Soil moisture-precipitation coupling over Central Europe: Relative impact of surface heterogeneity on deep convection

Florian Baur

München 2019

Soil moisture-precipitation coupling over Central Europe: Relative impact of surface heterogeneity on deep convection

Florian Baur

Dissertation
an der Fakulät für Physik
der Ludwig–Maximilians–Universität
München

vorgelegt von
Florian Baur
aus Bad Aibling

München, 18. Juni 2019

Erstgutachter: Prof. Dr. George C. Craig
Zweitgutachter: Prof. Dr. Bernhard Mayer
Tag der mündlichen Prüfung: 25. Juli 2019

Zusammenfassung

Die Vorhersage von Ort und Intensität potenziell verheerender, konvektiver Wetterereignisse ist eine der größten Herausforderungen der numerischen Wettervorhersage. Moderne Ensemble-Vorhersagesysteme auf konvektiver Skala berücksichtigen zwar unterschiedliche Unsicherheitsquellen, haben jedoch häufig Probleme, die Vorhersageunsicherheit einzuschätzen. Die Störung relevanter, aber unterrepräsentierter Prozesse kann die Darstellung der Vorhersageunsicherheit verbessern. Die Untersuchung der Wichtigkeit verschiedener Prozesse zur Vorhersage von Konvektion steht jedoch noch am Anfang. Zum Beispiel ist das Vorzeichen der Bodenfeuchte-Niederschlags-Kopplung und deren Skalenabhängigkeit immer noch umstritten.

Der erste Teil dieser Arbeit untersucht den kollektiven Einfluss der Bodenfeuchtebiase, sowie deren Heterogenität auf verschiedene Längenskalen, auf die Vorhersage konvektiver Niederschläge in realen Wetterszenarien über Mitteleuropa. Mittels des Consortium for Small-scale MOdeling (COSMO)-Modells mit einer Gitterweite von 2.8 km wurde eine Reihe von Experimenten für mehrere Sommertage durchgeführt, welche sich in ihren synoptischen Bedingungen unterscheiden. Verschiedene Längenskalen der Heterogenität zwischen 30 und 110 km werden durch Schachbrettmuster eingeführt und mit einem Bias von ±25 % überlagert. Die Experimente zeigen insbesondere bei schwachem synoptischem Antrieb eine nichtlineare, aber positive Korrelation zwischen einem großräumigen Bodenfeuchtebias und dem gebietsgemittelten Niederschlag. Im Gegensatz dazu wird eine negative, lokale Bodenfeuchte-Niederschlags-Kopplung mit erhöhtem Niederschlag über den trockenen Feldern des Schachbrettes gefunden. Diese räumliche Kopplung ist auf eine Wechselwirkung zwischen thermisch induzierten Zirkulationen und dem Hintergrundwind zurückzuführen, die eine persistente Aufwindregion an der Abwindflanke trockener Felder verursacht. Diese Zellen mit intensivierter Zirkulation dominieren bei Schachbrettgrößen von 40 bis 80 km, was zu einer bevorzugten Initiierung von Konvektion und zu einer geringeren Variabilität zwischen den Fallstudien führt. Die räumliche Verknüpfung der Konvektionsauslösung bei anderen Längenskalen oder synoptischen Bedingungen ist jedoch schwächer.

Im zweiten Teil werden die Auswirkungen von drei spezifischen Unsicherheitsquellen betrachtet, indem der relative Einfluss von Störungen der Bodenfeuchte, der Grenzschicht - und der Konzentration von Kondensationskeimen auf die Vorhersage von konvektivem Niederschlag und dessen Variabilität untersucht wird. Dazu werden für zehn aufeinanderfolgende Tage mit unterschiedlichen synoptischen Bedingungen, welche aus einer Unwetterperiode im Sommer 2016 über Mitteleuropa stammen, mehrere COSMO Experimente durchgeführt. Während die Menge des akkumulierten Niederschlags für alle Störparameter nahezu unverändert bleibt, weist die räumliche Variabilität und akkumulierte Ensemblevariabilität des Niederschlags deutliche Unterschiede auf. Auch wenn alle gestörten Parameter-Ensembles ein nicht zu vernachlässigendes Maß an Variabilität erzeugen, gibt es zwei Merkmale, welche die Bodenfeuchtestörungen von den übrigen Parametern unterscheiden. Bodenfeuchteheterogenität führt zu einem Anstieg der Variabilität während der In-

itiierungsphase von Konvektion, was zu einer steileren Zunahme der normalisierten Niederschlagsausbreitung führt. Stochastische Grenzschichtstörungen und Störungen der Anzahl an Kondensationskeimen wirken sich jedoch ab Modellinitiierung auf die räumliche Niederschlagsvariabilität aus. Darüber hinaus zeigt die Bodenfeuchteheterogenität die höchste Sensitivität gegenüber dem synoptischen Regime, wobei der stärkste Effekt bei schwachem Antrieb zu beobachten ist.

Die Ergebnisse dieser Arbeit legen daher nahe, dass systematische Bodenfeuchtigkeitsstörungen den Mangel an Variabilität in konvektivskaligen Ensemblevorhersagen mindern können.

Abstract

Forecasting the location and intensity of potentially devastating convective weather events is one of the major challenges of numerical weather prediction. Modern convective-scale ensemble prediction systems account for different sources of uncertainty but often have problems to adequately represent the forecast uncertainty. Perturbation of relevant but underrepresented processes can mitigate this underdispersion. However, research on the relative role of various convective-scale uncertainties is in its infancy. For example, opposing signs in soil moisture-precipitation coupling (SMP coupling) and its scale-dependence are still under debate.

The first part of this thesis examines the collective impact of soil moisture bias, as well as its heterogeneity on various length-scales on the forecast of convective precipitation in real-case scenarios over Central Europe. A series of experiments performed with the Consortium for Small-scale MOdeling (COSMO) model at 2.8 km grid spacing is conducted for several summer cases differing in their synoptic conditions. Various heterogeneity length-scales between 30 km and 110 km are introduced by chessboard patterns and superposed with a bias of $\pm 25\,\%$. The experiments reveal a nonlinear yet positive correlation between a large-scale soil moisture bias to the domain-averaged precipitation, especially during weak synoptic forcing. In contrast, a negative local SMP coupling with increased precipitation over the dry patches is found. This spatial coupling is traced back to an interaction between thermally induced circulations and the background wind, causing a persistent updraft region on the downwind flank of dry patches. These enhanced circulation cells are dominant for tile sizes of 40 km to 80 km, leading to preferential initiation of convection and result in a smaller day-to-day variability. The spatial locking of convection initiation is weaker at other heterogeneity scales or synoptic conditions.

The second part assesses the effect of three specific sources of uncertainty by examining the relative impact of soil moisture, stochastic Boundary-Layer (BL), and cloud condensation nuclei perturbations on the forecast of convective precipitation and its variability. Therefore, several COSMO experiments for ten consecutive days with different synoptic conditions chosen from a high impact weather period in summer 2016 over Central Europe are conducted. While the amount of daily accumulated precipitation remains almost unchanged for all perturbed-parameter ensembles, the spatial and ensemble variability of precipitation exhibits pronounced differences. While all perturbed-parameter ensembles generate a non-negligible amount of variability, there are two features discerning soil moisture perturbations from the remaining parameters. Soil moisture heterogeneity primarily introduces variability during convection initiation, causing a steeper increase in normalized rainfall spread before the onset of afternoon precipitation. Stochastic BL perturbations and perturbed aerosol concentrations, however, impact spatial precipitation variability from the model start onwards. Furthermore, soil moisture heterogeneity shows the strongest sensitivity to the synoptic regime with the largest impact during weak forcing.

The results of this thesis thus suggest that systematic initial soil moisture perturbations can potentially mitigate lack of spread in convective-scale ensembles.

Parts of this thesis are included in:

Baur, F., Keil, C., Craig, G.C.: Soil moisture–precipitation coupling over Central Europe: Interactions between surface anomalies at different scales and the dynamical implication. *Quarterly Journal of the Royal Meteorological Society*. 2018; 144 (717): 2863– 2875. doi:10.1002/qj.3415.

Keil, C., **Baur, F.**, Bachmann, K., Rasp, S., Schneider, L., Barthlott, C.: Relative contribution of soil moisture, boundary layer and microphysical perturbations on convective predictability in different weather regimes. *Quarterly Journal of the Royal Meteorological Society*. 2019; (accepted), doi:10.1002/qj.3607

> Contributions: Conduction of the ensembles with perturbed initial soil moisture, as well as the reference ensembles. Analysis of precipitation time series, normalized standard deviation and spatial variability (Fractions Skill Score) of the perturbed-parameter ensembles and the ensemble forecasts. Furthermore, there were several contributions to the text.

Arnault J., Rummler T., **Baur, F.**, Lerch S., Wagner S., Fersch B., Zhang Z., Kerandi N., Keil C., Kunstmann H.: Precipitation Sensitivity to the Uncertainty of Terrestrial Water Flow in WRF-Hydro: An Ensemble Analysis for Central Europe. 2018; *Journal of Hydrometeorology*, 19, 1007–1025, doi:10.1175/JHM-D-17-0042.1.

> Contributions: Advice on the application and description of the convective adjustment timescale.

Contents

1. Introduction

Deep moist convection is one of the most hazardous small-scale events globally causing the largest number of insured financial losses (Mills, 2005; Kunz et al., 2009). Local thunderstorms producing hail, strong gusts, and heavy precipitation do not only affect the location of occurrence but also threaten larger regions by flash floods in river catchment areas or by landslides. Those issues concern many socioeconomic sectors, such as tourism, finance, energy, or agriculture (Jahn, 2015). Accurate forecasts of such convective events can reduce socioeconomic losses since then individual measures could secure private properties, or civil protection could better prepare for potentially dangerous weather situations. According to Gunasekera (2010) or Frei (2010), the financial benefits exceed the investments in the weather services providing the forecasts. However, despite tremendous technical advances, improvements in the parameterization of physical processes, and reduction of grid spacing, quantitative forecasting of convective precipitation remains a major challenge for today's Numerical Weather Prediction (NWP) (Clark et al., 2016). This challenge has several reasons, as described in the following section.

1.1. The challenge of forecasting deep convection

Forecasts of the atmosphere face fundamental limits hampering predictability of the weather. Lorenz (1963, 1982) experienced the importance of initial conditions by rapidly growing small errors leading to fundamentally different realizations. This behavior is referred to as the nature of the chaotic atmosphere (Yoden, 2007) and implies that the predictability of numerical weather predictions is intrinsically limited. Lorenz (1982) describes this limit as an upper bound of predictability. This is a theoretical limit, coined intrinsic predictability, given a perfect model and infinitesimally small initial condition errors. In contrast to the intrinsic predictability, practical predictability describes the predictability based on the available prognostic system. In other words, it quantifies a particular forecasting system's ability to predict the weather and is affected by initial and boundary condition uncertainty, as well as uncertainties in the model physics. Initial condition uncertainty is a crucial limiting factor for the predictive skill for mid-latitude weather prediction. A recent study by Zhang et al. (2019) showed that a reduction of this uncertainty could gain one additional day of predictable forecast time. However, modern NWP systems are not only challenged by initial conditions but also by physical and small-scale processes not adequately resolved. A prominent example of a poorly resolved process and a major contributor to the loss in predictability is moist convection (Hohenegger

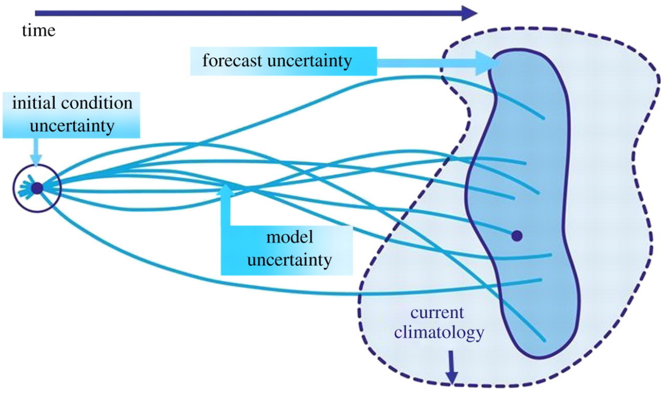

Figure 1.1.: Schematic showing the principle of an ensemble prediction accounting for different sources of uncertainty. Initial condition and model uncertainties (i.e. uncertainty in the representation of, for example, sub-grid processes in the model) are visualized. Those uncertainties cause a divergence of the individual realizations of the ensemble over time (blue lines). Aim of the ensemble forecast is to adequately represent the forecast uncertainty (blue area) lying within the range of climatologically possible states. This graphic is taken from Slingo and Palmer (2011).

and Schär, 2007). Small-scale disturbances introduced by misrepresentation of convection quickly grow in the presence of latent heat release and convective instability towards larger scales affecting synoptic-scale predictability (Selz and Craig, 2015). Ensemble Prediction Systems (EPSs) are a way to deal with the chaotic nature of the atmosphere in a statistical sense by predicting the forecast's probability rather than a single deterministic forecast. An ensemble comprises a set of different realizations deduced from slightly different initial conditions to sample the probability distribution of a particular weather situation (e.g., Slingo and Palmer, 2011). A schematic describing the basic principle is shown in Figure 1.1. As those uncertainties grow throughout time, an accurate representation of, for example, convection and related processes affect both the forecast skill of local and synoptic-scale weather.

As already mentioned, another issue for convective-scale NWP is the representation of convection. The representation of convection is, among others, continuously improved by parallel advances in computational resources and physical descriptions, enabling a regular reduction of model grid spacing (Clark et al., 2016). Until the early years of the 21st Century, models used for forecasting local weather were restricted to a horizontal grid spacing in the order of 10 km to 20 km. Deutscher Wetterdienst (DWD), for example, made the step from a Consortium for Small-scale MOdeling (COSMO) model with a grid spacing of 7 km and parametrized convection (i.e. COSMO-EU) towards a convection-permitting model with 2.8 km (i.e. COSMO-DE) in 2007. However, convection remains despite all the improvements very challenging to forecast as intensity, location, and timing depend on highly nonlinear and local processes (Barthlott et al., 2011b). Even though modern weather models operate with a grid spacing of a few km, which permits the explicit representation of convection, the small-scale processes of moist convection, such as single convective updrafts or initiation processes, are poorly captured. To adequately resolve those mechanisms, the grid spacing should be an order of magnitude smaller (i.e. $\mathcal{O}(100\,\mathrm{m})$; Bryan et al. (2003); Craig and Dörnbrack (2008)) than the grid spacing of approximately 2.8 km operationally used in the local area model at DWD. Small-scale Boundary-Layer (BL) processes, such as convergence lines, differential or elevated heating, or land-surface–atmosphere interactions, are hardly resolved by this model resolution. Thus, despite the convection-permitting model resolution, critical processes potentially triggering convection remain unresolved, which leads to a lack of predictive skill at small scales (Clark et al., 2016).

The lack of forecasting skill should be represented in the ensemble's confidence. This means that, assuming a reliable representation of the sources of uncertainty, the variability within the ensemble (for example measured as spread) should correlate with the mean error of the forecast. Hence, the spread of an ensemble is supposed to provide information on the forecast's uncertainty. Modern EPSs, however, often face the problem of underdispersion. The spread of an underdispersive ensemble is too small, and the model is too confident about the forecast. Introducing a better representation of the uncertainty of individual processes by particular perturbations can improve the variability within the model to better account for the actual uncertainty. State-of-the-art convection-permitting EPSs are, for example, often underdispersive for near-surface variables (Berner et al., 2015; Hally et al., 2014). This is in line with Klasa et al. (2018) recently diagnosing an underdispersion of afternoon precipitation examining three different convective events over Switzerland. Concerning forecasts of convective precipitation, studies from Romine et al. (2014) or Dey et al. (2016) support this overconfidence of convective-permitting EPSs.

Modern EPSs attempt to generate reliable dispersion of the forecast by accounting for the three general sources of uncertainty, namely, initial and boundary condition uncertainties, as well as uncertainties in the model physics. This is why the next two paragraphs describe different influences of the three sources of uncertainty on the ensemble forecast. Representation of the uncertainty related to unresolved small-scale processes by initial condition perturbations is a crucial issue for operational weather forecasting. Many convective-scale EPSs account for initial condition uncertainty (see also Fig. 1.1) by downscaling of coarser-resolution large-scale driving models. The convective-scale EPS of the DWD (COSMO-DE-EPS, operational from 2012 till 2017), for example, obtained its initial conditions from different global NWP systems (Kühnlein et al., 2014; Theis et al., 2015). Coarse-resolution, global driving models, however, hardly capture convective-scale uncertainties (Raynaud and Bouttier, 2016). Despite the positive impact of those downscaled initial condition perturbations on precipitation forecasts shown in several studies (e.g., Hohenegger et al., 2008; Peralta et al., 2012), they require about 9–12 h to grow downscale and produce small-scale variability (Raynaud and Bouttier, 2016). Since this spin-up time is often too long for operational convection forecasts, convective-scale initial condition perturbations are necessary. In 2017, COSMO-DE-EPS was replaced by a more sophisticated system obtaining its initial conditions by ensemble data assimilation. The ensemble Kalman filter generates an ensemble of initial states by estimating error statistics and is able to introduce small-scale variability (Evensen, 1994; Schraff et al., 2016). Note that the procedure of ensemble data assimilation is beyond the scope of this thesis. Even though data assimilation is already operationally used by some weather services (i.a. at DWD), the procedure remains, according to Raynaud and Bouttier (2016), computationally very expensive for the use on convective scales. Another way to represent small-scale initial uncertainty is to directly introduce perturbations on the forecasting model's grid (Johnson and Wang, 2016). Raynaud and Bouttier (2016), for example, suggest random perturbations drawn from an unbiased normal distribution as an affordable alternative to computationally expensive data assimilation systems. In their study, both techniques provided comparably skillful predictions of precipitation or 2 m temperature. This is supported by Vié et al. (2011) reporting about the beneficial impact of convective-scale initial condition perturbations on the precipitation forecast.

Besides the impact of initial conditions, small-scale uncertainty can also arise from an insufficient representation of lateral boundary conditions or model physics. By investigating several experiments using convective-scale ensembles with a forecast horizon of 12 h, Zhang (2019) found a different behavior of initial condition uncertainty compared to the other two primary sources of uncertainty. While exclusively perturbing model physics or lateral boundary conditions results in perturbation growth for all variables, initial condition perturbations mainly altered precipitation and showed less influence on the remaining variables. Moreover, a combination of only model physics and lateral boundary condition uncertainty may act on all spatial scales but still fails to represent the forecast uncertainty adequately. Therefore, they recommend applying a combination of all three sources of uncertainty in ensemble systems. This is important as the relative impact of initial and lateral boundary condition perturbation depends on the spatial scale of the forcing, or, in other words, on the synoptic regime (Stensrud et al., 2000; Vié et al., 2011; Kühnlein et al., 2014). For weather conditions dominated by synoptic-scale processes, lateral boundary conditions quickly control the forecast. In contrast, initial conditions uncertainties are dominant in the absence of synoptic forcing when the initiation of convection crucially depends on small-scale processes. However, the influence of lateral boundary conditions gradually increases and is dominant after approximately 12 h lead time (Vié et al., 2011).

The previous two paragraphs described the different influence of the three sources of uncertainty affect the precipitation forecast on different temporal and spatial scales. Since this thesis focuses on locally triggered convective precipitation on daily timescales, we will only consider initial condition and model uncertainty, as lateral boundary conditions are not likely to significantly affect locally triggered convection.

A way to mitigate the underdispersion is to specifically perturb relevant processes that are insufficiently represented in the model. Those processes can act as potential sources of predictability for convection as they extend the range of skillful forecasts. Examples for those processes are synoptic-scale triggers of convection, such as large-scale lifting (Bauer et al., 2015; Yano et al., 2018), or the ability of orography to initiate convection by flow distortion, forced lifting, or elevated heating (i.a. Kirshbaum et al., 2018; Bachmann et al., 2019). This paragraph lists three insufficiently represented processes that can be used to mitigate underdispersion of convective-scale ensembles. The first two processes introduce variability in the near-surface atmosphere. Since many convective-scale phenomena are forced from the lower boundary condition, surface and soil properties represent an important uncertainty source that has been mostly overlooked by the weather forecasting community (Santanello et al., 2019). While soil moisture and lateral terrestrial water flow are often considered as an uncertainty source as they are poorly represented in operational weather models (e.g., Hauck et al., 2011; Arnault et al., 2018), they have the potential to influence the precipitation forecast. First, soil moisture anomalies stemming from seasonal variability or evoking from preceding precipitation anomalies can fundamentally impact convection on a daily timescale. The soil moisture-precipitation coupling (SMP coupling), however, is highly variable due to the complexity of processes and the non-linearity of coupling mechanisms and is still under debate (Seneviratne et al., 2010). Furthermore, since processes acting on the soil moisture itself are usually slow, and anomalies remain persistent over long periods, Guo et al. (2012) found that good representation of soil moisture in spring can significantly improve the predictability of summer precipitation forecasts over Northern America. Second, there is increasing evidence in literature that the underdispersion of convective precipitation in convective-scale weather models may also be mitigated by stochastic perturbation schemes (e.g., Buizza et al., 1999; Bouttier et al., 2012; Rasp et al., 2018). A stochastic BL perturbation scheme introduces small-scale variability in the BL and, by doing that, increases the variability in convection initiation. A third alternative is the perturbation of the concentration of cloud condensation nuclei (CCN) in the atmosphere (e.g., Hally et al., 2014; Grant and van den Heever, 2014). This introduces variability in the formation of clouds and precipitation. To our knowledge, neither stochastic BL perturbation nor microphysics perturbations are currently used for operational ensemble forecasting.

This introductory section presented challenges of operationally forecasting convective precipitation. It furthermore showed three specific sources of uncertainty acting on different stages of convection that can be used to alleviate the underdisperion ensembles. The following Section 1.2 describes the basic concept of convection initiation. Moreover, general concepts of soil-atmosphere interaction, stochastic BL perturbations, and microphysical uncertainties implemented by CCN perturbations are presented. Since this thesis mainly focuses on the SMP coupling, further details about the influence of soil moisture on moist convection are provided in the literature overview in Section 1.3.

1.2. Basic theory

The previous section described some challenges of convective-scale weather forecasting and stated the importance of interactions between soil moisture and precipitation. Important physical processes underlying the challenging forecast of convection are presented in the following subsection by providing an overview of the parcel concept of convection initiation. Afterwards, three specific sources of uncertainty influencing convection triggering and formation of precipitation, as well as their interconnections and their potential usage for ensemble perturbation, are presented. Thus, we describe principles of soil-atmosphere interaction, the influence of stochastic perturbations, and the influence of CCN on cloud formation.

Concept of convection initiation

The basic concept of convection initiation provides important insight into the physical reasoning behind the challenge of forecasting locally triggered deep convection. The thermodynamic sounding shown in Figure 1.2 summarizes the parcel concept of convection initiation in an unstable environment. It shows the pathway of an air parcel that experiences a mechanism inducing forced lifting. As indicated by the black line, a rising air parcel cools dry adiabatically until it reaches saturation at the lifting condensation level (LCL). Thus, a further ascent happens moist adiabatically. This means that latent heat release due to condensation of water vapor reduces the vertical temperature gradient. The energy consumed to reach the level of free convection (LFC) is equal to the area between the environmental temperature (red curve) and the parcel ascent (black line) defining the convective inhibition energy (CIN) (blue area). Above the LFC, the air parcel is warmer than its surrounding, can rise freely until the level of neutral buoyancy (LNB) and convective

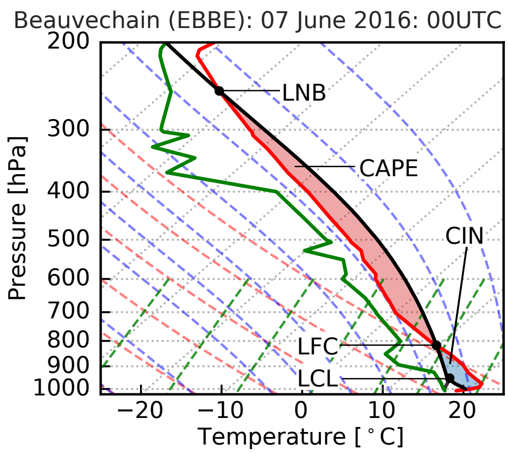

Figure 1.2.: Example of a thermodynamic skew-T, log-p diagram. The lines are the logarithmically scaled pressure (horizontal, dotted), the isotherms (dotted lines tilted towards the upper right), the dry adiabats (dashed, red), the moist adiabat (dashed, blue) and the saturation mixing ratio (green dashed). The diagram shows the environmental air temperature (red) and dew point temperature (green). Additionally, the lifting condensation level (LCL), level of free convection (LFC) and level of neutral buoyancy (LNB) are indicated. The shaded areas between the environmental temperature and a theoretical ascent of an air parcel starting from the surface (black, solid) indicate the convective available potential energy ($CAPE$) (red area) and convective inhibition energy (CIN) (blue area). The plot was produced using a code provided in May et al. (2008).

available potential energy ($CAPE$) (red area) is released. Hence, the crucial step deciding about the release of $CAPE$ and the initiation of deep moist convection is the mechanism necessary to overcome CIN.

It is often an interplay of processes lowering the CIN and mechanisms causing a forced lifting of near-surface air. On large scales, modifications of the mid-tropospheric lapse rate associated with, for instance, synoptic lifting, differential heating, upper-level divergence or low-level moistening may decrease CIN and favor convection initiation (Kottmeier et al., 2008; Markowski and Richardson, 2010). Mechanical lifting by mountain slopes or differential heating in complex terrain inducing slope wind circulations and confluence over mountain ridges represent the importance of orographic effects on convection initiation (Kirshbaum et al., 2018). Local discontinuities in the BL represent another prominent ingredient for convection triggering (Weckwerth and Parsons, 2006; Markowski and Richardson, 2010). Heterogeneities in surface heat fluxes, convergence lines, or the interaction of outflow boundaries and gust fronts emerging from the downdraft of mature convective systems can initiate such air mass boundaries. Hence, triggering processes are, apart from the synoptically controlled mechanisms, local processes closely linked to surface and BL conditions. Those small-scale processes constitute a challenge for state-of-the-art NWP in predicting convective storms. Improving the understanding and representation of those processes is of major importance for the prediction of intensity and location of deep convection. Three specific sources of uncertainty for moist convection and potential perturbation approaches connected to them are briefly described in the following subsections.

Basic concepts of soil–atmosphere interactions

In order to understand processes driving SMP coupling mechanisms, it is crucial to describe some basic concepts relating the heat and water budgets at the earth's surface. The heat budget at the earth's surface is externally forced by the net radiative flux (i.e. radiative flux accounting for incoming and reflected shortwave, as well as incoming and outgoing longwave radiation) and is mainly partitioned into sensible (SH) and latent (LH) surface heat fluxes. LH is the portion of net radiative flux expended on evaporation (vaporization of water from non-biologic surfaces), transpiration (vaporization of water from biologic surfaces) or melting of ice. Thus, the partitioning of surface heat is dependent on the availability of moisture at the surface. Sensible heat flux, instead, heats the BL from below and mainly depends on both, the vertical gradient of temperature near the surface and the near-surface wind speed. Characteristics of the soil, such as vegetation, land-use, or soil moisture, are crucial factors defining the partitioning of surface heat fluxes (e.g., Wallace and Hobbs, 2006; Markowski and Richardson, 2010). The fact that evaporation is not only a substantial part in the surface heat budget but is also an important sink term in the surface water budget underlines the importance of soil moisture for the near-surface atmosphere resulting in an important coupling with precipitation (Seneviratne et al., 2010).

Since evapotranspiration physically couples soil moisture and atmosphere, it is an essential factor for the interaction between those entities. Evapotranspiration is especially crucial for synoptic situations when local mechanisms provide moisture supply instead of atmospheric advection. According to, for example, Budyko (1974), the evaporative fraction ($EF = \frac{LH}{SH+LH} = \frac{1}{1+\beta}$, Bowen ratio: $\beta = \frac{SH}{LH}$) can be used to divide evapotranspiration into a moisture and an energy limited regime. For a dry soil regime, evapotranspiration is increasing with increasing soil moisture. In contrast to that, evapotranspiration is not sensitive upon changes in soil moisture for generally wet soil conditions. For this energy-limited regime, evapotranspiration is less dependent on soil moisture but on the available energy. Since plants get water stressed for dry soil conditions, they close their stomata to reduce the water loss by transpiration. By contrast, this does not happen if the soil is wet and the stomatal aperture is maximal (Koster et al., 2009).

The linkage between evapotranspiration and subsequent precipitation is highly nonlinear since dynamical and microphysical effects are included. Both positive or negative impact on precipitation depending on the stratification within the BL and its dynamical modifications are possible (Seneviratne et al., 2010; Guillod et al., 2014). Precipitation is closely correlated to evapotranspiration on long temporal ranges, and large spatial scales (e.g., Seneviratne et al., 2010), but its small-scale influence on short-range forecasting of convective precipitation is still under debate. This complex behavior and its implications for convection initiation are elaborated in more detail during the literature overview provided in the following Section 1.3.

Initial condition perturbations of the soil moisture are increasingly considered as being potentially beneficial for ensemble forecasting systems (Gustafsson et al., 2018). In a pre-operational version of the AROME-EPS, the forecasting system operationally used at Météo-France, Bouttier et al. (2016) evaluated the influence of ten different initial surface and soil perturbations. They found that multiplicative initial perturbation of soil moisture turned out to be among the most beneficial factors improving 2m temperature and humidity. Furthermore, the pre-operational forecasting system run at DWD contains random perturbations of initial soil moisture with correlation length-scales of 10 km and 100 km. First investigations implied the improvement of near-surface prognostic variables due to those perturbations (Schraff et al., 2016). According to Yano et al. (2018) or Bauer et al. (2015), such coupling mechanisms like the SMP coupling, however, require further understanding of spatial scales assigned to them for a better representation of its uncertainty and thus increase the spread of the ensemble by physically meaningful processes.

Stochastic Boundary-Layer perturbations

Application of small-scale initial condition perturbations is not the only way to deal with the uncertainty proceeding from insufficiently resolved scales and processes. Stochastic perturbations can account for uncertainties emerging from imperfect model design or underrepresented processes (see also Fig. 1.1). Especially partly resolved processes, like convection, can benefit from those mode physics perturbations (Berner et al., 2017). In fact, they are valuable methods capable of reintroducing small-scale variability into convective-scale models (Kober and Craig, 2016). Various approaches are applied containing methods perturbing, for example, tuning parameters (Bright and Mullen, 2002) or input fields (Lin and Neelin, 2003). Another widely used method adds multiplicative noise with a specific temporal and spatial correlation to parameterized tendencies (Buizza et al., 1999; Leutbecher et al., 2017). Those stochastic perturbation approaches showed increased ensemble spread (Buizza et al., 1999) and improved skill (Lin and Neelin, 2003) but often lack in consideration of different contributions of physical processes depending on the synoptic situation (Kober and Craig, 2016) and might increase spread in regions with an initially good representation of uncertainty.

The physically-based stochastic Boundary-Layer perturbations (PSP) scheme defines the perturbation amplitude by obtaining subgrid-scale standard deviations of temperature, humidity, and vertical wind from the turbulence scheme (Kober and Craig, 2016). Perturbations amplified with this standard deviation are added to the resolved part of each variable. Those perturbations add variability to the BL that would, in reality, arise from interactions between the soil or surface with the atmosphere. Inhomogeneities in the BL cause additional turbulence or small-scale convergence zones that can trigger convection (Kober and Craig, 2016). This leads to variability in the location of convection initiation in the ensemble and, by doing that, increases ensemble spread (Rasp et al., 2018).

Microphysical uncertainties

Up to now, this introduction mainly dealt with macrophysical uncertainties affecting the initiation of deep moist convection. However, there are inherent uncertainties associated with microphysical processes affecting the aerosol-cloud-precipitation interactions. Aerosols consisting of a mixture of hydrophilic and soluble compounds are indispensable for the formation of cloud droplets and precipitation. In perfectly clean air, droplets could only grow by homogeneous nucleation of supersaturated water. When starting with a tiny embryo droplet, its strongly curved surface has a higher equilibrium vapor pressure as compared to a flat surface. In other words, this so-called Kelvin effect causes increased evaporation rate over small droplets. For this effect to grow cloud or rain droplets, it would require high supersaturation as the achievable droplet radius is too small. Aerosols support the growth process in two ways. On the one hand, hydrophilic aerosols increase the radius of droplets countering the Kelvin effect. Soluble aerosols, on the other hand, decrease the equilibrium vapor pressure reducing the required supersaturation. This is described by the "Raoult effect" (Wallace and Hobbs, 2006).

Uncertainty in the aerosol-cloud-precipitation interactions is not only caused by physical processes but also by heterogeneous spatial distribution and varying residence time and transport mechanisms depending on the region of atmosphere (e.g., Devara and Manoj, 2013). In general, it is thought that additional aerosols acting as CCN lead to more numerous, but smaller cloud droplets, which can impact the precipitation formation via the collision-coalescence process (e.g., Hoose et al., 2009). Tao et al. (2012), however, summarizes several observational studies stating both, enhancement and suppression of rain processes depending on the existence of an ice phase in the rain process and the concentration of CCN. Very clean air (i.e. low concentration of CCN) result in an enhancement of warm rain processes (i.e. absence of ice phase) whereas cold rain processes are suppressed. Interestingly, the opposite is true for high CCN concentrations. Furthermore, the mixed-phase region is deeper for the latter aerosol concentrations as compared for clean conditions. Seifert et al. (2012) show that in convection-permitting simulations for three summer seasons across Central Europe, the average effect of varying aerosol concentrations on precipitation is negligible due to buffering effects, although the cloud properties themselves (like, e.g., condensate amounts) are strongly influenced.

Perturbing the aerosol concentration influences cloud formation by altering the collision-coalescence process and reducing required supersaturation of the air. Moreover, it varies cloud-radiation and radiation-aerosol interactions thus indirectly feeding back to the radiation budget at the earth's surface (Seifert et al., 2012; Betts and Silva Dias, 2010; Fan et al., 2016).

The previous subsections described three specific sources of uncertainty in convection initiation and formation of precipitation but acting on different steps in the convection process. The three methods share processes physically linking them to each other as they all act on or are influenced by the earth's surface radiation budget. Heterogeneous perturbations in the initial soil moisture conditions introduce uncertainties at the surface affecting the growth and structure of the BL by radiative processes and thus is directly linked to convection initiation and precipitation. While soil moisture perturbations modify the BL via surface heat budget, physically-based stochastic Boundary-Layer perturbations (PSP) directly perturb the BL structure. Perturbing the aerosol concentration affects the earth's surface radiation budget thus indirectly feeding back to the BL (Seifert et al., 2012; Betts and Silva Dias, 2010; Fan et al., 2016). Since the main focus of this thesis, however, is on the interaction between soil moisture and convective precipitation, the following literature review presents further details about the SMP coupling.

1.3. The role of land surface processes in the initiation of convection

Land surface processes, such as the processes described in the previous section, play a crucial role in the initiation of deep convection and subsequent precipitation and are of major importance for weather and climate (e.g., Schär et al., 1999; Pielke, 2001). Spatial and temporal anomalies in surface characteristics, like surface roughness, orography, leaf area index, vegetation, or, particularly, soil moisture can result in anomalies in surface energy budget (e.g., Taylor et al., 2011) by determining the partitioning of the surface heat flux into latent and sensible heat. The partitioning of the surface heat flux strongly influences the diurnal evolution of the BL. The SMP coupling has been found to be relevant on many timescales and encompasses long-term memory effects caused by the seasonal storage of water affecting continental climate (e.g., Schär et al., 1999; Koster et al., 2004) as well as the daily timescale by triggering cumulus convection (e.g., Clark et al., 2004; Barthlott et al., 2011b). Likewise, SMP coupling covers spatial scales ranging from continental-scale down to the convective-scale. Presently, SMP coupling at convective-scales poses a major challenge in NWP concerning the initiation of deep convection and the subsequent formation of precipitation. In the present thesis, we focus on the SMP coupling at convective scales [$\mathcal{O}(10\ km)$] on daily timescales. The complexity related to the SMP coupling is discussed in the following literature review.

Observational evidence

The sign of SMP coupling and its scale-dependence have been controversial issues when examining soil-atmosphere interactions. Based on findings and methods developed in Taylor et al. (2012) concerning spatial soil moisture-precipitation coupling, Guillod et al. (2015) presented additional observational evidence on the coupling of soil moisture characteristics before afternoon precipitation. Using 10 years of global satellite observations at 0.25° spatial and 3-hourly temporal resolution, the interplay of spatial soil moisture heterogeneity and temporal soil moisture anomaly was examined. They found a positive SMP coupling (more precipitation over wetter soils) for temporal soil moisture anomalies (i.e. an anomaly compared to the mean seasonal cycle) and, in contrast, a negative SMP coupling for spatial anomalies. Thus, locally, heterogeneous soil conditions exhibit rainfall maxima over dry anomalies. This different influence of temporal and local soil moisture anomalies was recently proved by Welty and Zeng (2018) or Moon et al. (2019) using different regional and global observation data sets and global climate modeling. The role of spatial discontinuities in soil moisture was additionally emphasized by Taylor et al. (2018) as they observed the initiation of convective systems over dry regions near soil moisture gradients. However, those convective cells weakened as they were advected over adjacent wetlands in the sub-Saharan African region. However, Welty and Zeng (2018) hypothesized about an impact of the synoptic regime on the SMP coupling potentially inverting the coupling sign during strong synoptic forcing. Hsu et al. (2017) furthermore found a locally positive SMP coupling for locally dry anomalies embedded in very wet large-scale soil moisture conditions.

While numerous studies (e.g., Koster et al., 2004; Taylor et al., 2011) show that the SMP coupling is more pronounced in dry and semi-humid climates of the globe, Yang et al. (2016) found anomalous springtime soil moisture conditions influencing summer precipitation over Central European and Central Northern American regions. Besides this seasonal coupling, Taylor (2015) linked convection initiation to soil moisture based on satellite observations of cloud top and land surface temperature as well as soil moisture over Europe. According to them, convection initiation seems to be favored on the downstream side of dry surfaces, close to wetter areas.

Those observational studies report about two important features of soil moisture affecting precipitation in different ways. On the one hand, a seasonal anomaly is mostly positively coupled with precipitation while, on the other hand, convective precipitation is often linked to heterogeneity in soil moisture. Furthermore, those studies predominantly deal with large spatial and long temporal scales. The influence of soil moisture anomalies on convective precipitation on daily timescales, however, is hardly covered. Moreover, they give evidence for the different influence of large- and small-scale soil moisture anomalies but are not able to give information about dominant heterogeneity length-scales or mechanisms leading to the different coupling signs.

Numerical modeling studies in idealized settings

Although all the advances based on statistical evaluations of observations, those studies have difficulties in demonstrating causal relationships as mechanisms causing precipitation are often upstream of the location of precipitation (Ford et al., 2018). Much of the numerical modeling work on SMP coupling was based on the application of uniform soil moisture perturbations. A positive coupling between uniform soil moisture perturbations and subsequent precipitation was found in simulations with horizontally homogeneous atmospheric initial conditions using a convection-permitting model resolution (Schlemmer et al., 2012; Imamovic et al., 2017) and Large Eddy Simulations (Cioni and Hohenegger, 2017).

Other studies focus on the effect soil moisture heterogeneity on the SMP coupling and elucidate dominant processes starting from those spatial anomalies (e.g., Froidevaux et al., 2014; Lee et al., 2019). For the same surface heat flux, dry patches show lower latent heat fluxes in comparison with nearby moist patches. The resulting surplus in sensible surface heat flux leads to an increased buoyancy over dry patches resulting in a deeper BL and compensating thermally induced circulation between the differentially heated dry and moist land areas (Mahfouf et al., 1987). Those circulations alter the location and timing of convection especially under weak synoptic forcing conditions (e.g., Pielke, 2001; Birch et al., 2015) and occur at heterogeneity length-scales in the meso-β-scale ($20 - 200\,\mathrm{km}$) (Segal and Arritt, 1992).

The influence of gradients in soil moisture on the dynamics in the lower troposphere has almost exclusively been studied using model setups with horizontally homogeneous atmospheric initial conditions. Convection-permitting 2D simulations (Robinson et al., 2008) and highly idealized 3D simulations (Cronin et al., 2015; Lee et al., 2019) found a preferential initiation of moist convection over dry spatial anomalies having a scale of $\mathcal{O}(10\ km)$. Froidevaux et al. (2014) studies the interaction between local soil moisture anomalies and the background wind by running simulations with horizontally homogeneous atmospheric initial conditions on a convection-permitting resolution. Varying horizontal wind speed, it has been found that the background wind shifts the preferred region of convection triggering to the upstream side of areas with positive soil moisture anomaly. Moreover, Lee et al. (2019) find the ability of a strong background wind ($> 2\,\mathrm{ms}^{-1}$) to suppress thermal circulations and the impact of soil moisture heterogeneity on convection initiation based on highly idealized large-eddy simulations (LESs).

Those idealized studies emphasize the importance of soil moisture gradients for the dynamics of the lower troposphere, as well as interactions of thermally induced circulations with the background wind. However, those studies cannot answer whether those mechanisms still hold for operationally used models with a grid-spacing of a few km and realistic spatially variable surface or atmospheric conditions.

Regional numerical modeling studies in real-case scenarios

Similar to the above mentioned observational studies, regional studies under real-case scenarios mostly concentrate on semi-arid to semi-humid regions of the globe, which are considered to be preferentially affected by soil moisture-precipitation interactions. Regional modeling studies over the Great Plains (Northern America) support the importance of soil moisture heterogeneities interacting with deep convection. Sensitivity analysis simulating convection embedded in quasi-stationary fronts benefited from an accurate description of the initial soil moisture state (Chang and Wetzel, 1990). Spatial variations in soil moisture caused differential heating, which enhanced lifting near the gradient and improved the realistic representation of the convective events compared to observations. While soil moisture heterogeneity has an important impact on the initiation of convection, its effect is almost negligible concerning regional-scale average precipitation (Trier et al., 2008). Supporting above mentioned studies over Northern America, Adler et al. (2011) found the transition from shallow to deep convection predominantly occurring near the upwind part of circulation cells thermally induced by differential heating of the surface by exploiting convection-permitting COSMO simulations over Western Africa. In a different study by Cheng and Cotton (2004), the dependence on soil moisture accuracy, however, was minor, as large-scale synoptic forcing had a more pronounced influence. Nevertheless, they found that an accurate representation of soil moisture on a spatial scale of 40 km or finer improves the forecast of rainfall.

In general, the effect of soil moisture anomalies on convective precipitation in the European region in real-case scenarios using convection-permitting NWP models is rarely examined. Among the few studies that were published, Hohenegger et al. (2009) and Barthlott et al. (2011a) show a strong case-dependence of the SMP coupling in various mountainous regions in Central Europe. Likewise, Koukoula et al. (2019) could not find consistent feedback after performing several case studies over Southern France using 1 km model resolution initialized with different soil moisture conditions of varying accuracy. Nevertheless, they found a strong influence of initial soil moisture on intensity and location spatial distribution of deep convection. They concluded that an accurate representation of soil moisture leads to a better representation of local circulations driven by soil moisture. In contrast to that, Van Weverberg et al. (2010) reported only a vanishing beneficial impact of accurate soil moisture representation simulating two cases of convection driven by strong buoyancy, and strong wind shear over Belgium. Nevertheless, the majority of those real-case studies report about a beneficial impact of accurate representation of soil moisture on the forecast of precipitation.

Regional numerical modeling studies thus indicate that orographic and atmospheric complexity hampers the clarity of a potential SMP coupling in real-case scenarios. While most studies conclude that an accurate representation of soil moisture has a beneficial impact on the precipitation forecast, systematic studies focusing on the influence of the heterogeneity length-scale of soil moisture anomalies are missing. This, however, would provide valuable information about the potential impact of heterogeneous soil moisture perturbations in EPSs.

Soil moisture-precipitation coupling in the context of the synoptic regime and analyzed scale

Another underrepresented issue of the SMP coupling is the consideration of multiscale interactions as well as the synoptic regime of the weather situation. On the one hand, there are observationally based studies (e.g., Taylor and Ellis, 2006; Taylor et al., 2013) or studies based on idealized simulations (e.g., Froidevaux et al., 2014; Lee et al., 2019) focusing on spatial scales in the order of $\mathcal{O}(10\,\mathrm{km})$. Prominent processes are linked to thermally induced circulation cells near the surface, as well as low-level stratification and humidity (Findell and Eltahir, 2003a). On large scales, on the other hand, studies like Koster et al. (2004) or Schär et al. (1999) mostly report a positive coupling dominated by surface evaporation. A pioneering study by Guillod et al. (2015) unites those two scales in a global observational study reporting a positive SMP coupling for large scale soil moisture anomalies and, in contrast, a negative SMP coupling for spatial anomalies. Even though a subsequent study proved their concept using observations and coarse-resolution, global, climate modeling, evidence on a regional scale using convective-scale modeling on daily timescales under real-case scenarios is still missing.

The literature review showed evidence for the synoptic situation weakening the SMP coupling for single case studies over Europe (Van Weverberg et al., 2010) or America (Cheng and Cotton, 2004). According to a recent study evaluating more than 16000 convective events over the Great Plains by Ford et al. (2018), the interaction between soil moisture, atmosphere, and subsequent precipitation significantly weakens for increasing synoptic forcing. In fact, large-scale conditions can also change the sign and intensity of SMP coupling on a local scale (Ford et al., 2015). Therefore, it is important to consider the synoptic situation when investigating the SMP coupling.

1.4. Aims and outline of this thesis

The assessment of the scale-dependent, as well as the relative impact of heterogeneous soil moisture perturbations in convective-scale NWP is now possible due to important scientific advancements. Developments in convective-scale modeling and improvements of computational power enable us to transfer knowledge gained in highly idealized and observational studies to a state-of-the-art, operationally used convection-permitting numerical weather model and to real-case application.

The literature review presented in the previous sections revealed a lack of understanding of amplitude and sign of SMP coupling mechanisms considering different spatial scales and synoptic conditions. Furthermore, the scientific community realized the importance of surface-atmosphere coupling mechanisms and increasingly incorporates surface perturbations in modern EPSs to mitigate underdispersion of ensembles by perturbing those relevant, but poorly represented sources of uncertainty. This, however, still requires a more in-depth knowledge of coupling mechanisms and their representation in convection-permitting numerical weather models. Moreover, the multi-scale aspect of heterogeneous soil moisture initialization in the Central European region is barely addressed by current literature. Systematic studies focusing on the influence of the heterogeneity length-scale of soil moisture anomalies in real-case scenarios including the full complexity of the surface and atmosphere are missing. Understanding dominant coupling mechanisms, relevant spatial length-scales, and the relative impact of heterogeneous soil moisture compared to other perturbation approaches are of major importance regarding the design of future EPSs.

This dissertation focuses on assessing dynamical processes and the relative impact of heterogeneous soil moisture initial condition on convection initiation and subsequent precipitation in the Central European region. The representation of physical mechanisms in a modern, convective-permitting numerical weather model is of special interest. This thesis will aim at the identification of the scale-dependent impact of heterogeneous soil moisture perturbations on convection initiation and subsequent precipitation. Doing that, we will describe relevant processes in real-case scenarios, and assess the relative impact of soil moisture perturbations compared to stochastic Boundary-Layer perturbations and aerosol perturbations. The lack of research concerning the influence of the SMP coupling and its potential importance for uncertainty representation and mitigation of underdispersion in future EPSs motivates the following research questions addressed throughout this thesis:

- RQ-1 How does an initial soil moisture bias affect convective precipitation considering different synoptic regimes?
- RQ-2 What is the collective and regime dependent impact of soil moisture bias and heterogeneity on different spatial scales on the precipitation forecast?
- RQ-3 What is the relative impact of soil moisture, stochastic Boundary-Layer, and aerosol perturbations on convective precipitation considering different synoptic regimes?

The following Chapter 2 comprises the research strategy applied to answer the questions stated above. Furthermore, it describes the used weather model, the performed experiments, as well as measures to evaluate the experiments and characterize the synoptic conditions. Results aiming to answer the research questions are presented in Chapter 3 starting with uniform bias experiments and proceeding via the evaluation of heterogeneous soil moisture perturbations to the assessment of the relative impact of three specific, major sources of uncertainty in the convection initiation process. Chapter 4 discusses the results in light of a broader context and provides some future implications.

2. Methodology

The following section presents the research strategy utilized to answer the questions posed in the previous chapter before it describes the procedures and methods used in this thesis in more detail. It provides a description of the COSMO model and the designs of the three different sets of experiments before two benchmark simulations are described. Furthermore, the convective adjustment timescale used to characterize the case studies, as well as the case studies themselves, are presented. Further detail about the choice of case studies and the underlying convective adjustment timescale are presented. Finally, the reader finds information about metrics to describe spatial variability and the thermodynamic state of the lower troposphere.

2.1. Research strategy

The literature review provided in the previous chapter exposes a lack of understanding concerning the impact of heterogeneous soil moisture perturbations on deep convection considering different synoptic situations. This lack is especially evident, considering real-case scenarios in a convection-permitting model environment. Furthermore, it is essential to assess the relevance of the SMP coupling by comparing the influence of soil moisture perturbations to other perturbation methods, such as stochastic BL perturbations or perturbations of the CCN concentration. This comparison is important concerning potential applications in future EPSs.

Assessing the impact of different perturbation approaches on convective precipitation in real-case scenarios requires a convection-permitting NWP model. We chose the Consortium for Small-scale MOdeling (COSMO) model, which is operationally used at DWD in a convection-permitting configuration for daily forecasts over the Central European region. It is furthermore applied in numerous highly idealized (e.g., Bachmann et al., 2019), and real-case (e.g., Barthlott and Kalthoff, 2011) studies with great success in accurately reproducing the atmospheric state and physical processes. By choosing this model, we can build on studies dealing with the coupling between surface processes and precipitation in highly idealized setting (e.g., Imamovic et al., 2017), and on studies applying uniform initial soil moisture perturbations (e.g., Barthlott and Kalthoff, 2011). We intentionally run the model in its operational configuration to remain as close as possible to problems in everyday weather forecasting and to identify dominant, resolved processes being relevant for the operational service.

A difference to the operational model configuration is the application of the double-moment microphysics scheme (Seifert and Beheng, 2006). This scheme enables a more accurate description of cloud properties and will potentially be incorporated in future operational modeling systems at DWD. More importantly, it exclusively enables us to vary the concentration of cloud condensation nuclei (CCN) in the model. This is important in the context of research question RQ-3 and allows to compare perturbations of the impacts of the initial soil moisture, stochastic BL perturbations and microphysical perturbations affecting autoconversion processes and the activation of cloud droplets (i.e. CCN).

Along with the quasi-operational setting of COSMO, we adopt the model domain centered over Germany and containing parts of its neighboring countries. This region provides the opportunity to study the sensitivity of the results to orography as the domain contains a relatively flat northern and an orographically structured southern part. Since we are assuming similar synoptic conditions across the entire domain, differences in the impact of perturbations can be attributed to the terrain's complexity as orography can strongly influence the location of convection triggering.

We carefully selected case studies in order to identify the sensitivity of the results to the synoptic regime. The focus lies on locally triggered deep moist convection, which is challenging to predict for modern NWP. Thus, case studies must exhibit a pronounced daily cycle of convective precipitation spread over the entire model domain. Even though omitting situations directly affected by frontal activity, we collected case studies revealing local heavy precipitation under different synoptic conditions. An objective classification of the synoptic regime is performed by applying the convective adjustment timescale (Done et al., 2006; Keil et al., 2014, see Section 2.5). A framework introduced by Findell and Eltahir (2003a) provides information about the thermodynamic preconditioning according to which initiation of convection is favored over dry or wet soils (see Section 2.8). Among others, we chose a ten-day period of high impact weather comprising daily heavy precipitation under varying large-scale conditions. This period is of high interest as it caused high financial losses by local convective precipitation events (Piper et al., 2016), and it is the basis for comparisons in research question RQ-3.

We apply three sets of experiments specifically tailored to the three research questions posed in Section 1.4. The first set, relating to RQ-1, comprises uniform bias perturbations providing valuable information about the impact of soil moisture perturbations on convective precipitation and its spatial variability considering different synoptic conditions.

The second set of experiments is designed to introduce soil moisture heterogeneity at well-defined length-scales systematically. Chessboard patterns with different tile sizes are linked to the previous experiments by superposing heterogeneous initial soil moisture conditions with a uniform offset. Those experiments are suited to provide insight into the collective impact of soil moisture bias and heterogeneity on convective precipitation, considering the prevailing synoptic conditions (RQ-2). The introduced soil moisture pattern enables us to investigate the dynamical response of the lower troposphere to sharp soil moisture gradients. This setting is, to our knowledge, the first transferring findings from highly idealized studies into a real-case application and enables us to identify dominant length scales of soil moisture perturbations in an operationally used convection-permitting weather model. Since our focus is on the influence of heterogeneous initial soil moisture on convective precipitation, we chose to have a short spin-up time for the simulations as gradients and heterogeneity length-scale might lose sharpness after longer forecasting time.

The third set of experiments realizes more realistic initial condition perturbations. High-, Low-, and Band-pass filtered soil moisture conditions unify dominant length-scales found in the previous chessboard experiments with perturbation length-scales used in the Kilometre-Scale Ensemble Data Assimilation (KENDA) scheme. KENDA provides initial conditions for the new EPS used operationally at DWD since March 2017 (Schraff et al., 2016; Theis et al., 2017). We compare the influence of this perturbed-parameter ensemble featuring spatial inaccuracy in initial soil moisture with two other major sources of uncertainty in convection initiation and formation of precipitation. While soil moisture perturbations affect the triggering of deep convection via differential surface heating, stochastic BL perturbations introduce small-scale variability directly affecting the BL structure. Perturbing the aerosol concentration influences, on the one hand, the cloud formation by perturbing the autoconversion process via different concentrations of cloud condensation nuclei (CCN). Since cloud formation is influenced, cloud-radiation interactions, on the the other hand, affect the earth's surface radiation budget and thus indirectly feeds back to the BL (e.g., Seifert et al., 2012; Fan et al., 2016). This choice of perturbation parameters features important specific sources of uncertainty related to the initiation and formation of deep moist convection. The relevance of the comparison of those specific uncertainty sources is given by important physical processes linking them with each other but affect convection at different stages. Performing separate COSMO experiments with a single type of perturbation allows for the accountability of differences between the ensembles to the respective perturbation. To assess the relevance of the variability caused by the perturbations, we introduce a lower and upper benchmark for spatial and ensemble variability by a white noise ensemble (WNoise) and the operational COSMO-DE-EPS. Assessing the relative impact of different perturbation methods is of high importance as future NWP systems might increasingly incorporate multi-parameter perturbations to mitigate underdispersion of ensembles. By using those perturbed-parameter ensembles, we are eventually able to assess the relative impact of soil moisture, stochastic BL, and CCN perturbations on convective precipitation (RQ-3).

To assess the ensemble and spatial variability of the precipitation forecasts, we apply two different measures. The normalized ensemble spread is a widely used measure to quantify the ensemble variability, and itself is insensitive of the ensemble size as it is divided by $N - 1$. Spatial variability is measured by means of the Fractions Skill Score (FSS). The FSS is commonly used as a measure of predictive skill. We, however, interpret the FSS as a measure of spatial variability within a perturbed-parameter ensemble.

Note that we do not attempt to represent realistic soil moisture error distributions. These are likely to have complex structures projecting on many length-scales, leading to changes in the atmospheric flow that are difficult to interpret. Instead, by understanding how the atmospheric response varies with the analyzed spatial scale and the weather regime, we aim to enable future research to focus on the soil moisture uncertainties that are most relevant to precipitation forecasts. Another limitation of this study is the ensemble size, which had to be limited due to computational constraints. However, Clark et al. (2011) diagnosed statistically indistinguishable results for small ensemble sizes (3-9 members) compared to their full 17-member ensemble investigating precipitation forecast skill in convection-permitting ensembles. Thus, despite limited and variable ensemble sizes, we are convinced that sensitivities of precipitation forecasts are attributable to the different perturbation approaches. The selection of parameters chosen for perturbations does not imply other parameters' unimportance. We intend to feature different sources of uncertainty linked to deep moist convection and leave the exploration of other parameters, as well as synergistic effects of different parameters to future research.

2.2. Model setup

The numerical experiments are conducted using the operational COSMO-DE forecast model (Version 5.3) (Baldauf et al., 2011). The fully compressible equations of motion are solved on an Arakawa-C grid with a horizontal resolution of 0.025° and a model time step of 25 s. The domain covers the area shown in Figure 2.1 and is discretized in 461 by 421 horizontal grid cells and 50 vertical levels. This results in an approximate grid-spacing of 2.8 km or a domain size of roughly 1300 km × 1200 km. The COSMO-DE experiments are started daily at 00 UTC with 24 h forecast lead time and driven by hourly COSMO-EU analysis data available on a 7 km grid and interpolated on our grid using the preprocessor INT2LM (Version 2.03) (Schättler and Blahak, 2017). The horizontal grid spacing of approximately 2.8 km allows for the explicit representation of deep convection, whereas shallow convection is parameterized using a mass flux scheme (Tiedtke, 1989). 1-D turbulence is parameterized based on a prognostic equation of Turbulent Kinetic Energy (TKE) using a level 2.5 closure scheme. The two-moment microphysics scheme (Seifert and Beheng, 2006) is applied to benefit from the more accurate representation of cloud properties (see, e.g., Igel et al., 2014), the availability of additional cloud quantities and the possibility to perturb the concentration of CCN. Unless otherwise noted, a typical CCN amount for continental conditions over Central Europe of 1700 cm^{-3} is used. The Harmonized World Soil Database provides external parameters for soil characteristics (HWSD), for topographical information by the 30 arcsec gridded, quality-controlled Global One-km Base Elevation Project (GLOBE) and land use by the GLOBECOVER Database.

Figure 2.1a shows the topographic situation with the gray shading. We divide the domain into a fairly flat northern and an orographically structured southern part. Throughout the thesis, the *German subdomain* is divided into a plain northern part

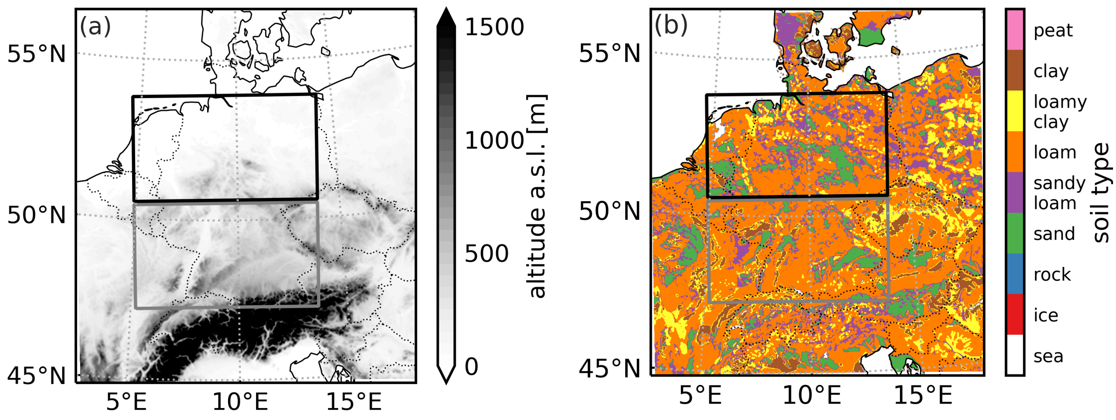

Figure 2.1.: Topographical map (a) and distribution of soil types (b) of the entire COSMO-DE domain, as well as the German subdomain consisting of a Northern German (black box) and Southern German subdomain (gray box). Political boundaries are shown in dotted and coastlines in black solid lines.

(i.e. *Northern German subdomain*), and a southern part showing complex terrain (i.e. *Southern German subdomain*). Mountain ranges, such as the Alps, Vosges, and the Central German Uplands characterize the topographic structure of the southern part. The latter low mountain range marks the division to the comparatively flat northern subdomain.

Soil processes are simulated using the multi-layer soil model (TERRA-ML) with seven soil layers as described in Doms et al. (2011). The soil model considers precipitation and the formation of rime and dew as sources while runoff, evaporation, and transpiration represent sink terms of water in the soil. For thermal interaction between soil and atmosphere, COSMO considers the radiation budget at the surface, as well as sensible and latent heat fluxes. Surface heat fluxes are computed using a bulk transfer coefficient based on similarity theory and dependent on the stability of the atmospheric surface layer. The latent heat flux is determined by the evaporation that depends, among others, on the degree of saturation of the soil, which is mostly defined by the local soil type. Dominant soil types are loam and sand in the German domain (see Fig. 2.1b). Sensible heat fluxes are determined by surface temperatures in TERRA-ML. Thus, surface heat fluxes are largely dependent on local soil conditions.

2.3. Experimental Design

This section provides a detailed description of the performed sets of initial soil moisture perturbations used to identify dominant mechanisms in SMP coupling and relevant heterogeneity length scales. Furthermore, three perturbed-parameter ensembles are presented consisting of soil moisture perturbations (Soil), stochastic

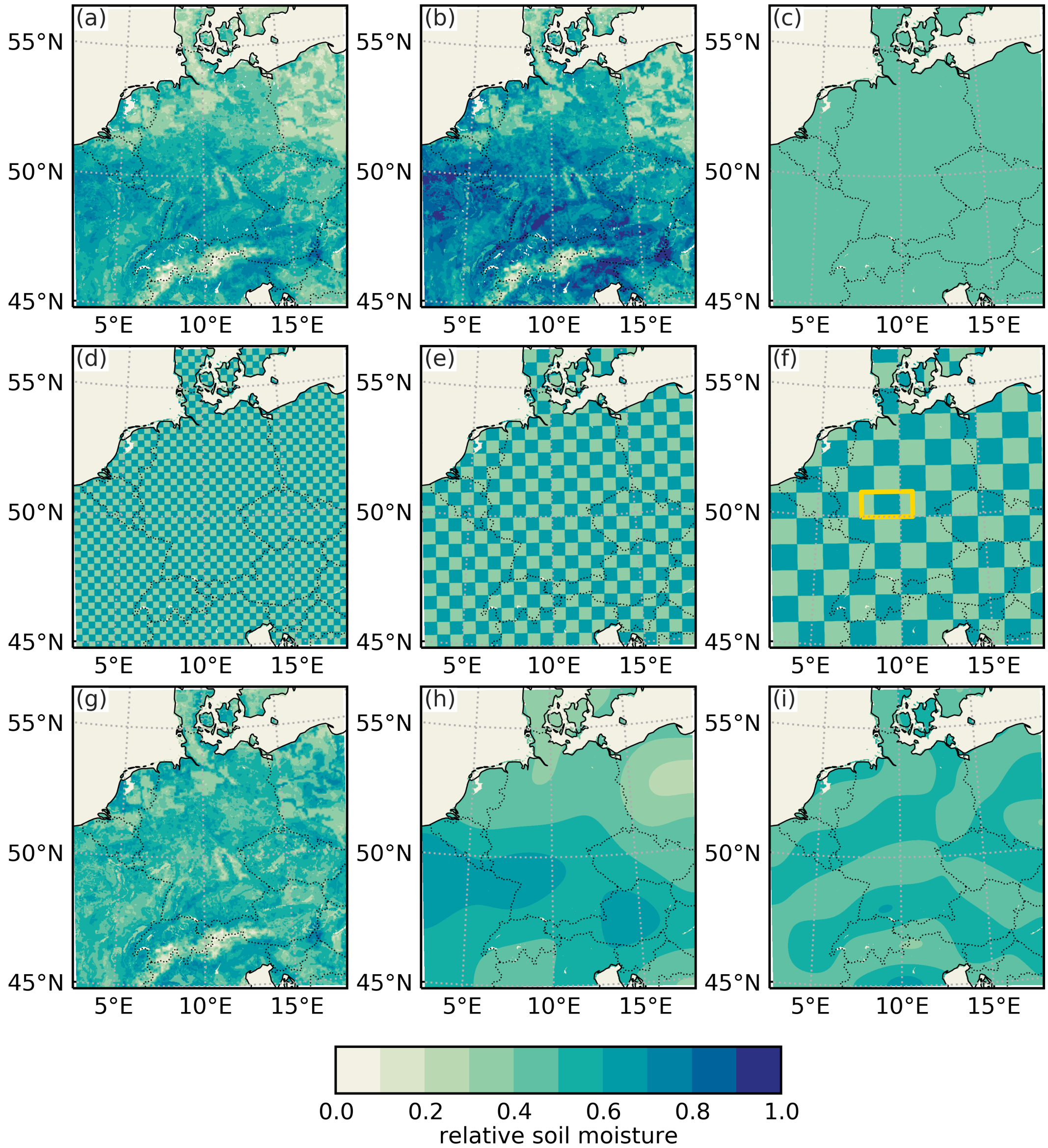

Figure 2.2.: COSMO-DE domain covering Central Europe juxtaposed with political boundaries shown in dotted and coastlines in black solid lines. Different of initial soil moisture conditions including the unperturbed reference (REF, a), positive bias (B125, b), uniform soil moisture (UNI, c), chessboard patches with 10 (C100_28k, d), 20 (C100_56k, e) and 40 (C100_112k, f) grid cells patch sizes, as well as filtered initial conditions showing high-pass (LP56k, g), low-pass (HP56k, h) and band-pass (HP50k, i) filtered initial conditions are shown in shadings. The yellow box in (f) exemplarily shows the sliding window to compute mean vertical cross-sections depicted in Figures 3.12, 3.14 and 3.15.

Boundary-Layer perturbations (PSP), and different realizations of cloud condensation nuclei (CCN). Note that, especially during the evaluation of the high impact weather (HIW) period in Section 3.3, the perturbed-parameter ensembles are for simplification often referred to as "ensembles".

2.3.1. Soil moisture perturbations

To study the role of soil moisture bias and heterogeneity, we modulate the soil moisture at the initial time by choosing pragmatic perturbations. For the construction of soil moisture fields, we define a relative soil moisture (w_{so})

$$w_{so_{i,j}} = \frac{w_{l_{i,j}}}{V_{p_{i,j}}\ \Delta z} \tag{2.1}$$

calculated based on the pore volume (V_p) specified for the soil type present at an individual grid cell i, j. The liquid water content of the soil layer in a grid cell is denoted $w_{l_{i,j}}$ with Δz being the thickness of the soil layer. This definition is similar to the degree of saturation for a specific soil type as described in Hillel (1998).

Next to an unperturbed reference simulation (REF) (Fig. 2.2a), we conducted three different sets of experiments each contributing to one of the research questions. The first set with constantly reduced / increased soil moisture allows to inspect the influence of bias in initial soil moisture state on the forecast of deep convection (see RQ-1). Each grid cell's soil moisture is multiplied by a factor of 0.75 (1.25) to simulate a soil moisture bias of $\pm 25\,\%$ (as in Barthlott et al., 2011a). Those experiments are named B075 and B125. Mean deviations between observations and the COSMO model amounting to 20-30 % in the area of interest (Hauck et al., 2011) additionally motivate this value. An example of a B125 initial soil moisture distribution is shown in Figure 2.2b. Note that the word "bias" relates to a bias relative to the reference state as a comparison to observations is beyond the scope of this study.

The second set of experiments focuses on the collective impact of initial soil moisture bias and heterogeneity on convective initiation and precipitation (see RQ-2). Chessboard patterns in initial relative soil moisture are introduced to imprint spatial variability at well-defined spatial scales. The dry (moist/wet) patches deviate from the domain averaged soil moisture ($\overline{w_{so}}$) by 25 % ($-25\,\%$). This no-bias (C100) set of experiments includes six chessboard patterns with patch lengths of 28 km (C100_028k), 42 km (C100_042k), 56 km (C100_056k), 84 km (C100_084k), 112 km (C100_112k) and 140 km (C100_140k). Note that initial relative soil moisture is identical for all C100 experiments and is also equal to REF. Examples of chessboard patterns are shown in Figure 2.2(d-f). In addition to that, there are similarly set up experiments with a temporal soil moisture anomaly (i.e. large-scale anomaly) is mimicked by a bias of $\pm 25\,\%$ in relative soil moisture (Barthlott et al., 2011a). This setting results in moist-bias experiments with 25 % more domain-averaged initial relative soil moisture (C125), and dry-bias experiments with 25 % less domain-averaged initial relative soil moisture (C075). Heterogeneity length scales are identical to the C100 experiments, and the naming is analogous.

Since the focus in RQ-2 is on the influence of the heterogeneity length-scale, we introduce a control simulation UNI without any gradients in relative soil moisture. The initial relative soil moisture of every soil layer is uniformly replaced by its domain-averaged value ($\overline{w_{so}}$) to create UNI. This control simulation necessary for representative comparison with the chessboard experiments, which then enables conclusions about the influence of soil moisture heterogeneity and its length-scale. While no gradients in relative soil moisture are present (see also Fig. 2.2c) there are still gradients in surface heat fluxes possible as the soil type, and thus abso-

Table 2.1.: List of COSMO-DE experiments indicating the experiments' name (set of experiment (SoE)), bias (B), perturbation length scale (patch size, cutoff length scale, respectively) and a short description of the perturbation. Listed are single experiments, such as the two simulations with a homogeneous bias (Dry Bias B075, Moist Bias B125), the unperturbed reference simulation (REF), as well as the uniform control simulation (UNI). The lower part of the table shows several sets of experiments. The six different chessboard patch sizes are applied to all bias experiments (Chessboard Dry Bias C075, - No Bias C100, - Moist Bias C125). The last group lists the spatially filtered initial conditions comprising a set of high-pass (HP), low-pass (LP) and band-pass filtered experiments with three cutoff length scales in each case.

SoE	**Bias**		**Description**	
B075	0.75	uniform	negatively biased initial soil moisture conditions	
REF	–	–	unperturbed reference simulation	
B125	1.25	uniform	positively biased initial soil moisture conditions	
UNI	–	–	control simulation with initial relative soil moisture uniformly replaced by its domain-averaged value ($\overline{w_{so}}$)	
		Patch sizes	**w_{so} dry patch**	**w_{so} dry patch**
C075	0.75	28 km, 42 km, 56 km,	$(B\ \overline{w_{so}})$ 0.75	$(B\ \overline{w_{so}})$ 1.25
C100	1.00	84 km, 112 km,	$(B\ \overline{w_{so}})$ 0.75	$(B\ \overline{w_{so}})$ 1.25
C125	1.25	140 km	$(B\ \overline{w_{so}})$ 0.75	$(B\ \overline{w_{so}})$ 1.25
		Cutoff length scales	**Description**	
HP	–	10 km, 50 km, 100 km	High-pass filtered initial soil moisture conditions	
LP	–	10 km, 50 km, 100 km	Low-pass filtered initial soil moisture conditions	
BP	–	14 km, 28 km, 56 km	Band-pass filtered initial soil moisture conditions	

lute soil moisture content, is still spatially varying (cf. Fig. 2.1b). Note that initial, domain-averaged relative soil moisture is equal for UNI, REF, and C100 simulations.

The third set of experiments, often referred to as perturbed-parameter ensemble, is intended to bridge the gap from pragmatic soil moisture initialization structures to inaccuracies in the spatial representation of initial soil moisture, which is more relevant for operation. Those experiments are conducted to assess the relative impact of soil moisture perturbation compared to other perturbed-parameter ensembles (see RQ-3). Experiments with spatially-filtered initial soil moisture conditions enable to study the influence of perturbations at particular spatial scales and mimic spatial misrepresentation of soil moisture observations. Spatial filtering is based on a discrete cosine transform. In order to produce the spatially filtered initial conditions, specific wavenumbers are cut off from the spectrum before applying the inverse transform. Three different types of spatial filters are performed, namely, High-, Low-, and Band-pass filters. The band-pass filtered experiments apply windows with a bandwidth of 4 grid cells (i.e. 11.2 km) centered around the respective cutoff scales in order to produce initial conditions comprising specific spatial scales. Note that this bandwidth is close to the effective resolution of 4 to 5 times the horizontal grid spacing whereas smaller scales are not accurately resolved in COSMO (Bierdel et al., 2012). Two band-pass filtered experiments are produced applying the length-scales used in the KENDA system (Schraff et al., 2016). Those cover two orders of magnitude as 10 km (BP010k) and 100 km (BP100k). Additionally, we perform a third band-pass experiment cutting length scales around 50 km (BP050k). We choose this length-scale as a result of the chessboard experiments that are described in Section 3.2. In addition to the three band-pass filtered experiments, we also applied three low- and three high-pass filters. Cut-off length scales for the high- (HP) and low-pass (LP) filters are on scales of 14 km (HP14k / LP14k), 28 km (HP28k / LP28k) and 56 km (HP56k / LP56k). This third set of soil moisture experiments amounts to nine spatially filtered initial soil moisture conditions used to generate an ensemble of soil moisture perturbations. Note that the initial domain averaged soil moisture $\overline{w_{so}}$ remains constant throughout all spatially filtered experiments.

Since the relative soil moisture is restricted to values well below 1, no local oversaturation of the soil is possible, and no extra runoff can be generated (see also $\overline{w_{so}}$ in Table 2.2). No hydrological or atmospheric process is perturbed beyond the initial time, and the soil model can evolve freely during the entire simulation. Keeping the spin-up time short allows for the evaluation of the direct influence initial soil moisture heterogeneity exerts on deep convection. Longer spin-up times would result in a weakening of spatial gradients and blurring of precise length scales. A loss in sharpness of the gradients would hamper the detection of physical mechanisms. After 24 h forecast the soil moisture perturbation pattern is still dominant and only exhibits minimal reductions in magnitude. In total, the three sets of experiments add up to 30 COSMO-DE simulations per case, as summarized in Table 2.1.

2.3.2. Physically-based stochastic Boundary-Layer perturbations

One central task of this thesis is it to assess the relative impact of soil moisture perturbation compared to other perturbation methods. The physically-based stochastic Boundary-Layer perturbations (PSP) for BL turbulence was first described in Kober and Craig (2016); an updated description of this model physics perturbation approach can be found in the appendix of Rasp et al. (2018). The primary motivation follows from the observation that convective triggering in situations of weak synoptic forcing depends crucially on BL turbulence. In km-scale models, convection is treated explicitly while BL turbulence is parameterized. These parametrizations, however, only represent the mean effect of sub-grid turbulence and not fluctuations around the mean, which can be on the same order of magnitude. The PSP scheme aims to re-introduce the missing variability by perturbing the tendencies of temperature, humidity and vertical velocity based on a horizontal random field with a correlation length of five grid boxes, and a temporal correlation of 10 min. The amplitude of the perturbations is scaled to the physical sub-grid variances of the respective variables, which are diagnosed in the 2^{nd} order local closure scheme of the COSMO model (Mellor and Yamada, 1982). From this follows that the most substantial impact of the PSP scheme occurs in situations with considerable BL turbulence, for example on a convective summer day. A PSP ensemble with 20 members, which differ only in their random field, was computed for each day of the high impact weather period (see Sec. 2.6).

The PSP scheme is complementary to the initial soil moisture perturbation as it also causes variability in the BL. Although having temporal and spatial correlations, variability PSP are produced by stochastic noise rather than direct physical processes, such as radiative interactions. Therefore, PSP scheme directly perturbs the BL structure, whereas soil moisture perturbations modify the boundary layer via the surface heat budget.

2.3.3. Perturbation of cloud condensation nuclei

So far, only macrophysical uncertainties affecting the soil atmosphere interaction and BL are considered. Important additional sources of uncertainty are microphysical processes affecting the aerosol-cloud-precipitation interactions. The basis to analyze the effect of aerosols on the precipitation forecast is set by the application of a sophisticated two-moment microphysics scheme (Seifert and Beheng, 2006) in the model setup (see Section 2.2) as it allows for varying the concentration of aerosols in the domain homogeneously. The use of preprocessed activation ratios (Segal and Khain, 2006) facilitates the computation of the activation of CCN from aerosol particles considering the properties of the aerosol and vertical velocity at cloud base. To investigate aerosol-cloud interactions, we conducted experiments with Maritime ($N_{CN} = 100\,\text{cm}^{-3}$, CCN_mar), Intermediate ($N_{CN} = 500\,\text{cm}^{-3}$, CCN_int), Continental ($N_{CN} = 1700\,\text{cm}^{-3}$, CCN_con, reference case), Continental Polluted ($N_{CN} = 3200\,\text{cm}^{-3}$, CCN_pol) conditions. Note that, unless otherwise specified, Continental conditions are used in the experiments as those conditions are most prevalent over Central Europe. Consequently, there is a four-member ensemble containing different aerosol conditions.

Perturbing the aerosol concentration influences, on the one hand, the cloud formation. On the other hand, it affects the earth's surface radiation budget by varied cloud-radiation interactions and thus feeds back to the surface (Betts and Silva Dias, 2010; Fan et al., 2016). In the COSMO configuration, radii of cloud droplets calculated in the microphysics scheme are passed to the two-stream radiation scheme (Ritter and Geleyn, 1992) where they modify radiative fluxes by emission, absorption, and single scattering (Seifert et al., 2012). Aerosol scattering, however, is considered in the radiation scheme but concentrations are based on climatological values (Doms et al., 2011) and are not altered by our perturbations.

2.4. Variability benchmarks

In order to assess the relative impact of the three different perturbation approaches on the HIW period, namely initial soil moisture perturbations, perturbation of aerosol concentration (CCN) and physically-based stochastic Boundary-Layer perturbations (PSP), we introduce two benchmark simulations. Furthermore, radar observations are used to assess the simulations' capability to capture the precipitation during the high impact weather period generally.

2.4.1. Lower variability benchmark ensemble (WNoise)

We designed a lower benchmark ensemble by adding spatially uncorrelated, unbiased Gaussian noise with a standard deviation of 0.01 K to the atmospheric temperature. Similar to the error growth experiments of Selz and Craig (2015), the initial temperature in the entire model atmosphere is perturbed to generate the 10-member WNoise ensemble. The purpose of this WNoise ensemble is to evaluate the relevance of the variability caused by the different types of perturbation. It thus is to ensure that variability is not based on chance but is the result of processes initiated by the considered aspects of uncertainty. The general model setup is equal to the remaining perturbed-parameter ensembles.

2.4.2. Upper variability benchmark ensemble (EPS)

The COSMO-DE-EPS (EPS) is based on the convective-permitting COSMO-DE (see Section 2.2) and has been running operationally between 2012-2017. The forecasting system constitutes the operational 20-member ensemble forecasts of DWD also applied during the HIW period, and is performed using the same domain and grid as our experiments (see also Fig. 2.1). Apart from the double-moment microphysics scheme exclusively applied in our experiments, EPS is similarly set up as our simulations. Henceforth, it also resolves deep convection on a 2.8 km grid and applies the same parameterizations as our model configuration. Since this highly sophisticated ensemble accounts for uncertainties stemming from initial and lateral boundary conditions, as well as deficiencies in the parameterization schemes, it provides an upper benchmark for spatial and ensemble variability caused by our perturbed-parameter ensembles.

The multi-model ensemble is driven by four downscaled global models from DWD (Global Modell Erde, GME), European Centre for Medium-Range Weather Forecasts (ECMWF; Integrated Forecasting System, IFS), National Centre for Environmental Prediction (NCEP; Global Forecast System, GFS) and Japanese Meteorological Agency (JMA; Global Spectral Model, GSM). Next to the uncertainties in lateral boundary conditions, the initial state of atmospheric variables (e.g., horizontal wind components, temperature, cloud water content) is perturbed. Near-surface variables, however, are excluded. Model physics is perturbed by manipulating tunable parameters representing shallow convection, cloud microphysics, BL, and turbulence. Since 2014, initial soil moisture perturbations are implemented in an ad-hoc way for different members in COSMO-DE-EPS. Difference soil moisture fields derived from the COSMO-EU analysis and deterministic COSMO-DE are applied as additive (positive or negative) perturbations. This forecasting system featuring primary sources of uncertainty is initialized twice a day (00 UTC and 12 UTC). More details about the operational forecasting system can be found in e.g. Theis et al. (2015), Kühnlein et al. (2014) or Gebhardt et al. (2011).

2.4.3. Radar observation

The simulations are validated using the Radar Online Aneichung (RADOLAN) quality-controlled radar observations (EY product) provided by the DWD (DWD, 2018a,b). It covers the Central European region with a spatial resolution of 1 km and a temporal resolution of 5 min. The radar-derived observations are coarse-grained to the COSMO-DE grid and cover the entire German subdomain (cf. Fig. 2.1).

2.5. Convective adjustment timescale

The large-scale flow has an important influence on the characteristics of moist convection by determining the required source to trigger convection. For the case of large-scale ascent, conditional instability is formed over large regions and is often collocated with small values of CIN. Conditional instability thus is continuously removed by convection within a short timescale in the order of a few hours and convection can reach an equilibrium state (Done et al., 2006; Keil et al., 2014). In contrast to those synoptically strongly forced conditions, the removal of $CAPE$ is inhibited by large values of CIN during synoptically weakly forced conditions. Triggering of convection relies on mesoscale mechanisms such as convergence lines in the BL, or forced lifting along a slope or cold pools. An equilibrium state of convection is unlikely for those situations (Done et al., 2006).

In order to determine the character of convection, Done et al. (2006) and Keil et al. (2014) introduced an objective measure evaluating the time necessary for the depletion of conditional instability (mean layer $CAPE$) by convective precipitation

$$\tau_c = \frac{CAPE}{d(CAPE)/dt} = 0.5 \left(\frac{L_v g}{\rho_0 c_p T_0} P \right)^{-1} CAPE \tag{2.2}$$

as the ratio between $CAPE$ and its rate of change. Heating of the atmospheric column is mainly responsible for the depletion of $CAPE$. Condensation correlating with the precipitation rate provides a significant contribution to this heating. The rate of change of $CAPE$ can thus be estimated by the expression in brackets in Equation 2.2 containing the precipitation rate (P [kgm^{-2}s^{-1}])) and the constant values of the latent heat of vaporization (L_v), the gravitational acceleration (g), a reference temperature (T_0), the specific heat of air at constant pressure and a reference air density (ρ_0) (Done et al., 2006). The scaling factor 0.5 accounts for the negligence of modifications of the BL in the calculation of $CAPE$ and prevents an overestimation of τ_c (Keil and Craig, 2011).

Assuming that the large-scale synoptic flow evolves within a timescale in the order of $\mathcal{O}$12 h, a threshold to determine the characteristics of convection and the synoptic situation can be estimated. If the value of τ_c is small compared to that timescale, $CAPE$ is quickly removed by convection favoring equilibrium convection and strong synoptic forcing. In contrast to that, similar or longer timescales than $\mathcal{O}$12 h imply that the time necessary to remove instability is longer than its generation. Locally triggered, non-equilibrium convection is accountable for the depletion of $CAPE$ under synoptically weakly forced conditions. Hence, a plausible threshold to categorize the synoptic regime would be between 3 and 12 h (Keil et al., 2014). Following Done et al. (2006); Molini et al. (2011); Kühnlein et al. (2014) or Zeng et al. (2018) a threshold of 6 h is chosen throughout this thesis. A case study is consequently categorized as synoptically weakly forced if the domain-averaged value of τ_c exceeds this threshold once a day.

2.6. Choice of case studies

This thesis analyses the influence of different perturbation methods on 17 precipitating summer cases distributed over four years and featuring different synoptic conditions (Tab. 2.2). The subjective classification was carried out by inspecting weather charts and the spatial distribution of precipitation. Visual inspection showed an intermittent and spotty spatial distribution of precipitation during weakly forced conditions. In contrast, the amount and coverage of domain-averaged precipitation are higher during moderate synoptic forcing. In these cases, the wind speed is generally higher and predominantly westerly, whereas wind velocities are often smaller in magnitude and variable in direction for weak synoptic forcing conditions. The convective adjustment timescale (τ_c; see Section 2.5) is applied as an objective measure to classify the predominant weather regime. Following Kühnlein et al. (2014), a day was classified to be weakly forced if the domain-averaged τ_c exceeds 6 h once throughout a day. Accordingly, the 17 case studies were split into eight weakly and nine moderately forced cases. Furthermore, we incorporate a ten-day episode in 2016 with daily severe thunderstorms in Central Europe as described in Piper et al. (2016) in the selection of case studies.

Note that moderate synoptic forcing will for the sake of brevity often be abbreviated as mod. synoptic forcing. Even though moderate synoptic forcing might seem to be used synonymously to strong synoptic forcing, large-scale synoptic events, like passing cold fronts or strong midlevel troughs, are omitted in this study. By contrast,

Table 2.2.: List of summer case studies indicating the date and mean values averaged over the German subdomain at 12 UTC: the horizontal wind speed and direction in 500 hPa ($\overline{V}$, $\overline{dir}$), the daily accumulated precipitation ($\overline{\text{prec}}$), the fractional coverage of precipitating grid cells exceeding 1 mm (frac) and the daily maximum of the convective adjustment timescale ($\overline{\tau_c}$). The domain-averaged relative soil moisture in the last column ($\overline{w_{so}}$) is averaged over the entire COSMO-DE domain. The low-level humidity index (HI_{low}) and Convective Triggering Potential (CTP) are domain averaged values valid at 06 UTC. The upper part of the table lists case studies categorized as weak synoptic forcing, whereas moderately forced cases are in the lower part. All values are calculated based on unperturbed numerical simulations (i.e. REF). Case studies containing the high impact weather period are highlighted in gray. The two case studies marked with * are additionally simulated with higher model resolution in Appendix A.

Case Study	$\overline{V}$	$\overline{\textbf{dir}}$	$\overline{\textbf{prec}}$	**frac**	$\overline{\tau_c}$	$\overline{w_{so}}$	$\overline{HI_{low}}$	$\overline{CTP}$
30 June 2009*	2.3 ms^{-1}	353°	1.79 mm	4.2 %	31.7 h	0.48	7.6 °C	85 Jkg^{-1}
01 July 2009	3.3 ms^{-1}	32°	1.80 mm	4.3 %	43.3 h	0.49	9.5 °C	138 Jkg^{-1}
20 May 2011	9.2 ms^{-1}	242°	2.14 mm	5.0 %	26.1 h	0.43	10.2 °C	100 Jkg^{-1}
23 July 2013*	5.3 ms^{-1}	294°	1.62 mm	4.1 %	72.1 h	0.35	21.3 °C	228 Jkg^{-1}
04 June 2016	5.3 ms^{-1}	90°	3.55 mm	5.8 %	6.6 h	0.49	8.2 °C	108 Jkg^{-1}
05 June 2016	5.6 ms^{-1}	66°	3.79 mm	6.1 %	13.0 h	0.48	10.0 °C	134 Jkg^{-1}
06 June 2016	1.8 ms^{-1}	19°	1.69 mm	4.4 %	27.2 h	0.47	13.2 °C	150 Jkg^{-1}
07 June 2016	4.8 ms^{-1}	293°	2.58 mm	6.6 %	82.7 h	0.44	16.0 °C	151 Jkg^{-1}
11 Sept 2011	22.9 ms^{-1}	220°	8.04 mm	19.6 %	0.7 h	0.45	14.2 °C	86 Jkg^{-1}
28 July 2013	21.3 ms^{-1}	217°	5.91 mm	8.8 %	1.8 h	0.38	16.1 °C	139 Jkg^{-1}
11 Sept 2013	6.3 ms^{-1}	297°	5.45 mm	10.5 %	1.2 h	0.54	4.4 °C	0 Jkg^{-1}
29 May 2016	9.1 ms^{-1}	165°	9.96 mm	13.2 %	1.4 h	0.47	7.8 °C	111 Jkg^{-1}
30 May 2016	8.3 ms^{-1}	115°	11.25 mm	18.0 %	1.0 h	0.51	4.0 °C	44 Jkg^{-1}
31 May 2016	9.2 ms^{-1}	108°	3.89 mm	5.5 %	2.6 h	0.50	5.8 °C	0 Jkg^{-1}
01 June 2016	8.9 ms^{-1}	61°	9.17 mm	12.6 %	1.0 h	0.51	4.1 °C	22 Jkg^{-1}
02 June 2016	7.0 ms^{-1}	71°	6.42 mm	14.2 %	3.8 h	0.51	4.3 °C	50 Jkg^{-1}
03 June 2016	7.8 ms^{-1}	88°	5.20 mm	7.4 %	4.8 h	0.51	5.1 °C	66 Jkg^{-1}

those synoptic conditions refer to gentle large-scale lifting or increased influence of advection. The distinction of synoptic regimes allows for a focused analysis of interactions between different perturbation approaches, heterogeneity length scales in soil moisture, the strength of background wind, large-scale destabilization of the atmosphere and locally triggered deep convection.

2.7. Fractions Skill Score

A widely used technique to spatially verify quantitative precipitation forecasts compares a forecast and an observation by matching a particular region around the verification point rather than performing a point by point comparison. Such a neighborhood method allows for spatial and temporal inaccuracy in the forecast by considering a neighborhood around the verification point (Ebert, 2008). A famous and very efficiently computable (Faggian et al., 2015) representative is the Fractions Skill Score (FSS) as introduced by Roberts and Lean (2008).

In the first step, a binary field is produced based on a forecast and observation by applying a threshold to both fields. Choosing a precipitation rate (e.g., [mmh^{-1}]) as a threshold enables to assess differences in amplitude and spatial displacement of precipitation whereas a percentile value reduces the effect of bias in precipitation amounts and gives more weight to the spatial accuracy of the forecasts (Roberts and Lean, 2008). A fraction of grid cells exceeding the threshold is then calculated for several squared neighborhood regions with edge lengths of $n = 2N - 1$ with N being the number of grid cells in the largest horizontal, spatial dimension. The fraction of precipitating grid cells above a certain threshold is calculated for each

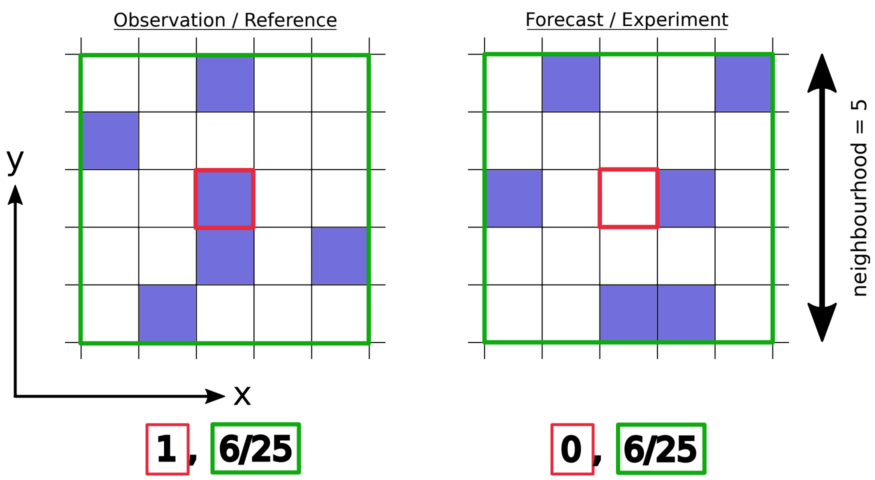

Figure 2.3.: Binary field of precipitation after applying a precipitation threshold. Blue boxes show grid cells with precipitation above a certain precipitation threshold and white boxes illustrate non-precipitating grid cells or those with precipitation below the threshold. The red and green boxes show two different neighborhood sizes. This figure is adapted from Roberts and Lean (2008).

neighborhood size as conceptually illustrated in Figure 2.3. On grid scale, there is no agreement in the two experiments (red box in Figure 2.3) whereas there is a perfect match when considering a larger neighborhood of 5×5 grid cells (green box in Fig. 2.3) (Mittermaier and Roberts, 2010). The squared shape of the filter leads to a dependency on the displacement direction besides the displacement distance (Skok and Roberts, 2016). The effect on the FSS value, however, is small and does not rectify the additional computational cost and complexity of a circular mean filter or Gaussian filter (Roberts and Lean, 2008). The calculation of the FSS is based on the Mean Square Error (MSE) for the wet fractions of the experiment / forecast ($O_{(n),i,j}$) and the reference / observation ($M_{(n),i,j}$)

$$MSE_{(n)} = \frac{1}{N_x N_y} \sum_{i=1}^{N_x} \sum_{j=1}^{N_y} \left(O_{(n),i,j} - M_{(n),i,j} \right)^2 \tag{2.3}$$

for a domain with size $N_x \times N_y$ and neighborhood size $n \times n$. The FSS is then defined relative to the MSE of the worst forecast possible

$$MSE_{(n),ref} = \frac{1}{N_x N_y} \left(\sum_{i=1}^{N_x} \sum_{j=1}^{N_y} O^2_{(n),i,j} + \sum_{i=1}^{N_x} \sum_{j=1}^{N_y} M^2_{(n),i,j} \right) \tag{2.4}$$

by

$$FSS_{(n)} = 1 - \frac{MSE_{(n)}}{MSE_{(n),ref}} \tag{2.5}$$

taking any value between 0 for a forecast with zero skill and 1 for a perfect forecast considering a certain neighborhood and threshold. The value of the FSS is increasing with neighborhood size until it asymptotically converges against 1 for large neighborhood sizes if the forecast is unbiased. This characteristic of the FSS allows defining a spatial scale above which the forecast is considered as skillful. Roberts and Lean (2008) defined this useful scale as the smallest spatial scale n_s where the following holds

$$FSS_{(n_s)} = FSS_{FSSd50} \geq 0.5 + 0.5 f_0 \tag{2.6}$$

(f_0 is the fraction of precipitating grid cells above a certain threshold across the entire domain).

Different studies use other notations depending on the context. On the one hand, studies comparing model simulations with observations refer to that scale as "skillful" scale (e.g., Roberts and Lean, 2008; Mittermaier et al., 2013). Comparing numerical simulations among each, on the other hand, studies use the term "believable" scale (c.f. Dey et al., 2014, 2016). In principle, we will apply the scale in the latter context. However, we will exclusively use the FSS to quantify spatial variability of experiments compared to reference simulations and do not aim for quantification of forecast skill. Thus, in order to prevent confusion, it is appropriate to rename the scale as the spatial dispersion scale ($FSSd$). The spatial dispersion scale describes the spatial scale at which a certain level of spatial variability compared to a reference (quantified by FSS) is reached. In other words, it defines a spatial scale below which the experiments of the perturbed-parameter ensemble deviates from the reference to a certain degree (measured by FSS). This happens by displacement and differences in amplitude of precipitation and thus loses spatial similarity. The equivalent to the "believable" scale would thus be the low dispersion scale $FSSd50$ quantifying the spatial scale below which the spatial agreement of the simulations reduces to a value of $FSS \approx 0.5$. We furthermore propose two additional scales to visualize the change in spatial variability throughout different scales. Similar to the $FSSd50$ defining the scale where the FSS is in the center between a random and perfect forecast, FSS thresholds describing higher spatial agreement between the compared simulations are chosen as the medium ($FSS \approx 0.75$; $FSSd75$) and high ($FSS \approx 0.90$; $FSSd90$) dispersion scales. As a consequence, the three spatial dispersion scales estimate spatial scales at which particular levels low, medium, and high spatial agreement are obtained.

2.8. Assessing the low-level thermodynamic structure

The evolution of the BL, land-surface atmosphere interactions, and thus the triggering of convection, are primarily affected by the thermodynamic structure of the lower troposphere in the early morning. In a framework to evaluate the preferred state of the soil – wet or dry – with regard to triggering convection, Findell and Eltahir (2003a) proposed the usage of the Convective Triggering Potential (CTP) [Jkg^{-1}] and low-level humidity index (HI_{low}) [°C].

The CTP is defined as the area between the environmental temperature and an air parcel lifted moist-adiabatically from a level 100 hPa above ground level (agl) and up to a level 300 hPa agl. This atmospheric layer is likely to be integrated into the growing BL during the day depending on the vertical temperature structure and the heat flux partitioning near the surface. If the surrounding temperature profile is close to the dry adiabatic lapse rate (Γ_d), CTP results in a large, positive value. With respect to the limited duration of daylight, the BL has to grow high enough to reach the LFC quickly. For rapid and deep growth of the BL large portion of sensible heat flux is necessary, which is preferentially the case for dry soil conditions. However, if the environmental temperature is closer to being moist adiabatically but still unstably stratified, values of CTP are smaller positive values as compared to the case above. Those conditions require a lowering of the LFC by a growth in equivalent potential temperature (θ_e) which is closely linked to the moisture content of the air. Wet soil and BL conditions favor this scenario by an increase of latent heat flux manifesting in an increase of Moist Static Energy (S_e) within the BL. To describe the moisture content of the BL more closely, Findell and Eltahir (2003a) additionally applied the HI_{low}. The dew point depressions computed 50 hPa agl and 150 hPa agl are aggregated

$$HI_{low} = \left(T_{P_{surf}-50\,\mathrm{hPa}} - T_{d;P_{surf}-50\,\mathrm{hPa}}\right) + \left(T_{P_{surf}-150\,\mathrm{hPa}} - T_{d;P_{surf}-150\,\mathrm{hPa}}\right) \quad (2.7)$$

to form a simple metric describing the moisture content in the BL.

Analyzing atmospheric soundings from several summer periods across the United States, Findell and Eltahir (2003a,b) developed thresholds distinguishing conditions favoring wet-, or dry-couplings, transitional region, as well as atmospherically controlled convection as shown in Figure 2.4. Surface-based triggering of convective precipitation thus generally requires an unstable atmosphere (i.e. positive values of CTP) and sufficient moisture content in the lower atmosphere. For intermediate values of HI_{low} (approximately $5\,°\mathrm{C} \leqslant HI_{low} \leqslant 10\,°\mathrm{C}$) convective precipitation is more likely to be triggered over wet soils. Low and intermediate values of CTP are sufficient under those conditions. The requirements to initiate convection over dry soils are high values of HI_{low} (approximately $10\,°\mathrm{C} \leqslant HI_{low} \leqslant 15\,°\mathrm{C}$), as well as large instability (i.e. CTP larger than approximately $200\,\mathrm{Jkg}^{-1}$). Note that those regions are representative for the region of the United States and may not be applicable to other regions (Findell and Eltahir, 2003a; Ferguson and Wood, 2011; Roundy et al., 2012). The values listed here thus provide a feeling of low, intermediate, or high values rather than providing precise thresholds.

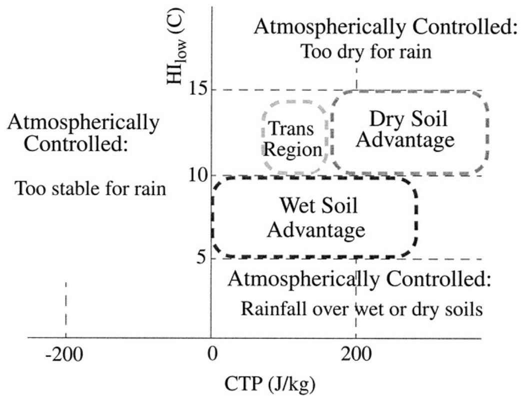

Figure 2.4.: Categorization of surface based initiation of convective precipitation depending early-morning atmospheric conditions and soil moisture conditions using CTP (x-axis) and HI_{low} (y-axis). Four convective regimes are represented: atmospherically controlled, wet soil advantage, dry soil advantage and a transition region. This figure is taken from Findell and Eltahir (2003a).

3. Results

This chapter consists of three sections, each contributing to one of the three research questions posed in the introduction (Section 1.4). It starts introducing a homogeneous bias in initial soil moisture conditions of several weakly and moderately forced cases (Section 3.1). Those bias perturbations will then be combined with soil moisture perturbations with different heterogeneity length-scales using chessboard patterns (Section 3.2). Finally, Section 3.3 applies more realistic initial soil moisture perturbations to produce a perturbed-parameter ensemble and to elaborate on the relative impact compared to other major sources of uncertainty for convective initiation and formation of precipitation including stochastic BL and CCN perturbations.

3.1. Influence of initial soil moisture bias on convective precipitation

To get a first impression of the model's sensitivity to soil moisture perturbations the following section will evaluate the influence of a bias in initial soil moisture for different synoptic regimes (see RQ-1 posed in Section 1.4). We apply homogeneous initial soil moisture bias of $\pm 25\,\%$ to eight weakly and nine moderately forced case studies. By doing that, we will extend the small body of literature dealing with SMP coupling on a diurnal time scale by focusing on the influence of the synoptic situation and orographic characteristics of the surface.

3.1.1. Changes in precipitation rate

Since the partitioning of surface heat fluxes is mainly driven by soil moisture content, its perturbations will first manifest in sensible and latent surface heat fluxes. The distributions of the sensible surface heat fluxes evaluated for a synoptically weakly forced case study (i.e. 6 June 2016) are shown in the first row of Figure 3.1. A clear diurnal cycle is visible for all three experiments (B075 (a), Ref (b), B125 (c)) while the peak values (12 UTC) increase (decrease) by 35 % when decreasing (increasing) the initial soil moisture content in the domain. However, relative to the absolute numbers, the spread of the values remains similar for the three simulations. Latent surface heat fluxes (second row in Fig. 3.1) reveal a reversed behavior. Peak values of latent heat flux decrease (increase) with increasing (decreasing) initial soil moisture in the domain. Unlike the sensible heat fluxes, the change in absolute values of the medians is not linear. A reduction in soil moisture reduces latent heat fluxes by about 30 %, whereas an increase only translates into a 21 % increase of

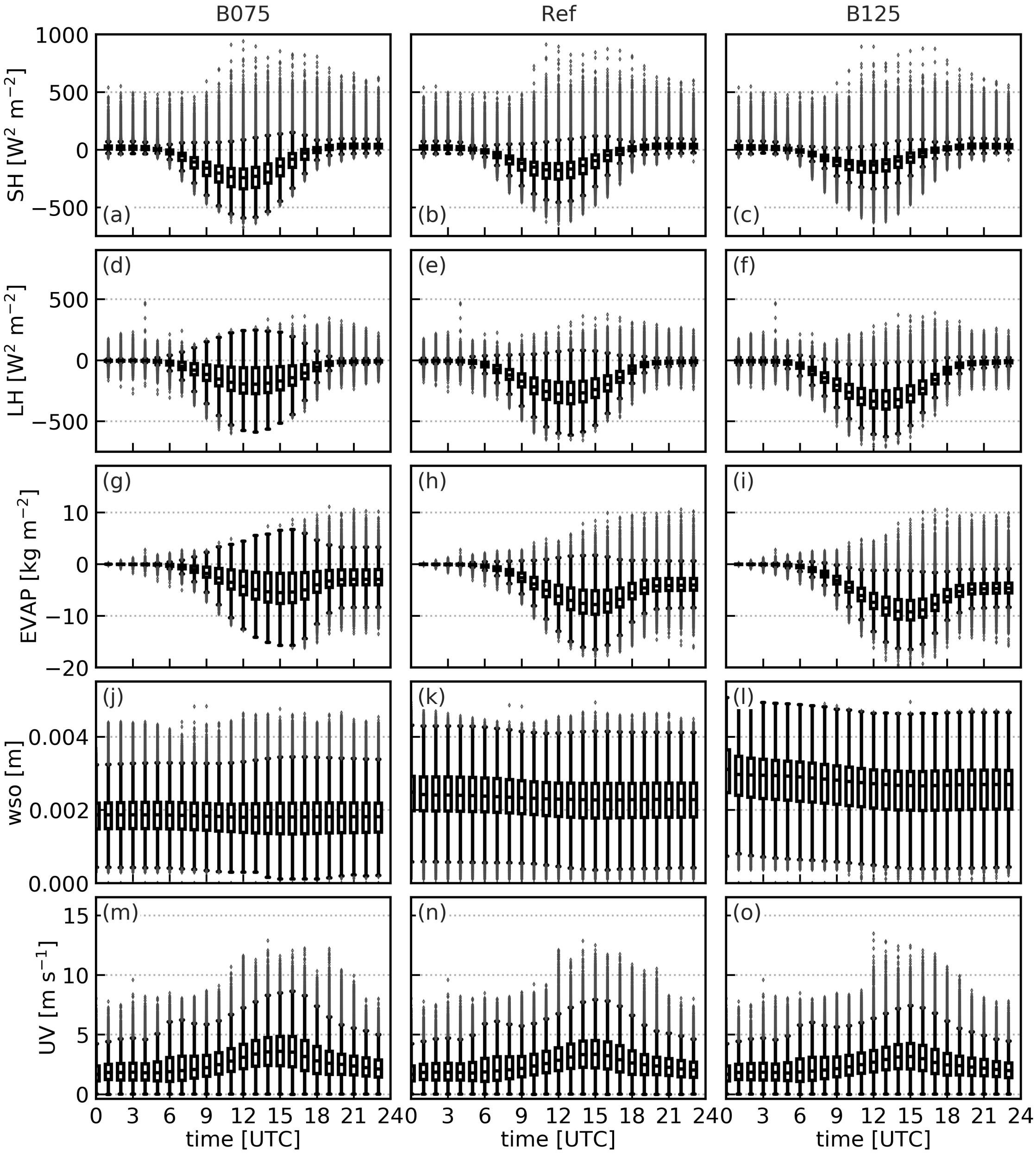

Figure 3.1.: Time series of box-whisker plots showing the distributions of sensible surface heat flux (a-c) latent surface heat flux (d-f), surface evaporation (g-i), absolute soil moisture (j-l) and horizontal wind at 10 m a.g.l. ($uv = \sqrt{u^2 + v^2}$, m-o). The dry bias experiment (B075) is shown in the first, reference simulation in the second and the moist bias experiment (B125) in the last column. Boxes represent the lower (25 %) and upper (75 %) quartile whereas the whiskers are defined as 1.5 times the interquartile range. Points outside this range are considered as outliers. Lake- and sea-areas are excluded from the computations. Evaluations are performed for a synoptically weakly forced case (06 June 2016).

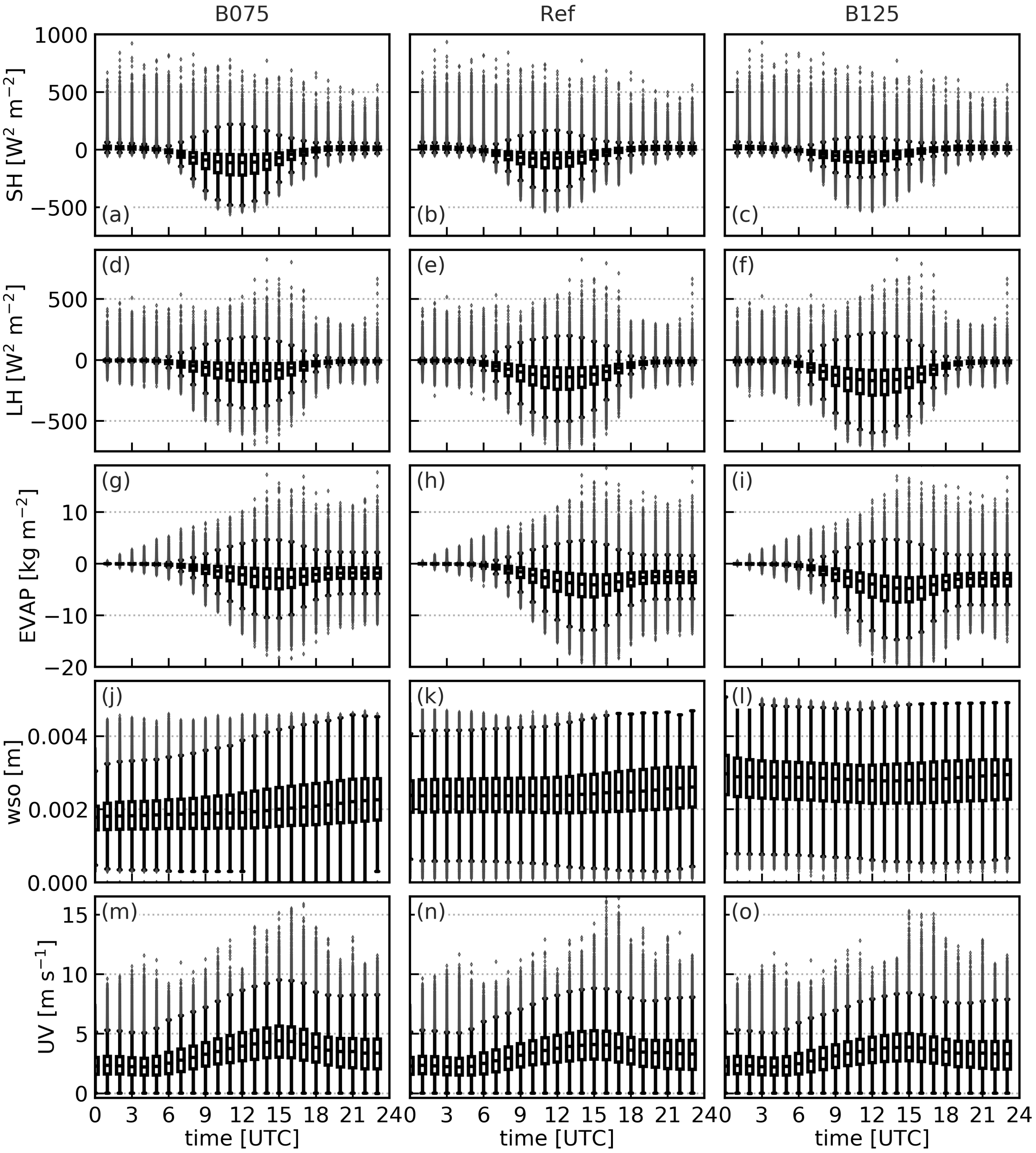

Figure 3.2.: Same as in 3.1 but evaluated for a synoptically forced case (29 May 2016).

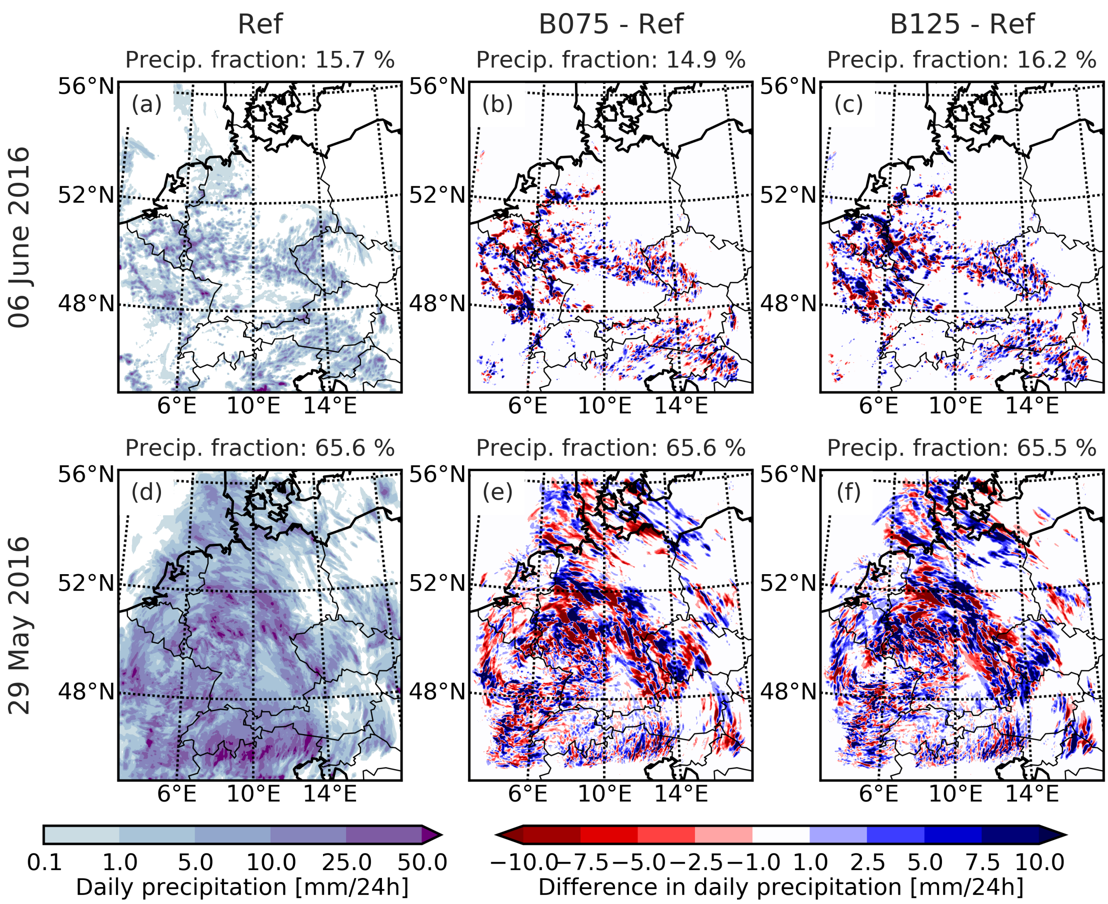

Figure 3.3.: Daily accumulated precipitation for reference simulations (a, d), as well as differences between dry bias experiments (b, e) / moist bias experiments (c, f) and the respective reference simulation. Computations are depicted for 06 June 2016 (a-c) and 29 May 2016 (d-f). The fraction of precipitating grid cells exceeding a daily value of 1.0 mm/24h is listed above each graphic.

latent heat. Similar values are valid for the changes in surface evaporation (Fig. 3.1 (g-i)). As the net radiation at the surface remained similar, this hints on the transition from a moisture-limited (B075, Ref) to an energy-limited (B125) evaporation regime. Consequently, further moistening of the soil would not significantly increase evaporation. Similar behavior is true for domain averaged values (not shown). Inversely to the median and average values, the spread in latent heat flux, as well as surface evaporation, increases with decreasing initial soil moisture. In combination with the small absolute values, the increased spread in evaporation leads to an increase in the spread of the absolute soil moisture values and a moderate increase in domain averaged soil moisture throughout time (Fig. 3.1(j)). High evaporation rates for the positively biased initial soil moisture experiments lead to a continuous drying of the soil during the day. The increased sensible heat fluxes in the dry bias experiment lead to higher surface wind speed (Fig. 3.1m) whereas magnitudes of horizontal wind decrease with increasing initial soil moisture (Figs. 3.1m-o).

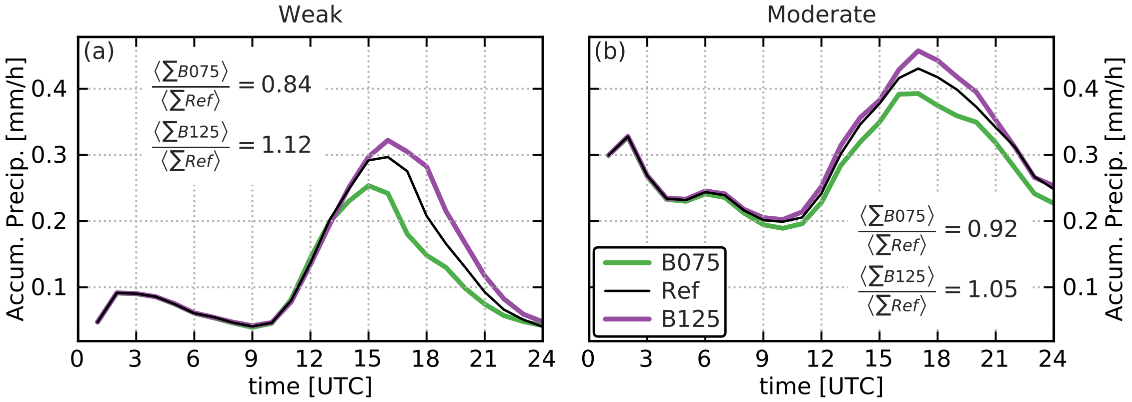

Figure 3.4.: Time series of domain averaged hourly precipitation evaluated for the dry bias (B075, green), reference (Ref, black) and moist bias (B125, magenta) experiment averaged over all synoptically weakly (a) and moderately (b) forced case studies listed in Table 2.1. The average ratios between the aggregated precipitation between 09 h and 21 h of each bias experiment, and the related reference simulation are listed within the respective figure.

The synoptically moderately forced case differs from the weakly forced case examined above by larger fractional coverage of precipitation (comparing 06 June and 29 May 2016 in Table 2.2). Compared to 06 June 2016, a reduction of surface heat fluxes (i.e. sensible + latent heat flux) by about 40 % is evident in Figure 3.2. Even though the absolute values of heat fluxes are smaller during moderate synoptic conditions, the relative change for altering initial soil moisture is comparable to the weakly forced case. While sensible heat fluxes decrease by about 30 % when increasing the initial soil moisture (Figure 3.2 b, c), the evaporation only experiences an increase by 22 % (Figure 3.2 h, i). This behavior again hints on a transition from moisture-limited to the energy-limited regime from Ref to B125. Interestingly, the upper quartile (75$^{\mathrm{th}}$ percentile) remains similar for the three experiments (Figs. 3.2(g-i)) whereas the lower quartile (25$^{\mathrm{th}}$ percentile) decreases with increasing initial soil moisture. The less efficient evaporation for the dry bias experiment leads to moistening of the soil by about 25 % after 24 h simulation time probably caused by precipitation. The domain averaged absolute soil moisture hardly changes during the moist bias experiments as the increased amount of negative evaporation values can compensate for a large amount of positive evaporation values. Finally, surface winds are generally higher as compared to the weakly forced case (Fig. 3.1) but similarly reveals higher magnitudes with higher values for the dry bias experiments (along with higher sensible heat fluxes, m) and lower magnitudes for the moist bias experiments (o).

Figure 3.3 indicates a noticeable difference in the precipitation fields of different synoptic forcing conditions. The weakly forced case shows local convective cells, whereas precipitation covers larger areas for the moderately forced case. Consequently, the fraction of precipitating grid cells is smaller for weak synoptic forcing (15.7 %) as compared to the moderately forced case (65.6 %). Furthermore, precipi-

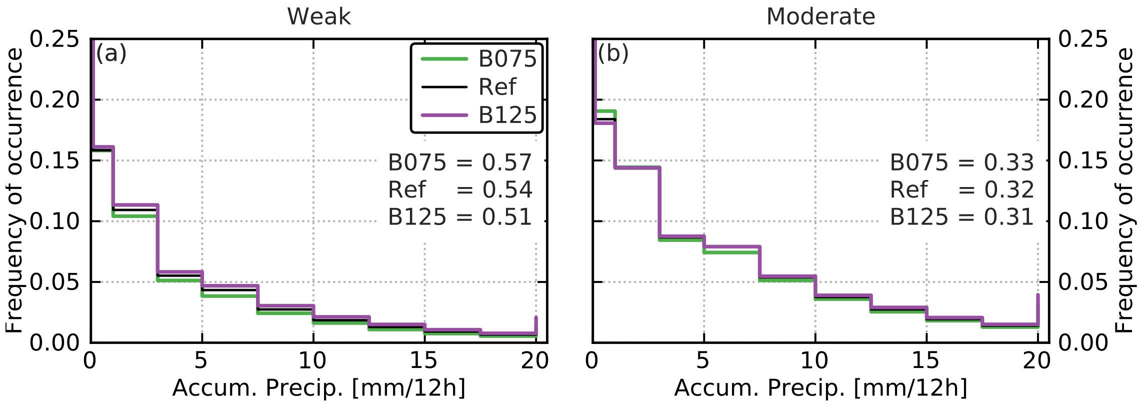

Figure 3.5.: Histogram of precipitation accumulated between 09 h and 21 h incorporating all weakly (a) and moderately (b) forced case studies evaluated over the German subdomain for dry bias (B075, green), reference (Ref, black) and moist bias (B125, magenta) experiments. The fraction of non-precipitating grid cells is listed within the respective figure.

tation amplitude is also increased for moderate synoptic forcing. Those findings are also evident for the remaining case studies listed in Table 2.2. When comparing the effect of the bias experiments, both, the areas covered by the differences in precipitation (b, c, e, f) and the fraction of precipitating grid cells remain similar in both case studies. Due to the increased influence of surface heat fluxes in the weakly forced case, there is a slight change in precipitating area in the order of 1 % (a-c) whereas there is hardly any change for the moderately forced case (d-f). Furthermore, changes in daily precipitation relative to the absolute values of the reference simulations are larger for the weakly forced case. A redistribution and amplification of precipitation are thus more evident than changing the location of convective cells.

Comparison of the two exemplary case studies thus hints on a larger influence of a bias in initial soil moisture on surface heat fluxes and precipitation during weakly forced weather regimes. To quantify the average influence of an initial soil moisture bias on precipitation, Figure 3.4 depicts the domain-averaged hourly rainfall averaged over all weakly (a) and moderately (b) forced cases. Comparing the two synoptic regimes again reveals generally higher precipitation rates for moderate synoptic forcing. The simulations are similarly stratified for both synoptic regimes with the moist bias experiments showing the highest and the dry bias experiment showing the smallest precipitation rates. However, the diurnal cycle peaks one hour earlier (i.e. 15 UTC) in the dry bias experiments as compared to the reference and moist bias simulations (i.e. 16 UTC). Artificially high precipitation rates during the first simulation hours are due to the fact that we used downscaled analysis data for the simulations leading to spin-up effects. We, therefore, omit the time before 05 UTC for the calculation of aggregated precipitation amounts spin up effects might still act before that time. Furthermore, no solar radiation is apparent to induce differences in surface heat budget before that time. Aggregated precipitation amounts support the larger impact of initial soil moisture bias for weakly forced conditions on average reducing (increasing) aggregated precipitation by 16 % (12 %) for a dry (moist) initial bias (Fig. 3.4a). In contrast to that, moderately forced cases only show a reduction (increase) in aggregated precipitation by 8 % (5 %) for a dry (moist) initial bias (Fig. 3.4b). This difference again shows the nonlinear impact of a moist and dry bias in initial soil moisture on precipitation as moist bias experiments show smaller impact as dry bias simulations compared to the unperturbed reference.

Similar to the modulation of accumulated precipitation described above and supported by Figure 3.3, the fraction of non-precipitating grid cells listed in Figure 3.5 is more sensitive to initial soil moisture bias during weak synoptic forcing. Fractional coverage of precipitation is not only increasing by 6 %, but the frequency of occurrence in each precipitation bin is also increasing for B125 as compared to B075 (Fig. 3.5a). Both effects, however, are reduced for moderate synoptic forcing. Consequently, the histograms in Figure 3.5b are very similar, and the fraction of non-precipitating grid cells differ just a little. Note that the histogram depicted in Figure 3.5 is based on all real-case studies and both bias experiments. This large database increases the reliability of small differences between the experiments. In general, however, the dry fraction is smaller for moderate synoptic forcing ($\approx 30\,\%$) as for weak synoptic forcing ($\approx 50\,\%$). While the change in the number of dry grid cells is approximately linear considering the 12-hour period, the modification of an initial soil moisture bias causes in each precipitation bin is not linear. A dry bias more drastically reduces the precipitation of a particular bin, whereas a moist bias increases it.

3.1.2. Spatial variability caused by initial soil moisture bias

The previous paragraphs suggest that precipitation differences stem from amplification of different convective cells rather than from variations of the basic precipitation pattern. To assess the influence of a soil moisture bias on the spatial variability of precipitation, we use the FSS at a scale of 30.8 km (i.e. 11 grid cells). For our application, a decreasing FSS does not relate to a loss in skill but to increased spatial variability. Comparing the two synoptic conditions, the increase in variability is approximately one hour earlier (i.e. 9 UTC) for weakly forced cases, as shown in Figure 3.6a. Additionally, the decrease rate is slightly steeper for weakly forced conditions leading to generally higher spatial variability and a more pronounced influence of soil moisture perturbations. The average low dispersion scale ($FSSd50$) depicted in Figure 3.6d describes the spatial scale at which a spatial variability corresponding to $FSS \approx 0.5$ is reached. The low dispersion scale shows good accordance between the bias experiments and the reference simulation until noon. Substantial differences arise in the time when spatial variability starts to increase. During weak synoptic forcing, spatial variability on average starts to increase at about 13 UTC and approximately 3 h before the moderately forced cases. Spatial scales where the simulations are considerably dissimilar to the reference are almost double for weak forcing. The strong soil-atmosphere interaction for weakly forced cases leads to a redistribution of convection over Germany, lowering the FSS. Spatial variability

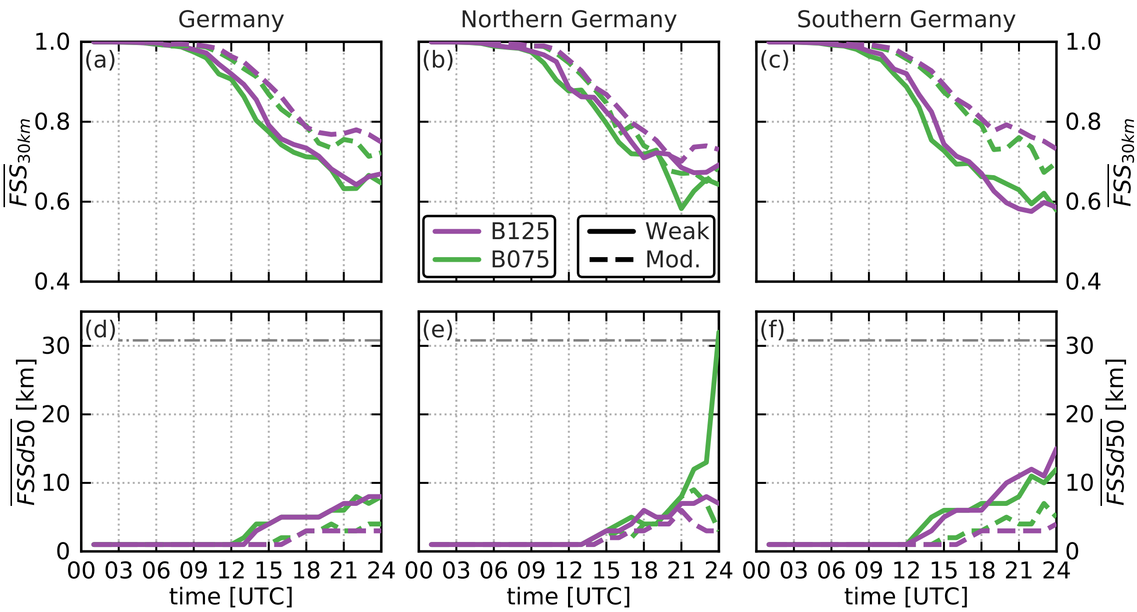

Figure 3.6.: Time series of Fractions Skill Score (FSS) (upper row, a-c) and low dispersion scale (lower row, d-f) relative to the reference simulation averaged over all weakly (solid) and moderately (dashed) forced case studies listed in Table 2.2. Calculations were performed for B075 (green) and B125 (magenta) experiments using the 95$^{\text{th}}$ percentile precipitation as threshold. The spatial scale for the FSS is 11 grid cells (30.8 km). Evaluations are depicted for the German (a,d), Northern-German (b,e) and Southern-German (c,f) subdomains. See Figure 2.1 for the definition of subregions.

is increased, and bias perturbations affect the forecast earlier in the case of weak synoptic forcing. Nevertheless, $FSSd50$ remains below 10 km for both synoptic conditions, which is considered as small spatial variability.

Dividing the German subregion into a fairly flat northern part (Fig. 3.6(b,e)) and a mountainous southern part (Fig. 3.6(c,f)) reveals both, regional differences and the importance of orography. Spatial variability is slightly more pronounced for the dry bias as compared to the moist bias experiments as the green (B075) lines mostly show smaller values as the magenta lines (B125). Differences arise from the comparison of the synoptic situations in the two subdomains. While weak synoptic forcing evokes only slightly higher spatial variability over northern Germany (Fig. 3.6b,e), differences are more pronounced over the southern part (Figs. 3.6c,f). Estimations of the low dispersion scale in Figure 3.6f reveal about 5 km during moderate forcing whereas weakly forced cases display an earlier and steeper increase resulting in scales of about 10 km. Thus, the sensitivity to the synoptic regime is larger over the orographically structured Southern subdomain. The absence of orographic trigger mechanisms explains the relatively larger influence of initial soil moisture perturbations over the flat Northern subdomain during weak synoptic control.

3.1.3. Discussion and summary

The previous section showed the influence of a bias in initial soil moisture on convective precipitation by evaluating several case studies with positively (negatively) biased initial soil conditions. Concerning the real-case application of those experiments, we interpret the bias as a temporal (seasonal, climatological) or large-scale anomaly. Inclusion of the synoptic regime as an essential factor in the SMP coupling is similarly innovative as the amount of included case studies involved in a study focusing on short-range forecasts of convective precipitation.

Regime dependent, nonlinear SMP coupling

Evaluating the average precipitation time series of eight weakly and nine moderately forced cases in Figure 3.4 on average showed a positive SMP coupling for large-scale initial soil moisture anomalies. Decreased initial soil moisture results in a decrease in domain averaged precipitation and vice versa. This is in good accordance to existing literature evaluating long-range forecasts of monthly precipitation over Europe by, e.g., Schär et al. (1999) or Gallus and Segal (2000).

Looking closely, accumulated precipitation is more sensitive to a negative bias for both synoptic conditions. We relate this observation to differences in surface heat budget. Figures 3.1 and 3.2 show surface heat fluxes, as well as evapotranspiration comparing the bias experiments with the reference simulation for a typical weakly and moderately forced case. The comparison reveals a more pronounced decrease (increase) in sensible (latent) surface heat flux for a negative bias as compared to the increase (decrease) in sensible (latent) for increasing initial soil moisture. This correlates with the nonlinear behavior of the SMP coupling. We found the reasoning for that in the moisture content of the soil defining the magnitude plant transpiration. Below a certain soil moisture content, transpiration linearly correlates to soil moisture. For very moist overall soil conditions, transpiration does not further increase with increasing soil moisture. As the incoming solar radiation is equal for the experiments of the same case study, the evaporation regime is changing from moisture to energy-limited. In other words, transpiration is not further increasing as the stomata of the plants are opened maximally. This directly feeds back on the precipitation and leads to a nonlinear SMP coupling. Additionally, the histograms shown in Figure 3.5 shows a linear behavior in the modification if dry grid cells but, comparing to the reference simulation, reveal less change for B125 as for B075 for each precipitation bin. Consequently, we find a nonlinear but positive SMP coupling. A case study performed by Barthlott and Kalthoff (2011) supports this behavior. They gradually increase initial soil moisture from $-50\,\%$ to $50\,\%$ in steps of $5\,\%$ over a small region in southern Germany. For dry anomalies, they found a linear increase in daily accumulated precipitation with increasing soil moisture whereas the increase rapidly decayed for moist anomalies. Pal and Eltahir (2001) found similar nonlinearity simulating two summer periods with altering initial soil moisture content over the Central United States.

Next to the sign and nonlinearity of average SMP coupling, Figure 3.4 reveals a different magnitude of the bias influence depending on the synoptic situation. By evaluating several case studies, we found a larger influence of initial soil moisture bias for weak synoptic forcing. A glance in the synoptic preconditioning summarized in Table 2.2 reveals reduced domain averaged CTP and either high or low low-level humidity (HI_{low}) which hints on reduced importance of soil-related trigger mechanisms. The surface heat budget is another crucial factor distinguishing the synoptic situations and shows smaller heat fluxes for moderate synoptic forcing (see Figs. 3.1 and 3.2). Less energy leads to smaller absolute energy gradients between differentially heated surfaces caused by differences in soil moisture and a reduction of surface-induced BL heterogeneities. Those factors do not favor a dominant role of the surface in triggering convection. Furthermore, increased average wind speeds shown in Table 2.2, as well as Figures 3.1 and 3.2 suppress the vertical growth of BL anomalies and emphasize the influence of advection. In other words, main trigger mechanisms of convection are based on large-scale effects, such as synoptic lifting.

Regional differences in SMP coupling

Assessing the spatial variability applying the FSS reveals a regime dependent behavior with larger variability for weak forcing. Strong soil-atmosphere interaction over both subdomains results in an increased spatial impact of homogeneous soil moisture perturbations during weak synoptic control (Fig. 3.6). This interaction leads to a redistribution of convection and impacts the spatial structure of the precipitation field, resulting in lower FSS. The impact is generally smaller during moderate synoptic forcing. Nevertheless, spatial variability is considered small for the bias experiments, whereas a soil moisture bias predominantly influences the intensity of the precipitation.

Dividing the German subdomain into a northern and southern part in Figure 3.6 additionally shows pronounced regional differences in the regime dependent SMP coupling with a stronger influence of the synoptic conditions over the south. Assuming that the atmospheric conditions are similar for the two subdomains, the main difference between the subdomains is orography. The strong soil-atmosphere interaction during weak synoptic forcing leads to a similar impact of homogeneous soil moisture perturbations over both subdomains. For moderate synoptic forcing, however, orography plays a more important role in varying the initiation of convection, whereas soil moisture is more important during weak synoptic forcing. Indication for differences stemming from the initiation phase is given by the steeper decrease in FSS and low dispersion scale between 09 h and 15 h (Fig. 3.6c,f). Thus, orography acts as a powerful trigger mechanism and by doing that suppresses the effect of perturbed soil moisture. This emphasizes the importance of synergistic interactions between soil orography and convective precipitation.

This section supports a positive SMP coupling sign but suggests that daily accumulated precipitation is nonlinearly dependent on domain-averaged latent surface heat flux. Nonlinearity mainly arises from the evaporative regime of the soil. The intensity of the coupling is dependent on the synoptic regime and the orography.

Although this section shows a good correlation between large-scale evaporation and precipitation, small-scale processes are crucial for the initiation of convection and thus for the response of convective precipitation on changes in initial soil moisture. Consequently, the questions arise whether results described above are sensitive to the model resolution and correlations change with finer model resolution and, thus, an improved representation of those small-scale processes. To investigate the importance of the grid spacing, we repeat the bias experiments for two exemplary case studies with COSMO simulations at 500 m model resolution in Appendix A. Those experiments show a slightly quicker response of domain-averaged precipitation with increased model resolution. The net effect of an earlier increase (decrease) of precipitation for dry (moist) initial soil moisture bias combined with an earlier decrease (increase) in the evening leads to a slightly reduced overall impact as compared to low-resolution simulations. However, it is hard to determine whether differences arise from the increased model resolution or the more sophisticated turbulence scheme was applied in the high-resolution simulations.

Furthermore, this section only covers homogeneous soil moisture perturbations but does not account for the influence of the heterogeneity length-scale and dominant processes captured by the model. The following section will, therefore, build on the general idea of a domain averaged soil moisture bias but replaces natural soil moisture heterogeneity by pragmatic chessboard patterns with varying tile sizes. This setting allows us to examine mechanisms influencing convection initiation and a scale-dependent SMP coupling by simulating the collective impact of heterogeneous and homogeneous soil moisture perturbations.

3.2. Influence of soil moisture heterogeneity on the initiation of moist convection

In the previous section, we found a nonlinearly positive, regime-dependent correlation between a homogeneously distributed initial soil moisture bias and precipitation. This setting, however, cannot give implications for the influence of soil moisture heterogeneity on different spatial scales on magnitude and sign of the SMP coupling. Furthermore, the setting does not allow to study scale-dependent and dynamical processes that are implicitly acting when soil moisture heterogeneity is present. As the representation of those mechanisms on currently used convective-scale weather models are still under debate, we will combine the setting used in the previous section with variously sized chessboard patterns. Therefore, we introduce several chessboard patterns superposed with a domain averaged bias in the initial soil moisture. This setting allows us to investigate the collective influence of spatially sharp soil moisture gradients and soil moisture bias of $\pm 25\,\%$ on the SMP coupling. This experimental setup is tailored to answer the research question RQ-2.

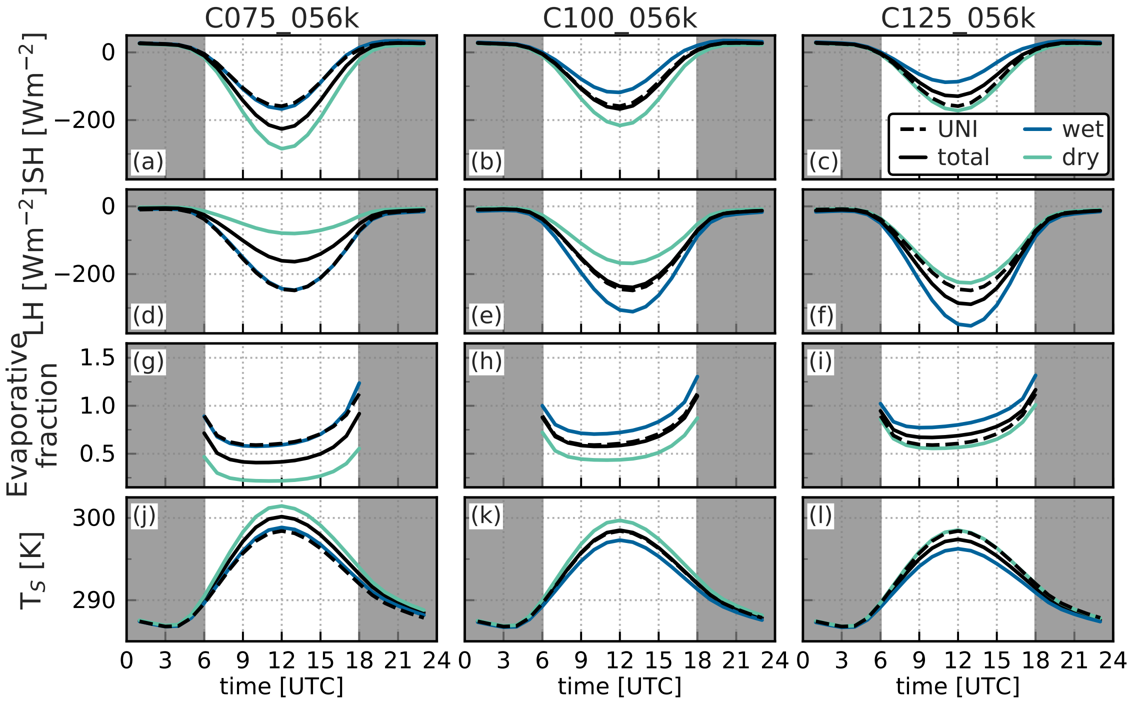

Figure 3.7.: Time series of average sensible surface heat flux (a-c), latent surface heat flux (d-f), evaporative fraction (g-h) and surface temperature (j-l). The UNI (dashed, black), C075_056k (first column), C100_056k (second column) and C125_056k (third column) experiments of eight weakly forced cases are incorporated into the average. Evaluations for the heterogeneous simulations are shown for the entire domain (black, solid), wet (blue) and dry (green) patches. Lake and sea areas are excluded from the computations. The gray shaded areas mark the timespan where sensible heat flux in UNI on average is not negative.

3.2.1. Influence on surface fluxes

As already discussed in the previous Section 3.1, soil moisture anomalies first manifests in surface fluxes. Therefore, this section begins with elaborating on the combined impact of soil moisture heterogeneity and bias on the surface heat budget. The prescribed chessboard patterns group the experiments into three sets defined by the initial bias (C075, C100, C125). Starting with a medium patch size of 56 km, average surface heat fluxes show a nonlinear behavior with the sensible (latent) surface heat fluxes changing by about +47 % (−33 %) in C075_056k (Figure 3.7(a,d)) and changing by about −19 % (+15 %) in C125_056k (Figure 3.7(c,f)) compared to the uniform control simulation (UNI), respectively. The impact of soil moisture perturbations on domain-averaged sensible and latent surface heat fluxes in the C100_056k experiments, however, is negligible. While the sign of the changes in surface heat fluxes goes in the expected direction, the magnitude of the soil moisture perturbations relates nonlinearly to the surface fluxes. The nonlinearity again hints on changing evaporation regimes from moisture to energy-limited. Not only the fraction of energy transferred into evaporation (Figure 3.7(g-i)) increases with

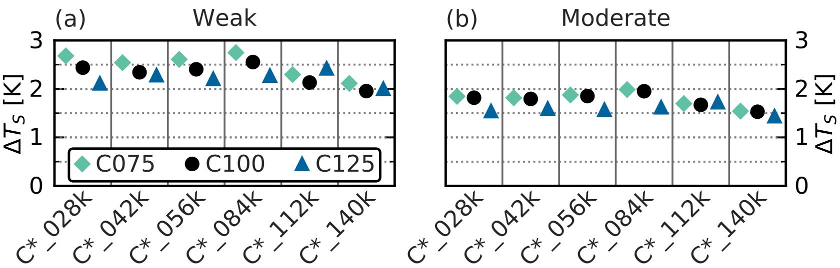

Figure 3.8.: Average difference in midday surface temperature between wet and dry patches ($\langle T_{S,dry}\rangle - \langle T_{S,wet}\rangle = \Delta T_S$) evaluated for the C075, C100, C125 experiments and averaged over seven weakly (a) and nine moderately (b) forced cases.

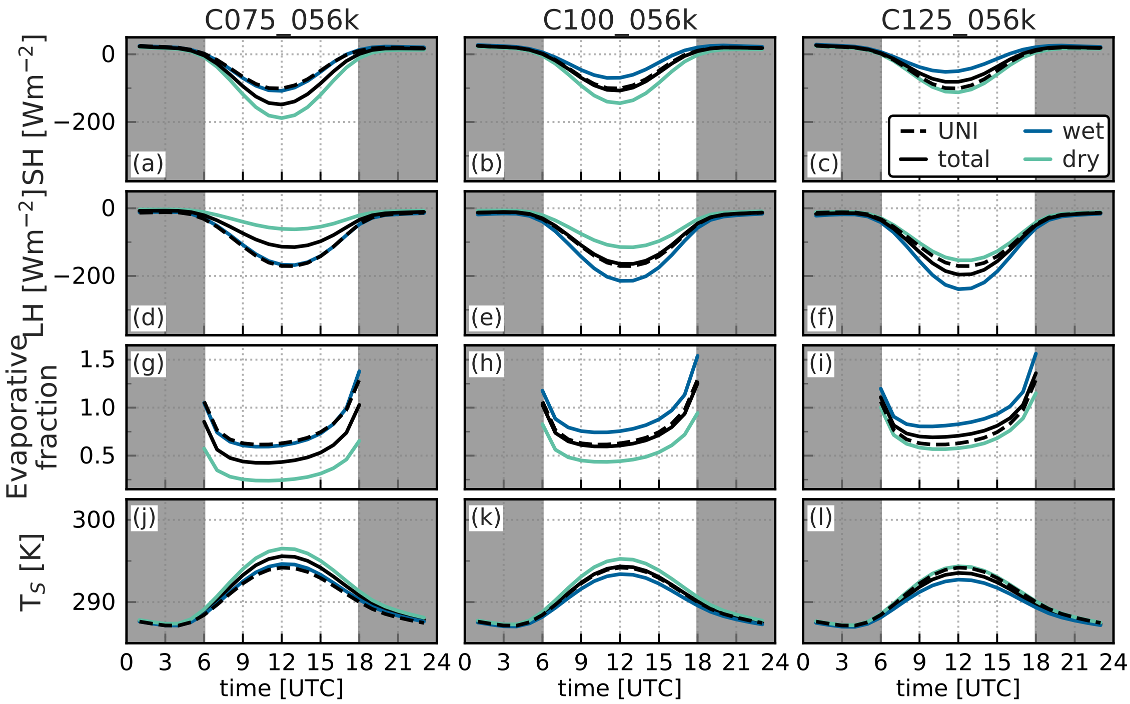

Figure 3.9.: Same as Figure 3.7 but evaluated for nine moderately forced cases.

increasing overall soil moisture, but the phase difference between peak latent and sensible fluxes slightly increases. Sensible heat fluxes reach their peaks earlier with increasing soil moisture whereas a slight delay is visible for latent heat fluxes. This can also be deduced from the increasing asymmetry of the evaporative fraction with increasing soil moisture. Time series of the surface temperature (Figure 3.7(j-l)) shows the close correlation between the magnitude sensible heat flux and temperature. Therefore, the midday surface temperature also shows a nonlinear response to bias perturbations in soil moisture. Simulations reveal an average change in midday surface temperature by +1.62 K (−1.08 K) when decreasing (increasing) domain averaged initial soil moisture compared to UNI, respectively. Similar to surface heat fluxes, temperature differences between UNI and C100_056k are negligible. Since Figure 3.7j-l only show three chessboard experiments, Figure 3.8(a) depicts differences in surface temperature between wet and dry patches for all three sets of experiments. The average difference of about 2.5 K compares well with land surface temperature anomalies during the initiation of moist convection in Europe (Taylor, 2015). Differences in surface temperature are systematically larger (smaller) for increased (decreased) overall initial soil moisture. The persistent behavior of temperature differences suggests that the influence of heterogeneous soil moisture perturbations on surface fluxes described above also hold for different patch sizes. The influence, however, is reduced for the large patch size (112 km & 140 km).

Similar to the simple bias experiments examined in the previous Section 3.1, moderately forced cases reveal smaller absolute values for sensible and latent heat fluxes. The relative change, however, is very similar for both synoptic conditions as moderately forced cases on average reveals sensible (latent) surface heat fluxes increasing (decreasing) by about 42 % (34 %) in C075_056k (Figure 3.9(a,d)) and decreasing (increasing) by about 18 %(17 %) in C125_056k (Figure 3.9(c,f)) compared to UNI, respectively. The no-bias simulations show, similarly to the weakly forced cases, an increase (decrease) of sensible (latent) heat fluxes in the order of 5 %. This is also why the evaporative fraction hardly changes between the two synoptic situations, as Table 3.1 shows. According to this table, evaporative fraction ranges between

Table 3.1.: Average evaporative fraction evaluated at 12 UTC for weak (left part) and moderate (right part) forcing. C075_056k, C100_056k and C125_056k experiments are considered. Values are listed for the total domain (first row), wet (second row) and dry patches (third row). Lake and sea areas are excluded from the computation. Values correspond to the time series of the evaporative fractions in Figures 3.7(g-i) and 3.9(g-i).

	Weak			Strong		
	C075_56k	C100_56k	C125_56k	C075_56k	C100_56k	C125_56k
total	0.42	0.59	0.69	0.43	0.61	0.71
wet	0.59	0.72	0.80	0.61	0.76	0.83
dry	0.22	0.44	0.57	0.24	0.44	0.68

about 0.45 (dry) and 0.75 (wet) for C100_056k experiments. Closely related to the sensible heat fluxes, surface temperatures are on average 5 K smaller as for weakly forced cases. The reduced absolute difference in sensible heat fluxes between wet and dry patches as compared to weakly forced cases results in smaller differences in surface temperatures between the different tiles of about 1.5 K to 2 K as well as the smaller discrepancy between the sets of experiments (Fig. 3.8(b)). The reduced patch differences for larger tile sizes (e.g., 140 km) described for the weakly forced cases still holds for synoptically moderately forced conditions.

This section reviewed the impact of heterogeneous initial soil moisture perturbations on the surface heat budget. Interestingly, surface heat fluxes strongly alter with the synoptic regime and initial soil moisture bias. Patch differences are more prominent for tile sizes below 112 km whereas differences decrease above. Likewise, differences between the sets of experiments characterized by the bias are also consistent for patch sizes below 112 km and decrease above. Besides the striking dependence on the synoptic regime and initial soil moisture bias, findings suggest that the heterogeneity length-scale also has an influence surface heat budget.

3.2.2. Influence on the dynamical and thermodynamic structure

The previous section, we describe the influence of soil moisture heterogeneity on the surface heat budget, implying scale-dependent influence on surface temperature. This section elaborates on the question of how changes in surface heat budget induced by soil moisture heterogeneities influence the thermodynamic preconditioning and dynamic structure of the lower troposphere.

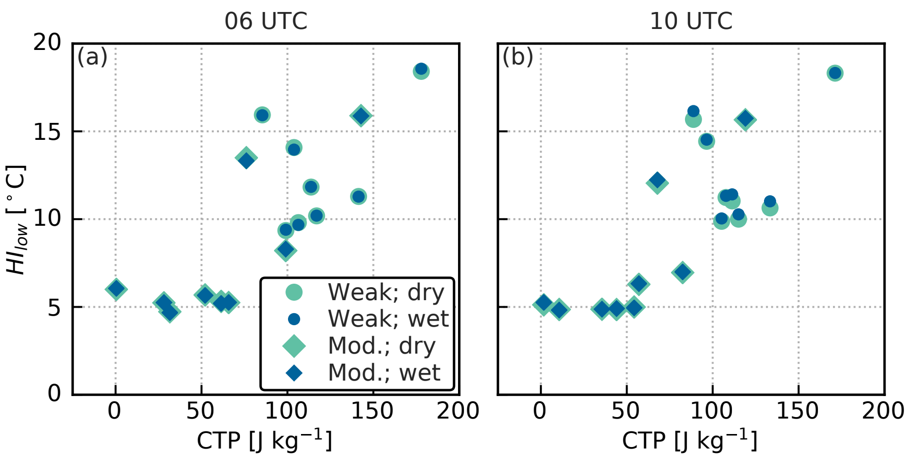

Figure 3.10.: Early morning (06 UTC, a) and morning (10 UTC, b) thermodynamic preconditioning plotting Convective Triggering Potential (CTP) against low-level humidity index (HI_{low}) (similar to Fig. 2.4) exemplary evaluated for C100_056k. Values are averaged over all wet (blue) and dry (green) patches and depicted for all weakly (circles) and moderately (diamonds) forced case studies.

The CTP–HI_{low} framework described in Section 2.8 evaluates the preconditions according to which convection is favored over dry or wet soil conditions, or whether convection is generally unlikely or probable to happen over any soil conditions. Findell and Eltahir (2003a) proposed to quantify the early-morning deviation from the lapse rate in a region which is likely to be incorporated in the BL during the day and the humidity content near the surface. Figure 3.10a shows the average CTP and HI_{low} computed over all wet and dry patches for all C100_056k experiments at 06 UTC in the morning. Most of the moderately forced cases appear in the lower left corner showing high low-level humidity and small CTP whereas some reveal dry low-level conditions and high CTP. Thus, values for moderately forced cases cover a vast region in this diagram. By contrast, all weakly forced cases cluster in the upper right corner showing higher moisture deficit and CTP. Interestingly, the difference between wet and dry patches is for all case studies small. While CTP hardly shows any difference, changes in HI_{low} are below 1 °C. Thus, the early-morning preconditioning determining the preferred soil state for convection initiation does on average not change between the wet and dry patches. This is similar for other patch sizes (not shown). Even though differences in HI_{low} slightly increase for weakly forced case studies until the beginning of convection triggering phase starting at about 10 UTC, they remain small (Fig. 3.10b). While average HI_{low} of wet and dry patches slightly drift apart for weak synoptic forcing, differences are vanishingly small for moderate forcing. This hints on convection triggering being more indifferent of the soil conditions for moderate forcing as for weak forcing. However, those difference evolving before 10 UTC are so small that they could not explain potential differences in convective precipitation.

As the CTP–HI_{low} framework does not reveal a fundamental change in preferred surface condition for convection triggering, the following paragraphs evaluate the impact of differentially heated surfaces and differences in evaporation on the dynamics in the troposphere below 7 km during the day. The distribution of thermodynamic energy can be described by the S_e

$$S_e = c_p T + L_v q_v + gz \tag{3.1}$$

which is the sum of the dry static energy ($c_p T$) and the latent energy ($L_v q_v$). It is calculated using the specific heat of air $c_p = 1005\,\mathrm{Jkg^{-1}K^{-1}}$, the latent heat of vaporization $L_v = 2.6\ 10^6\mathrm{Jkg^{-1}}$, the temperature T, the specific humidity q_v, the gravitational constant g and the altitude z. Convective available potential energy (CAPE) closely correlates with the S_e near the surface (Froidevaux et al., 2014). The differences in the vertical distribution of S_e and its components is computed between wet and dry patches:

$$\Delta S_e = c_p \Delta T + L_v \Delta q_v = c_p(T_{wet} - T_{dry}) + L_v(q_{v,wet} - q_{v,dry}) \tag{3.2}$$

Despite lower temperatures above wet patches, increased evaporation leads to an increase in moisture and a surplus of S_e below average BL height ($\approx$1200 m) over wet patches (Fig. 3.11). The portion of S_e driven by latent energy is higher for the smaller patch size in Figure 3.11a as compared to Figure 3.11b. The sign of ΔS_e

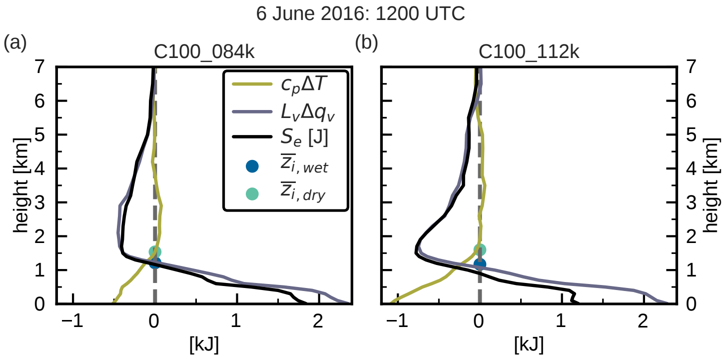

Figure 3.11.: Vertical distribution of horizontally averaged difference in Moist Static Energy (ΔS_e), specific humidity ($L_v \Delta q_v$) and temperature ($c_p \Delta T$) between wet and dry patches (wet - dry, see Eqn. 3.2) for C100_084k (a) and C100_112k (b). Additionally, the average BL heights over wet ($\overline{z_i}_{,moist}$, blue circle) and dry patches ($\overline{z_i}_{,dry}$, green circle) are indicated.

above the average BL height is reversed as air is drier over wet patches and vice versa. Again, the difference in S_e is mostly driven by the moisture content of the air, whereas the temperature differences ($c_p \Delta T$) are small. The vertical structure of S_e is similar to the one found in Froidevaux et al. (2014).

This vertical distribution of S_e can be explained by the influence of the soil moisture heterogeneity on dynamical processes in the lowest 4 km of the troposphere. The introduced soil moisture heterogeneity is expected to induce compensating thermally induced circulations near the borders of the patches as a result of differential surface heating. We created mean vertical cross-sections centered over wet patches to illustrate those circulation cells. An averaging box centered over wet patches including half of the dry patches on the east and west side (see the yellow box in Figure 2.2(f)) was shifted through the entire domain to get a large dataset for the averaging. The mean cross-sections shown in Figure 3.12 are constructed by meridionally averaging the vertical distribution of different quantities and taking the difference between the C100_084k (C100_112k) experiment and the control experiment UNI on 6 June 2016 at 12 UTC. Both snapshots show subsidence over wet patches (in the center of Figure 3.12) and upward motion over adjacent dry patches. Due to mass continuity, this results in near-surface divergence and weak upper-level convergence over the wet patches. Consequently, compensating circulations develop at the interfaces of wet and dry patches. The vertically averaged horizontal Moisture Flux Convergence ($\overline{MFC}$; $MFC = -u\frac{\partial q}{\partial x} - v\frac{\partial q}{\partial y} - q\left(\frac{\partial u}{\partial x} + \frac{\partial v}{\partial y}\right)$) shows strong low-level divergence (below 1 km height above ground) over the wet patches and a weak convergence aloft (between 1 − 2 km height above ground) (see Fig. 3.12b,e). This circulation determines the distribution of S_e (Eqn. 3.1) below 4 km. Over wet patches, increased evaporation leads to an excess of S_e of more than 400 J in the BL. Aloft, subsidence leads to drying and a deficit of S_e. This sequence is inverted over dry patches, whereas the near-surface surplus region is deeper and the vertical gradient above is weaker as compared to wet patches.

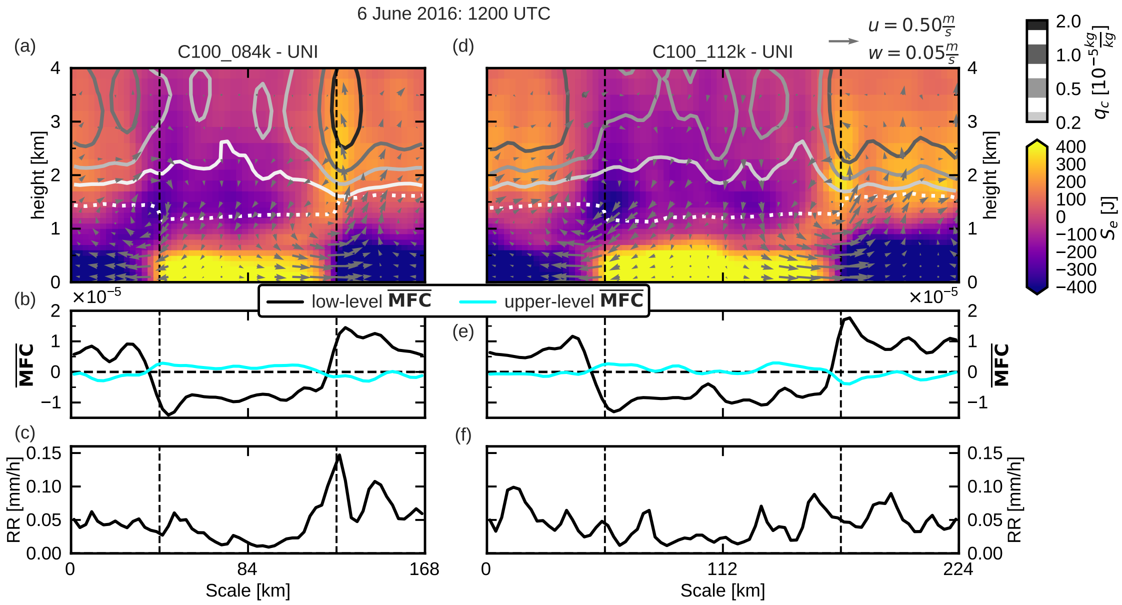

Figure 3.12.: Mean meridionally averaged vertical cross-sections with the wet patch in the center and half of the adjacent dry patches (according to the zonally shifted yellow box in Figure 2.2(f)) displaying the difference of Moist Static Energy (S_e) between the control simulation (UNI) and the C100_084k (a) and C100_112k (d) experiment evaluated on 6 June 2016 at 12 UTC. Yellow colors show an excess and purple colors a deficit in S_e compared to UNI. The arrows show the differences in the u and $10w$ components of the wind. The white dotted line indicates the average BL height. The contour lines indicate specific cloud water content (q_c). Panels (b) and (e) show vertically averaged difference in Moisture Flux Convergence below 1000 m above ground (low-level $\overline{MFC}$) and between 1000 m and 2000 m (upper-level $\overline{MFC}$). The average hourly precipitation (RR) is depicted in panels (c) and (f). Note that the background wind was easterly on 6 June. The dashed vertical lines in all panels indicate the borders between the patches.

The background wind plays a crucial role in the redistribution of S_e. In the example shown in Figure 3.12 the domain-averaged wind at 850 hPa is from easterly directions. Superposed with the convergent motion over dry patches, this leads to increased convergence near the downstream flank of the dry patch and increased divergence near its upstream flank as shown by the local extrema at the interface of wet and dry patches (Fig. 3.12a,b,d,e). There is a narrow updraft collocated with the region of increased low-level convergence. This updraft exports energy by lifting humid BL air with high S_e. This pattern is similar at both patch sizes but more intense at the smaller patch size (C100_084k) shown in Figure 3.12a. The narrow updraft region is indicated by the wind arrows, the region of higher S_e and the higher specific cloud water content. This amplified updraft leads to a peak in hourly precipitation in this region, as shown in Figure 3.12c. The spatial locking of precipitation maxima to soil moisture gradients is less evident at larger patch sizes (C100_112k, Fig. 3.12f) due to scattered, freely developing small updraft regions across wet patches. The interaction between the background wind and the soil

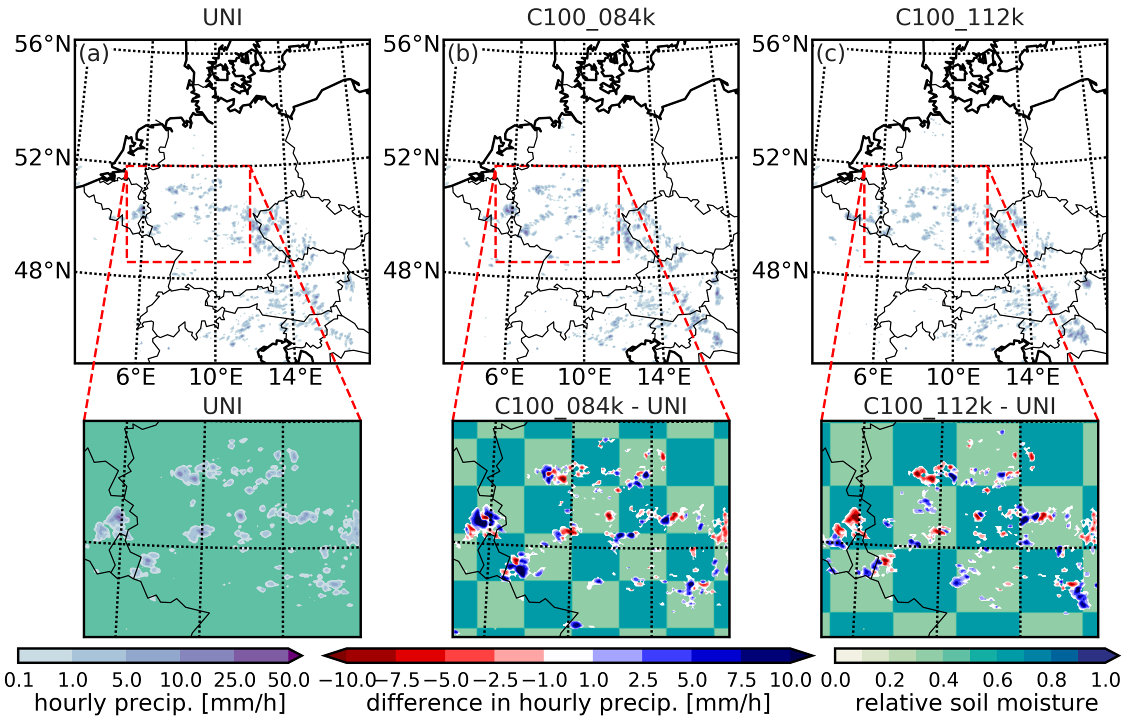

Figure 3.13.: Spatial distributions of hourly precipitation on 6 June 2016 evaluated at 12 UTC for UNI (a), C100_084k (b) and C100_112k (c) experiments. The zoomed insets show the hourly precipitation (a) and difference in hourly precipitation (b, c) for the Central German and border regions to Belgium, Luxembourg and France. Additionally, the initial relative soil moisture is shown for the zoomed region.

moisture heterogeneity influencing the dynamics in the lower troposphere seems to be less distinct at a horizontal scale of around 100 km.

Figure 3.13 depicts the spatial distribution of hourly precipitation corresponding to the experiments shown in Figure 3.12 revealing that the general regions covered by precipitation are similar and that the perturbations do not induce additional precipitating clusters. Precipitation mainly spreads over the Central German region including the border regions to Belgium and Luxembourg in the west as well as the Czech Republic and Austria towards the east. Zooming into that region and overlay the precipitation difference between UNI and each experiment in Figures 3.13b,c with the initial soil moisture supports the interactions between soil moisture and convection as described based on Figure 3.12. Both experiments predominantly show reddish colors over wet patches standing for a reduction of precipitation compared to UNI. In contrast to that, dry patches and preferably eastern and northern flanks of dry patches often show an increase in precipitation (blueish colors). Those features are discernible for both experiments, although more prominent for the smaller patch size experiment (C100_084k, Fig. 3.13b) as compared to the larger patches (C100_112k, Fig. 3.13c). Precipitation is concentrated near the windward flanks of the dry patches whereas for the smaller patch sizes precipitation is more evenly distributed over flank regions and dry patches for the larger patch size. The

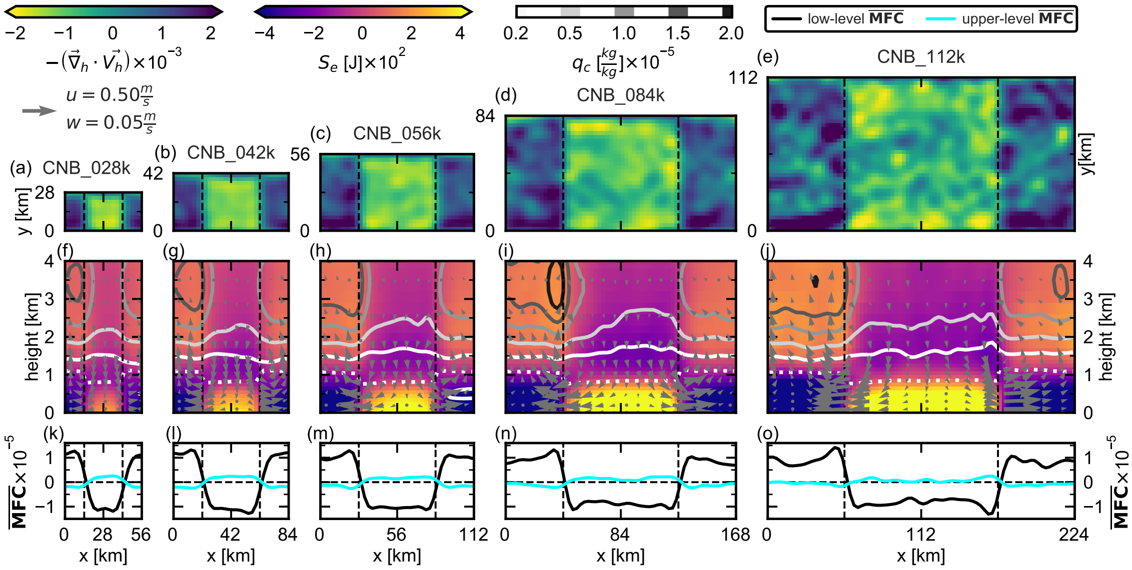

Figure 3.14.: Mean horizontal convergence (averaged below 1 km height above ground; a-e) and vertical cross-sections (f-j) of S_e, wind and cloud condensates (as in Fig. 3.12) for different patch lengths and averaged over all eight weakly forced case studies valid at 12 UTC. The white dotted lines indicate the average BL height. Panels (k-o) depict the vertically averaged moisture flux convergence (below 1000 m above ground (low-level $\overline{MFC}$) and between 1000 m and 2000 m (upper-level $\overline{MFC}$)) averaged over all experiments. Note that the data of the eight weakly forced case studies are rotated so that the mean wind in 850 hPa at 12 UTC is always westerly (coming from the left).

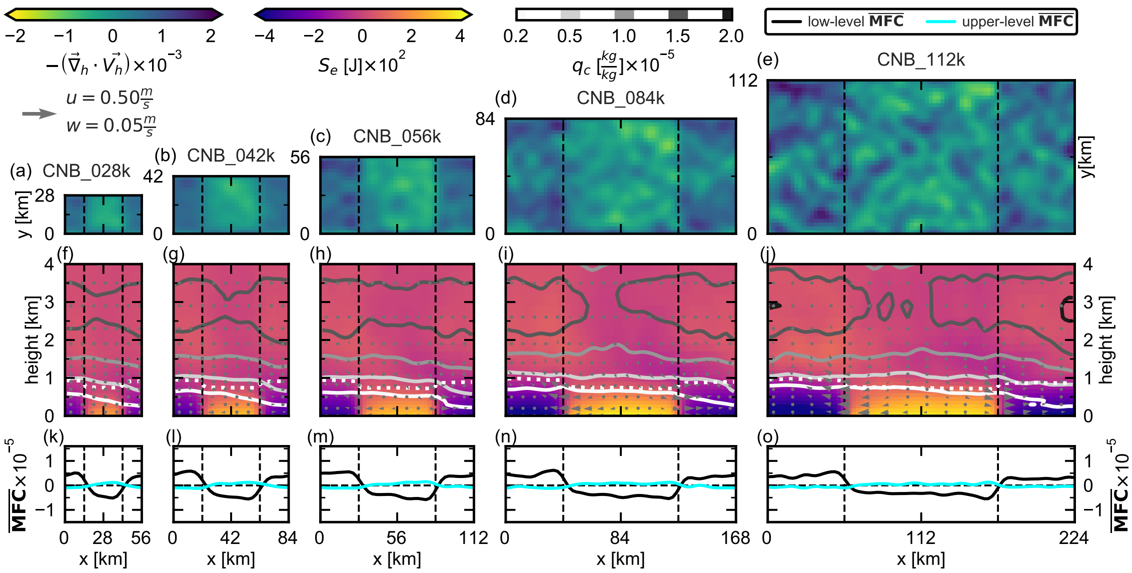

Figure 3.15.: As Figure 3.14, but averaged over all nine synoptically moderately forced case studies listed in Table 2.2.

stronger determination of precipitation differences by soil moisture heterogeneity for the smaller patch size again hints on a scale-dependent interaction between the background wind and soil moisture perturbations influencing the dynamics in the lower troposphere.

To test this hypothesis, the same diagnostics as for Figure 3.12 are applied to all eight weakly forced cases and chessboard experiments (Fig. 3.14). The pattern of the vertical velocity with predominantly ascending motion over dry patches and descending motion over wet patches, as well as the characteristic distribution of S_e and Moisture Flux Convergence (MFC) (Fig. 3.14f-o) confirm previous findings and show a clear but scale-dependent dipole structure. The structure is less pronounced for smaller patch sizes (C100_028k, C100_042k). For the medium size experiments (C100_056k, C100_084k), a clear convergence and updraft region are present near the downstream flank of the dry patch collocated with a region of increased values of liquid cloud condensates. This preferred scale is similar to findings from the single case study discussed in Figure 3.12a. Additionally to the horizontal structure of the multi-day mean S_e, vertically averaged (over the lowest 1 km height above ground) horizontal convergence is depicted in Figure 3.14a-e (note this is no difference plot). There is predominantly divergent motion over the central wet patches and convergence over adjacent dry patches. However, this structure is increasingly blurred and broken up for C100_112k by individual convergence zones within the wet patch (Fig. 3.14e). These numerous small updraft regions within the wet patch lead to the more variable distribution of precipitation, as discussed earlier (see Fig. 3.12f).

Application of the same diagnostics on the moderately forced cases reveals a similar structure of S_e in the BL but a rapid weakening further aloft (Fig. 3.15). Furthermore, differences in average BL height between the patches are visible, but differences are less pronounced as under weakly forced conditions. This can be traced back to the less distinct strength of the circulation cells (Fig. 3.15f-j). The magnitude of low-level MFC for moderately forced cases is about half of that of the weakly forced cases, and the differences between wet and dry patches are smaller for all patch sizes (Fig. 3.15k-o). The background wind mainly influences the low-level MFC insofar as divergence is decreased at the upstream gradient but increased near the downstream gradient. Horizontal cross-sections of mass flux convergence show weaker convergence over dry and divergence over wet patches during moderate synoptic forcing (Fig. 3.15a-e). At the largest patch size, there is hardly any difference discernible between dry and wet patches.

In summary, spatial anomalies in soil moisture strongly influence the energy distribution in the troposphere (up to a height of 7 km). Thermally induced circulation cells play a crucial role in redistributing S_e gradients emerging from differentially heated surfaces. Dependent on the synoptic control, this largely influences the dynamics in the lowest few kilometers. A superposition of those circulation cells with the background wind leads to persistent updraft regions at the downstream side of dry anomalies during weakly forced weather conditions. These updraft regions are preferred locations of deep convection and are most distinct for heterogeneity length scales between 40 km and 80 km.

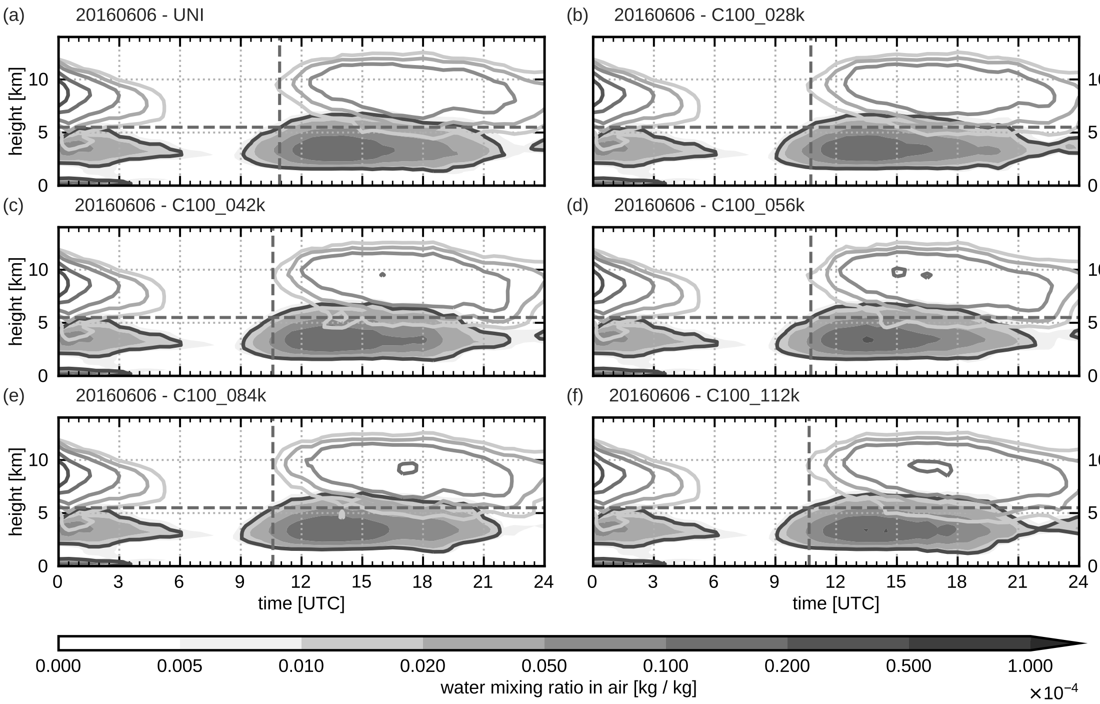

Figure 3.16.: Time series of vertical distribution of liquid (shaded) and ice (gray contours) water mixing ratio horizontally averaged over the German subdomain. The horizontal black dashed line indicates an altitude of 5.5 km, whereas the vertical dashed black line marks the transition time from shallow to deep convection. Evaluation is shown for the control experiment (UNI) (a), as well as experiments C100_028k (b), C100_042k (c), C100_056k (d), C100_084k (e) and C100_112k (f) on 06 June 2016.

3.2.3. Influence on clouds

To examine how those dynamical mechanisms affect cloud formation, we focus the investigation on the no-bias experiments (C100) with patch sizes ranging from 28 km to 112 km. We start with the influence of soil moisture perturbations on the vertical cloud structure. Figure 3.16 exemplarily shows the time series of the domain-averaged vertical distribution of liquid cloud water and ice condensates in the UNI and C100 experiments for the 6 June 2016 weakly forced case. At first glance, the vertical distribution of the cloud quantities only shows negligible differences with a slightly longer presence of high ratios of cloud condensates in experiments with large patches. Using MFASIS (a Method for FAst Satellite Image Simulation Scheck et al., 2016), we produce synthetic visible satellite images from the model output. Visually inspecting snapshots of three consecutive time steps of UNI (Fig. 3.17a-c) and C100_084k Fig. 3.17d-f) reveals that white areas are growing faster for the heterogeneous experiment especially throughout the first two hours. To quantify this faster growth, we introduce transition time from shallow to deep convection. Similar to Rieck et al. (2014), we define the transition time as the first time between 6 and 12 UTC when the ratio of liquid cloud condensates exceeds a value of $10^{-6}\,\mathrm{kg\,kg^{-1}}$ at an altitude of 5.5 km. Comparing the transition time between

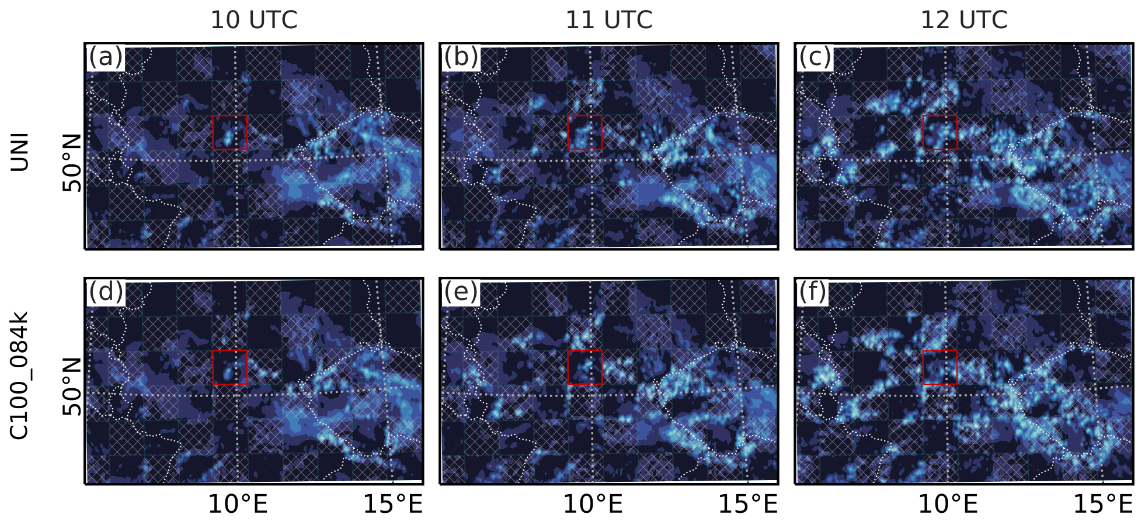

Figure 3.17.: Synthetic visible satellite imaged produced by MFASIS for three consecutive hours (11, 12, 13 UTC) on 6 June 2016 focusing on Central Germany. UNI experiments are depicted in the first (a-c) and C100_084k in the lower row (d-f). Initial soil moisture field for C100_084k is shown in the background all graphics (dry patches are hatched).

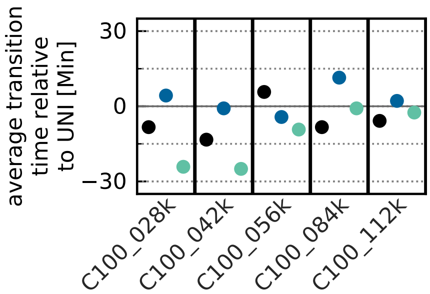

Figure 3.18.: Average transition time from shallow to deep convection relative to the control simulations evaluated for all experiments across all patches on five weakly forced case studies (black). For the chessboard experiments the transition time is separately shown for wet patches (blue) and dry patches (green).

the control simulation and the different patch sizes reveals an earlier transition of approximately half an hour over heterogeneous soil conditions (Fig. 3.16a vs. b-f). The earlier transition time from shallow to deep convection and the slightly longer lifetime of clouds in the heterogeneous soil moisture experiments comprise the most important differences when inspecting the time series of the vertical distribution of cloud quantities.

Applying this diagnostic on data with 5-min output frequency for six weakly forced cases shows an approximately 15 min earlier transition time from shallow to deep convection over heterogeneous surface conditions (black circles in Figure 3.18). The transition starts over dry patches (additionally 15 min earlier) and is followed half an hour later over wet patches. The time lag of the transition from shallow to deep convection between dry and wet patches amounts to merely 30 min in the cloud signal. There is a small yet systematic scale-dependent difference in the transition

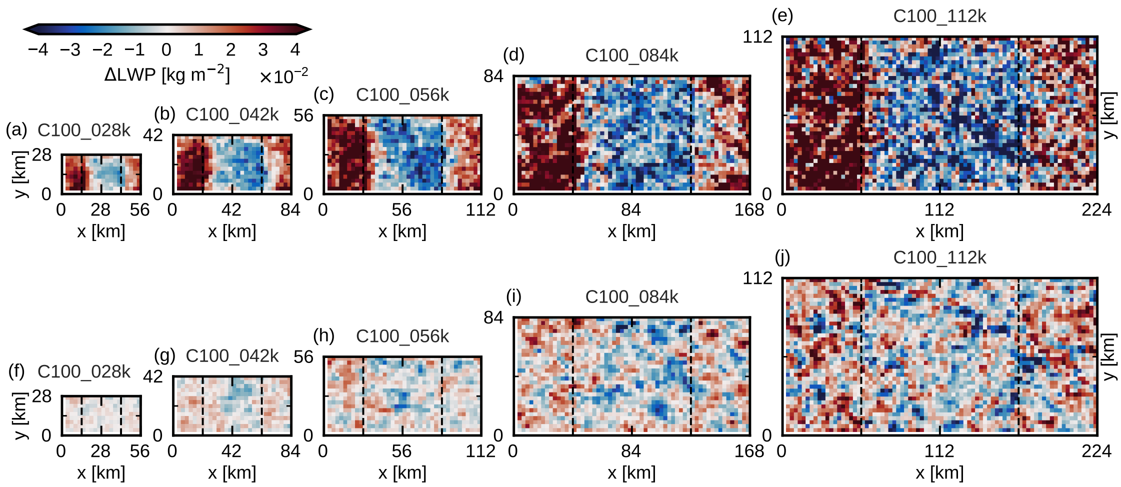

Figure 3.19.: Mean meridionally averaged horizontal cross-sections displaying the difference in LWP between the control simulation (UNI) and C100_028k (a,f), C100_042k (b,g), C100_056k (c,h), C100_084k (d,i) and C100_112k (e,j) experiment at 12 UTC with the wet patch in the center and half of the adjacent dry patches (according to the zonally shifted yellow box in Fig. 2.2(f)). Evaluations are shown averaged over all weakly (a-f) and moderately (f-j) forced case studies. Red colors show an excess and blue colors a deficit in LWP compared to UNI. Dashed vertical lines in all panels indicate the borders between the patches. Note that data are rotated so that the mean wind in 850 hPa is always westerly (left side in graphic).

time with the earliest appearance at 42 km patch size and continuously later times at larger scales eventually approaching the uniform experiment UNI. Note that the 4 and 5 June, as well as the moderately forced case studies, are excluded in this analysis since those were cloudy throughout the day resulting in transition times not representative for summertime afternoon convection. Extensive cloud coverage lasting the entire day is also the reason why this method is not applicable for synoptically moderately forced situations.

The average effect of different transition times over dry and wet patches is visualized by computing an advanced mean horizontal cross-section of the difference in Liquid Water Path (LWP) between the C100_* experiments and the control simulation UNI (Δ LWP) (Fig. 3.19). Those mean horizontal cross-sections are similarly constructed as those in Figures 3.12, 3.14, or 3.15 and thus are centered over wet patches and include half of the neighboring dry patches. For weakly forced cases, the transition is not only earlier but is also more efficient over dry tiles. For all patch sizes, the central patch (i.e. wet) reveals blueish colors pointing on a deficit on LWP whereas the reddish colors over the dry parts hint on an excess. Two main features are additionally discernible. The difference between patches is becoming less pronounced since the pattern gets slightly noisier with increasing patch size. This is especially true for C100_112k in Figure 3.19e. It also clearly correlates with the decreasing differences in transition time with increasing patch sizes shown in Figure 3.18. Additionally, the left dry part shows darker red colors as the whereas colors are lighter on the other side. Note that all data are rotated such that the mean wind in 850 hPa is coming from the left side in the graphic. Thus, the unequal response of LWP depending on the location relative to the prevailing wind conditions implies that the mid-tropospheric wind has an important impact on the soil-atmosphere interaction.

In contrast to that, moderate synoptic forcing lead to the weaker influence of heterogeneous soil moisture conditions in C100_* experiments (Fig. 3.19f-j). There is some influence for mid-size patches between 42 km and 84 km discernible, but the pattern is very noisy. Even though the chessboard patterns do not show a major local impact, mainly reddish colors point on soil moisture heterogeneity having an amplifying effect on general LWP.

Summarizing, the wet patches have a suppressive influence on LWP, while LWP is increased over dry patches. Synthetic satellite images produced based on UNI and C100_084k simulations for 6 June 2016 (Fig. 3.17) support this effect. The single convective cell that appears in the red box of Figure 3.17a is continuously growing throughout time in the UNI simulation. However, this cell is partly suppressed in C100_084k simulation (Fig. 3.17d). It still grows in this scenario but remains far below its original intensity in UNI. Besides that, cloud amount and intensity are increased for the dry patches in C100_084k. This is most pronounced at 11 UTC (Fig. 3.17e) and 12 UTC (Fig. 3.17f). This influence of dry patches in cloud formation leads, in the case of weak synoptic forcing to an earlier transition from shallow to deep convection of merely 30 min. Whether the spatial influence of soil moisture heterogeneity and the earlier transition time affects convective precipitation is discussed in the following subsection.

3.2.4. Influence on precipitation

This subsection collects the findings of the previous sections to discuss the combined impact of soil moisture bias and heterogeneity introduced by chessboard patterns with varying tile sizes on precipitation. Time series of the domain-averaged accumulated precipitation relative to the control simulation averaged over eight weakly forced cases and all experiments are shown in Figure 3.20a for each set of experiments (C075, C100, C125). The no-bias experiments (C100) show a similar amount of domain-averaged 24 h accumulated precipitation as the control run (UNI). Thus, the introduced soil moisture heterogeneity does, on average, not alter the domain-averaged precipitation amount. Noticeable variability in precipitation is discernible from 15 UTC onwards. The moist-bias experiments (C125) show the highest precipitation rates in the afternoon leading to an increase in daily precipitation of about 10 %. The opposite holds for the heterogeneous dry-bias experiments (C075). Those experiments produce, on average, about 15 % less precipitation than the control simulation. Different amounts of precipitation changes for C075 and C125 show that the magnitude of the soil moisture perturbations relates nonlinearly to the surface

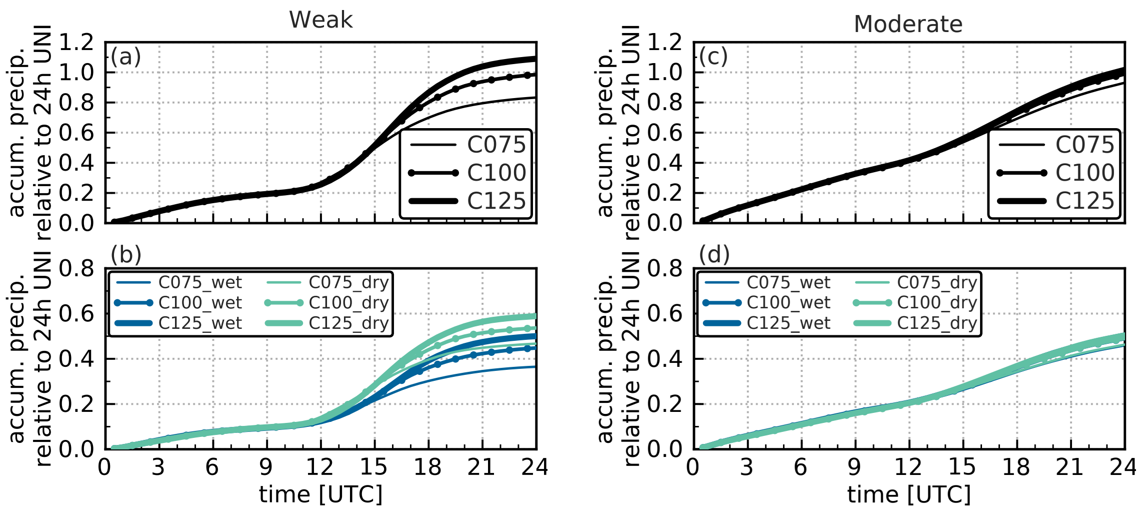

Figure 3.20.: (a) Time series of the domain-averaged accumulated precipitation relative to the domain-averaged 24 h accumulated precipitation of the control simulation (UNI) evaluated for the German subdomain averaged for eight weakly forced cases. All heterogeneity length scales are incorporated in each set of experiments. (b) Same as (a) but evaluated for dry (green) and wet (blue) patches separately. Panels (c) and (d) are the same as (a) and (b) but evaluated for nine moderately forced case studies. Note that the local noon is shortly after 13 UTC.

fluxes (as elaborated in Section 3.2.1) which in turn relates nonlinearly to the precipitation. Relative differences shown in Figure 3.20 well coincide with findings shown for the bias simulations (see Figure 3.4 in Section 3.1).

However, distinguishing the domain-averaged precipitation between wet and dry patches reveals two noticeable differences (Fig. 3.20b). The rate of afternoon precipitation is higher over dry patches than over wet patches from about 11:30 UTC onwards. This increase is mainly generated by the earlier increase in precipitation rate over dry patches which occurs about 3 h before the increase over wet patches (11:30 versus 14:30 UTC) which is based on an earlier transition from shallow to deep convection as described in Section 3.2.3. While the time lag of the transition from shallow to deep convection between dry and wet patches amounts to merely 30 min in the cloud signal, the steepest increase in precipitation rates is lagged by 3 h across the different patches. As a result, separately considering wet and dry patches shows more precipitation over dry patches than over wet patches.

To address the scale-dependent impact of the SMP coupling, we focus on the day-to-day variability of accumulated daily precipitation. The patch size dependent, daily precipitation of C100 averaged over all seven cases hardly exhibits any difference to the control experiment UNI (black dots in Figure 3.21a). Likewise, the positive SMP coupling on the overall soil moisture bias is evident as the mean daily precipitation of C125 (C075) is again about 10 % (15 %) higher (lower), respectively. In contrast, the day-to-day variability, depicted by the shading in Figure 3.21a indicates a scale-dependence. The experiments with soil moisture perturbations at 56 km and 84 km patch size show a decreased day-to-day variability. The day-to-

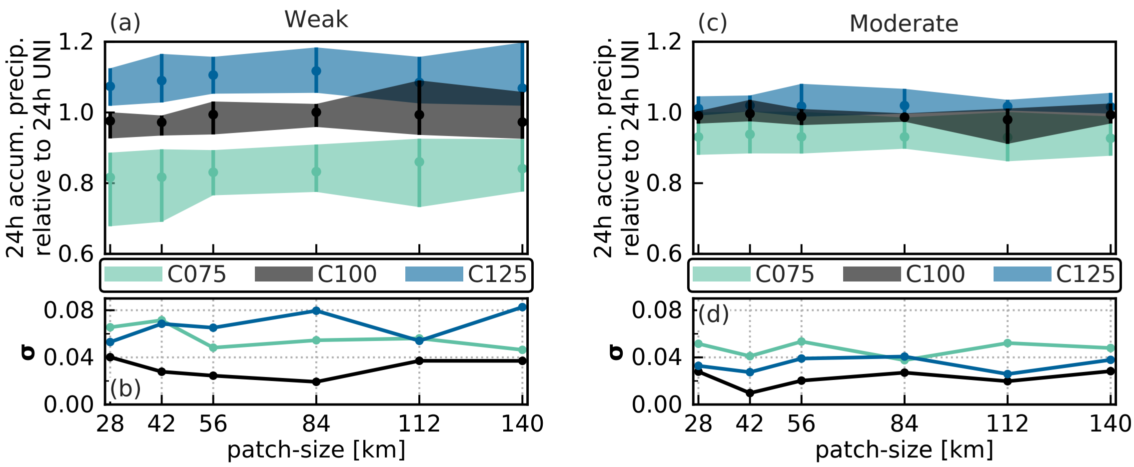

Figure 3.21.: (a) Mean (dots) and range (shaded area) of daily accumulated precipitation of the eight weakly forced case studies relative to the control simulation (UNI) as a function of patch size averaged over the German subdomain. (b) Patch-size dependent standard deviation (σ) of precipitation accumulated between 9 h and 18 h for seven weakly forced case studies evaluated for C100 experiments. Panels (c) and (d) are the same as (a) and (b) but evaluated for nine moderately forced case studies.

day standard deviation of precipitation accumulated between 9 h and 18 h – the period of heaviest convective precipitation – indicates that C100 experiments with soil moisture perturbations between 42 km and 84 km patch size show the smallest day-to-day variability (Fig. 3.21b). This coincides with the scale range at which dynamical effects described in Section 3.2.2 are most prominent. According to that, subsidence over wet patches hampers and convergence over dry patches, especially in the vicinity of thermally induced circulation cells near the sharp soil moisture gradients, foster convection initiation. The gentle mid-tropospheric background wind even amplifies those circulation cells. The superposition of bias and heterogeneity effects lead to the increased day-to-day standard deviation for C075 and C125 experiments and vanished scale dependence.

As the SMP coupling is expected to depend on the synoptic control, we also applied the diagnostics on four moderately forced case studies. The time series of accumulated precipitation in Figure 3.20c,d as well as the accumulated precipitation in Figure 3.21c only show minimal differences compared to the control simulation. There is only a small decrease of about 5 % in precipitation of C075 experiments. Furthermore, the day-to-day variability also reveals smaller values (Fig. 3.21d) for each set of experiments. This is in line with results from previous sections reporting that the surface energy budget, as well as thermodynamic and dynamic modifications, are less prominent during moderate synoptic control. Strong mid-tropospheric winds, as well as generally reduced surface heat fluxes, hamper the interaction between soil and atmosphere. Hence, the atmosphere's response to soil moisture perturbations is feeble for moderately forced case studies.

In summary, the *overall* soil moisture bias shows a positive SMP coupling, whereas *locally* there is a negative coupling resulting in more precipitation over drier soils.

Secondly, local soil moisture perturbations with scales between 40 km and 80 km lead to a lower day-to-day variability of area-averaged accumulated precipitation.

3.2.5. Discussion and summary

In the present section, we examined the scale- and case-dependent influence of soil moisture perturbations on the triggering of deep convection and the subsequent convective precipitation based on convection-permitting simulations of eleven real case scenarios over Central Europe using the COSMO model. We replaced the initial soil moisture by chessboard patterns with different patch sizes ranging from about 30 km to 140 km and superposed by a soil moisture bias of ±25 %. This methodology has been motivated by recent findings exploiting a multi-year dataset of satellite observations (Guillod et al., 2015; Taylor, 2015) and idealized convection-permitting modelling studies (Froidevaux et al., 2014).

Based on over 300 COSMO-DE experiments for real case scenarios, we conclude:

- Evaluating the evaporative fraction (Figures 3.7 and 3.9 as well as Table 3.1) we find values of approximately 0.75 (0.45) for wet (dry) patches in our C100_056k experiments. This difference is in good accordance with the observed contrast between grassland and cropland obtained based on turbulence and energy flux measurements (Zhang et al., 2017). It is also in line with with the perturbation setup used in idealized LES performed by Lee et al. (2019). They constructed their dry (wet) chessboard patterns by subtracting 30 % from the latent (sensible) and adding this portion to its counterpart. This good agreement further strengthens the relevance of our initial soil moisture perturbations not only representing the mean deviation between COSMO model and observations but also resembling a naturally relevant gradient.

- Soil moisture bias and soil moisture heterogeneities affect the precipitation forecast in different ways. Firstly, there is a positive SMP coupling concerning the soil moisture bias. Perturbations of the initial soil moisture by ±25 % dominate the overall effect and result in differences in daily domain averaged precipitation of ±10 −15 % compared to the control simulation. Those values compare well to the findings described in Section 3.1 for the simple bias simulations (B075, B125). While the domain-averaged impact is slightly larger for the heterogeneous bias simulations evaluated in this section, the magnitude, sign, and nonlinearity are very similar to the homogeneous bias experiments for both synoptic forcings. In contrast, we find a local negative SMP coupling with respect to soil moisture heterogeneity. Differential heating over dry and wet soil patches generates circulation cells at the patches' boundaries accompanied with convergence over dry and divergence over wet patches within the BL, respectively. Convergence over dry areas leads to an earlier transition from shallow to deep convection [$\mathcal{O}$(30 min)] and hence preferred convection triggering and more precipitation. Spatial analysis of the Liquid Water Path (LWP) reveals generally higher values over dry patches. Furthermore, visually inspecting synthetic satellite images of three consecutive time steps during the initiation phase proved earlier and preferential triggering over dry patches, and suppression wet patches. This influence on the transition from shallow to deep convection agrees with Rieck et al. (2014), who also found earlier transition times over heterogeneous surfaces. Due to their higher model resolution and highly idealized domain setting the transition time occurs even earlier and the heterogeneity length scale with the most definite impact is slightly smaller as compared to our experiments using an operational weather forecasting model. According to experiments with high spatial resolution and horizontally homogeneous atmospheric initial conditions conducted by Cioni and Hohenegger (2017), the earlier triggering of convection over dry areas extend the duration of precipitation while soil moisture availability controls the area-averaged precipitation amount. As the latter effect is more dominant, the longer duration of precipitation across dry patches is not able to compensate for the smaller precipitation intensity and thus results in a positive domain-averaged SMP coupling. The different signs of SMP coupling described above show the importance of the analyzed scale for the sign of SMP coupling with a negative local and positive regional scale coupling.

- Vertical cross-sections point to the importance of the mean background wind in the lower troposphere. Superposition of the background wind with convergent motion over a dry patch within the BL enhances the low-level convergence downstream of the dry patch close to the adjacent wet patch. This dynamic mechanism leads to an intensification of the thermally induced vertical circulation. In conjunction with the reservoir of high S_e air above the wet patch, this results in preferred convective triggering and increased precipitation at the downstream side of the dry patch. This amplified circulation also coincides with the region of the highest surplus in LWP. In contrast, the same mechanism decreases low-level moisture flux convergence at the upstream side of the dry patch. Thus, the interplay of soil moisture gradients with the background wind represents an important mechanism that causes an earlier transition from shallow to deep convection over heterogeneous soil conditions and an earlier increase in convective afternoon precipitation over dry patches. This result is in agreement with findings of Froidevaux et al. (2014), and Lee et al. (2019) using horizontally homogeneous atmospheric initial conditions. Rochetin et al. (2016) conducted LES of a 50 km wide anomaly in surface sensible heat flux integrated in an idealized domain with horizontally homogeneous atmospheric initial conditions. Investigating the interaction with convection triggering, their simulations also reveal an asymmetry in thermally induced circulations induced by interaction with the mid-tropospheric background wind determining the location of convection initiation. Furthermore, our results support the observational analysis of Taylor (2015).

- There is a scale-dependent influence of soil moisture perturbations on the effectiveness of triggering deep convection and the amount of subsequent convective precipitation. The smallest day-to-day variability in accumulated precipitation computed over eight different real cases emerges for patch sizes between 42 and 84 km. Similarly, the earliest transition from shallow to deep convection occurs in

this scale range. During synoptically weakly forced situations, the average residence time of an air parcel traveling across an individual patch of 56 km amounts to roughly 3 h given a typical background wind of about $5\,\mathrm{ms}^{-1}$. This residence time, in conjunction with the vertical circulation forced at the soil moisture interfaces, allows for fully developed thermally induced circulation cells consistently affecting the patches at these spatial scales. Towards smaller patch sizes (28 /42 km corresponding to 10/15 grid cells, respectively) the interaction of the thermally induced circulations cells and the background wind decreases. The circulation cells are too close to each other so that their influence is not individually discernible. Rieck et al. (2014) observed similar behavior in their simulations. They found a negligible impact of soil moisture heterogeneity for the smallest patch sizes [$\mathcal{O}(5\,\mathrm{km})$] as the thermally induced circulation cells collided too early and before the transition time from shallow to deep convection. On the other hand, the residence time of an air parcel traveling across the patch is too short to fully adapt to the thermodynamics over the individual patch. For patch sizes above 100 km, however, air parcels have fewer constraints (i.e. enough time and space) and can spontaneously rise within single patches resulting in a less structured precipitation distribution and, ultimately, in a larger day-to-day variability. The thermodynamical trigger mechanism resulting from the interplay of prescribed soil moisture gradients in the presence of a weak ambient wind is not as dominant as on scales between 40 km and 80 km.
A recent study applying chessboard shaped initial conditions in simulations with a horizontal resolution of about 20 m and horizontally homogeneous atmospheric initial conditions support the smallest resonant scale of 5 km (Lee et al., 2019). Since this hints on a strong influence of the model resolution on the preferential length scale of soil moisture perturbations, two of the real-case studies have been performed using the COSMO model at 500 m grid spacing in Appendix A. Results presented in the appendix hint on a shift of the range of resonant scales towards smaller patch sizes. However, due to the high computational costs of the finer grid-scale, only two days with two experiments were possible, which complicates conclusions. Furthermore, the assignment of the results to either the increased model resolution or the improved turbulence scheme applied to the high-resolution simulations is not possible. This means that it is not clear whether differences arise from an improved representation of dynamical processes due to the finer grid spacing or if the better turbulence scheme is more dominant.

- The interaction of soil moisture bias and soil moisture heterogeneities on precipitation is weather regime dependent and its influence decreasing with increasing synoptic forcing. Averaging over the moderately forced cases results in a precipitation difference of merely $\pm 5\,\%$ from the respective uniform control simulations that are about half the value as for weakly forced regimes. With increasing synoptic control, the mean tropospheric wind speed, low-level wind shear, and large-scale instability are generally increasing, and local triggering mechanisms due to soil moisture perturbations are less important. In high-resolution simulations initialized with heterogeneous surface conditions and varying vertically uniform horizontal wind speeds, Lee et al. (2019) found vanishing thermally induced circulation cells with increasing wind speed. Froidevaux et al. (2014) additionally reported a change in the sign of SMP coupling for increasing background wind from negative for vanishing winds to positive for strong winds. Furthermore, analysis of surface heat fluxes implies smaller influences of surface conditions for moderate synoptic forcing resulting from increased cloud amount negatively influencing surface heat fluxes. Those factors explain the reduced importance of soil moisture heterogeneity during moderate synoptic forcing. However, spatial analysis of LWP still reveals a small, overall positive influence of soil moisture heterogeneity during moderate synoptic forcing.

In summary, our numerical simulations confirm the observational findings of a positive temporal coupling (herein mimicked by soil moisture bias) and a negative spatial coupling (herein mimicked by soil moisture heterogeneity) as suggested by Guillod et al. (2015). Furthermore, the exploitation of the consistent model-based four-dimensional dataset allows for the inspection of the dynamical implications of the soil moisture gradients. The background wind establishes a region of persistent updraft at the downstream flank of dry patches exporting air with high S_e from the BL above the wet patch. Employing the COSMO model with a horizontal grid spacing of 2.8 km the vertically enhanced circulation cells have a dominant influence at scales between 40 km and 80 km leading to preferential triggering of convective precipitation near the downstream side of the dry patch. This mechanism optimally locks the triggering of convective precipitation near soil moisture gradients leading to spatial redistribution of precipitation with maxima at the soil moisture interfaces and to an overall reduction of the day-to-day variability of area-averaged precipitation.

Accounting for the uncertainty in triggering deep convection during weak synoptic control has been a long-standing issue in convection-permitting ensemble modeling. In convective-scale ensemble prediction systems this is presently accounted for by perturbing soil moisture values and patterns (Bouttier et al., 2016; Schraff et al., 2016). The results of our study suggest that the most important uncertainties for local precipitation forecasts are those with scales of 40–80 km, owing to the strong atmospheric response. The characterization of soil moisture errors on these scales and their representation in ensemble prediction systems will be an important focus for future research.

3.3. Relative influence of soil moisture perturbations on precipitation

As the previous sections showed, heterogeneous initial soil moisture perturbations can influence the intensity and location of precipitation by modifying the thermodynamic structure of the BL. By applying a general soil moisture bias or chessboard patterns, perturbations discussed so far are based on very idealistic approaches suitable for process-oriented studies. In order to test whether those processes can lead to relevant variability in a perturbed-parameter ensemble, heterogeneous soil moisture perturbations are generated using spatially filtered initial conditions in the following section to simulate different levels of spatial accuracy of soil moisture. The following section focuses on the relative contribution of three major sources of uncertainty in convection initiation and formation of precipitation (see RQ-3 in Section 1.4). Heterogeneous soil moisture perturbations are performed using spatially filtered initial conditions. Experiments initialized with High-, Low- and Band-pass filtered surface conditions introduce uncertainties in the lower boundary of the model by differential surface heating. Note that we use those nine spatially filtered initial soil moisture conditions to generate an ensemble of simulations with initial soil moisture perturbations. For doing that, we chose meaningful heterogeneity length-scales motivated by results in Section 3.2 and the length-scales used in KENDA. Thus, those are not used for further investigation of the scale-dependent SMP coupling, but for generating an ensemble based on meaningful initial soil moisture perturbations.

We will compare the impact of those soil moisture perturbations to two other major sources of uncertainty in convection initiation and formation of precipitation. They will be compared to the impact of uncertainties in the boundary layer introduced by stochastic boundary layer perturbations (PSP) and microphysical uncertainties realized by variations in CCN concentrations. Soil moisture perturbations modify the boundary layer via the surface heat budget, whereas the PSP scheme directly perturbs the structure of the BL. Perturbations of the aerosol concentration influences, on the one hand, the cloud formation. On the other hand, it affects the earth's surface radiation budget by cloud-radiation interactions and thus indirectly feeds back to the BL (e.g., Seifert et al., 2012; Fan et al., 2016). Performing separate COSMO experiments with a single type of perturbation allow the accountability of differences between the ensembles to each the three types of uncertainty. A white noise ensemble (WNoise) and the operational COSMO-DE-EPS provide a lower and upper benchmark for spatial and ensemble variability.

The following section concentrates on a HIW period in May/June 2016 and the German subregions (see Fig. 2.1). Note that we differentiate two types of averages by marking spatial averages with $\langle\cdot\rangle$ and ensemble averages with an overbar $\bar{\cdot}$.

The first part (Section 3.3.1) revisits the characteristics of the synoptic situation during the HIW period applying descriptive measures, like convective adjustment timescale (τ_c), precipitating fraction or low-level humidity index (HI_{low}). Ensemble variability of precipitation will be assessed in the second part (Section 3.3.2) applying normalized standard deviation while spatial variability will be evaluated in Section 3.3.3 using Fractions Skill Score (FSS). We will additionally evaluate ensemble and spatial variability with respect to regional and synoptic differences.

3.3.1. Synoptic classification of the high impact weather period 2016

During a 10-day high impact weather (HIW) period in May/ June 2016, Central Europe was daily affected by severe convection causing high financial losses. During that period, a persistent atmospheric blocking over Central Europe characterized

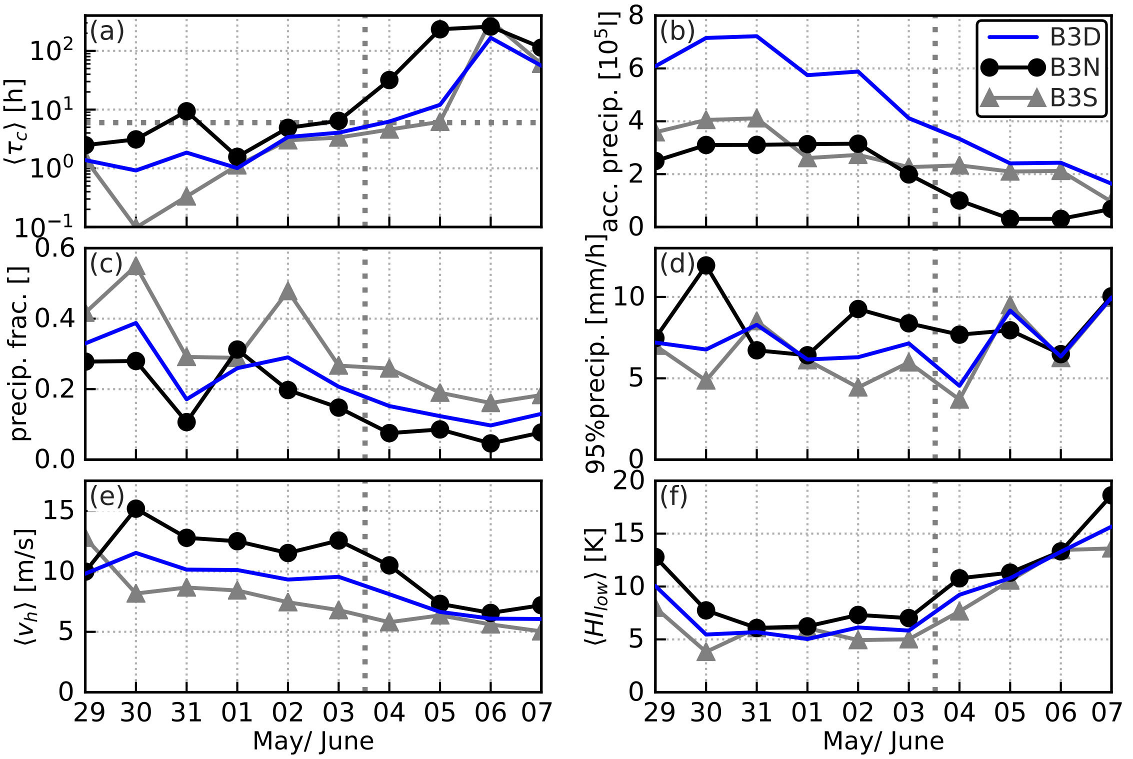

Figure 3.22.: Time series of area-averaged, daily maximum convective adjustment timescale ($\langle \tau_c \rangle$, a), domain accumulated daily precipitation (b), fractional coverage of precipitation (c), 95$^{\text{th}}$ percentile of precipitation amount (d), horizontal wind speed ($v_h = \sqrt{u^2 + v^2}$) at 500 hPa (e), and the low-level humidity index (HI_{low}) (f) for 10 days from 29 May to 7 June 2016. Evaluations were performed for the German subdomain (blue), as well as the northern (black with circles) and southern (gray with triangles) German subdomains using unperturbed reference simulations. The horizontal, gray, dotted line in a indicates the threshold value of 6 h used to classify weather regimes using the convective adjustment timescale (τ_c). Note that the dependent variables are given in logarithmic scale. The HIW episode is divided into a synoptically moderately forced regime (29 May to 3 June) and a weakly forced regime (4 to 7 June) optically separated by the vertical, gray, dotted line in each figure.

the synoptic situation. Two upper-level troughs built the blocking and were located between Iceland and the Azores in the west and from northern Scandinavia to the black sea flanked a high-pressure system ranging from Iceland to central Scandinavia. A weak pressure gradient over Central Europe dominated the scenery between the deviated flow over Northern Europe and the fairly zonal flow over the Mediterranean region. This weak pressure gradient leads to low thermal stability and low mid-tropospheric wind speed, providing a convection-favoring weather situation. In the first part of the period, however, a weak upper-level trough produced some synoptic lifting (see Piper et al., 2016, for further details about the synoptic situation).

We introduced the convective adjustment timescale (τ_c) as an objective measure to classify precipitation regimes according to their synoptic forcing. During weak synoptic forcing local triggering processes are necessary to release $CAPE$. For this non-equilibrium type of convection, the time between the buildup of $CAPE$ and its depletion is long after that τ_c increases. In contrast to that, convective precipitation continuously destroys instability ($CAPE$), for example, produced by large-scale lifting, during moderate synoptic forcing. This leads to small values of τ_c. Following previous publications (e.g., Done et al., 2006; Kühnlein et al., 2014), a threshold of $\tau_c = 6\,\text{h}$ is applicable to classify these two weather regimes (see Sec. 2.5 for further details). The daily maximum of domain averaged τ_c is depicted in Figure 3.22a. Applying the threshold of 6 h on the German subdomain (blue line) divides the period into a moderately (29 May – 03 June), and a weakly (04 – 07 June) forced period. Note that we consider this subdomain for the classification of weather regimes in the HIW period. Even though characteristics are similar, the regime change is slightly earlier over the Northern subdomain (black line) while being delayed over the south (gray line).

In line with the change in the synoptic regime, the spatial sum of daily accumulated precipitation (Fig. 3.22b) decreases by about 60 %. While the domain-averaged value is similarly distributed between the northern and southern subdomains during the first phase of the HIW, more precipitation occurs over the southern part of Germany (gray line) for weak synoptic forcing. Similarly, the precipitating fraction (Fig. 3.22c) decreases during the second phase of the HIW whereas the regional differences are less pronounced. Interestingly, daily peak precipitation (i.e. the 95$^{\text{th}}$ percentile of hourly precipitation) is slightly increasing throughout the period in all three domains (Fig. 3.22d). Hence, convection over the northern part of Germany covers smaller regions but is similarly intense as compared to the south. The decreasing mid-tropospheric wind speed (Fig. 3.22e) reduces the influence of advection. This reduction supports stationary convective cells not covering large areas but generating locally high precipitation amounts. The low-level humidity index (see Sec. 2.8) shown in Figure 3.22f reveals another important feature of the HIW period. After the lower atmosphere is quickly moistening during the first day, remains wet throughout the first, moderately forced, phase. With the regime change, dry air reaches the domain leading to an increase in HI_{low}. This drying further changes the expected intensity of the soil atmosphere interaction as atmospheric moisture availability is limited over a fairly large region. According to that, the importance of local evaporation as a source of atmospheric moisture is increasing. The expected intensity of soil-atmosphere interaction increases along with the change in moisture sources during the weakly forced phase of the period.

We furthermore evaluate the ability of COSMO to generally represent the weather situation by comparing the spectral structure of the precipitation fields using wavelet spectra. As opposed to the Fourier transform, which assumes spatial stationarity, wavelet spectra preserves spatial information of the analyzed field. Since a description of the wavelet method is beyond the scope of this thesis, the reader may find a comprehensive overview in Daubechies (1992) or Kaiser (1994). Similar to Brune et al. (2018), we use a Daubechies wavelet, however, using a Daubechies 4 wavelet instead of a Haar wavelet (Daubechies 1; as in Brune et al. (2018)) might decrease

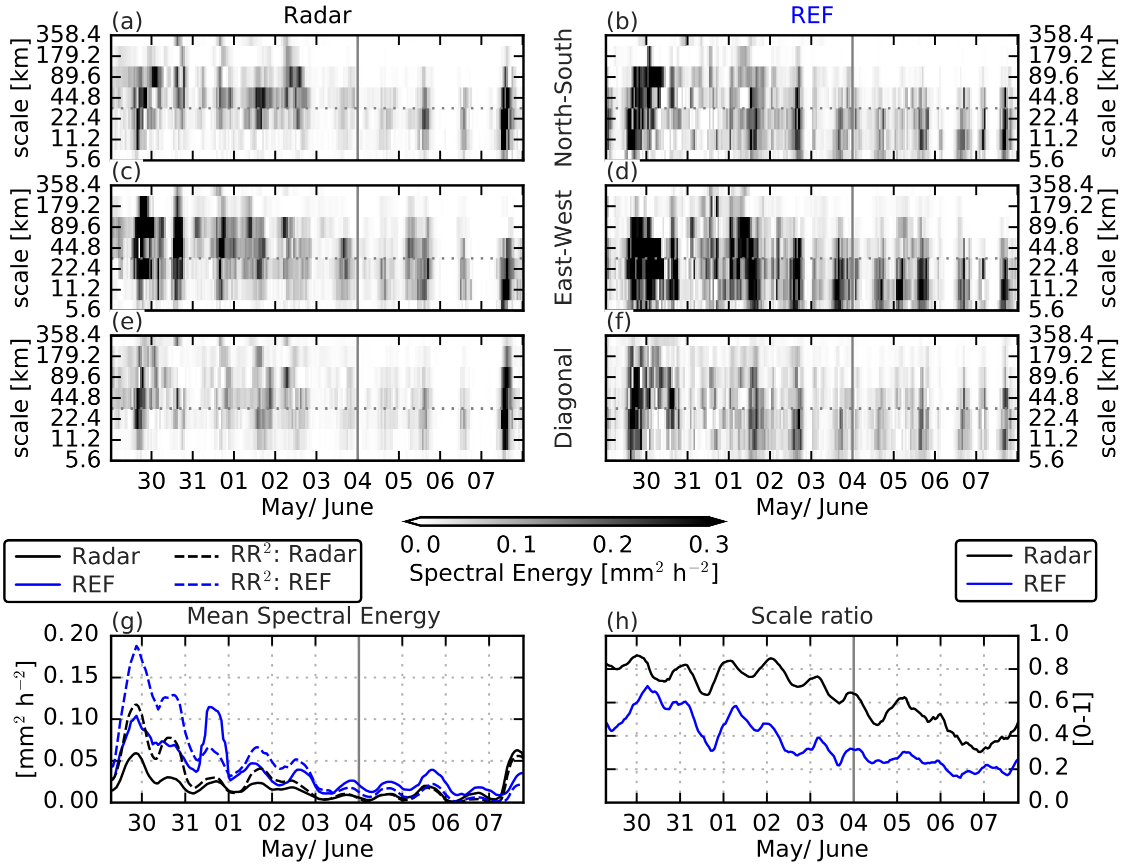

Figure 3.23.: Time series of domain-averaged wavelet spectra of hourly precipitation derived from Radar observations (a,c,e) and the unperturbed reference simulation (REF) (b,d,f). Displayed are the North-South (a,b), East-West(c,d) and Diagonal (e,f) directions. (g) Mean spectral energy averaged over all directions for Radar observations (black) and Ref (blue), as well as squared, domain-averaged hourly rain rates (dashed lines) are displayed. (h) Scale ratio $\langle E_l \rangle / (\langle E_l \rangle + \langle E_s \rangle)$ with $\langle E_l \rangle$ being the average spectral energy for scales from 44.8 km to 358.4 km and $\langle E_s \rangle$ from 5.6 km to 22.4 km. A 12-hourly rolling average is applied to increase readability of g and h.

the sensitivity towards discontinuities in the signal (in our case a precipitation field) but increases frequency resolution of the spectral analysis (Kaiser, 1994). According to, for example, Sharif and Khare (2014), the Daubechies 4 wavelets are superior to characterize spatial data retrieved from remote sensing while Brunsell and Gillies (2003) successfully applied those wavelets to analyze patterns of surface heat fluxes spatially. Recently, Buschow et al. (2019) reported about Daubechies 4 as the optimal trade-off in describing intermittency and smoothness in precipitation fields. A drawback of this method, as for any other wavelet method, is that analyzed scales are in powers of 2, which leads to rapidly increasing analyzed scales. We used zero-padding to increase the field size to the next higher power of two. The algorithm based on Eckley and Nason (2011) calculates the directional wavelet analysis in North-South, East-West, and diagonal directions.

Time series of the domain-averaged spectra are displayed in Figure 3.23 for Radar observations (a,c,e) and REF (b,d,f). The re-occurring dark patches in the time series reflect the daily cycle of convective precipitation with its maximum in the late afternoon. Similar to the domain-averaged precipitation rate (Fig. 3.22d), the color gradients decay throughout the HIW period in all directions of Radar observation and REF simulation. Even though REF slightly overestimates the East-West organization of convective precipitation, patterns in the spectra match reasonably well. Inspecting the magnitude of spectral energy, however, reveals that REF overestimates the sharpness and intensity of convective cells, which is why spectral energy is generally increased. This difference is even more prominent in the mean spectral energy displayed in Figure 3.23g (solid lines) according to which REF continuously shows higher spectral energy as the Radar observations. A comparison of mean spectral energy with the squared, domain-averaged precipitation rate (dashed lines) reveals reasonably good accordance meaning that the wavelet spectra are trustworthy (e.g., Brune et al., 2018). Figure 3.23h shows the ratio between spectral energy on small (i.e. 5.6 km to 22.4 km) and large (i.e. 44.8 km to 358.4 km) scales. This ratio provides information about the average size distribution of convective precipitation fields throughout time and reveals important characteristics of the synoptic conditions in the HIW period. On the one hand, the scale ratio shows a continuously smaller ratio for REF, meaning that the spatial extent of convective cells tends to be too small. The regime change, on the other hand, is more rapid in the observations. While the ratio continuously changes towards smaller values in REF, this transition happens faster in the Radar-derived observations. This transition thus shows that with the synoptic regime, the average size of convective cells changes from larger clusters during moderate synoptic control towards smaller convective cells during the synoptically weakly forced phase. Furthermore, radar observations generally show higher values of this scale ratio hinting on an increased organization of convection to larger clusters as compared to REF. Thus, the HIW period offers the opportunity to examine the relative impact of various perturbations comprising different aspects of uncertainty, conditional to different synoptic forcing conditions.

3.3.2. Precipitation rate and local variability

To get a first impression of the domain-averaged relative influence of the three different perturbation approaches, Figures 3.24a,b show time series of domain averaged precipitation for the two synoptic regimes. High precipitation rates in the morning hours (before 6 UTC) originate from spin up effects caused by the downscaled COSMO-EU initial conditions used for the experiments. The initialization using analysis data also explains the differences between the EPS and the experiments. Apart from those spin up effects, both, operational forecasts and experiments develop a diurnal convective cycle with low precipitation rates in the morning and a pronounced maximum in afternoon precipitation. Comparing the radar observed with our experiments and the operational forecasts, however, reveals a time shift of 1 h too late (2 h too early) for weak (moderate) forcing in the experiments and

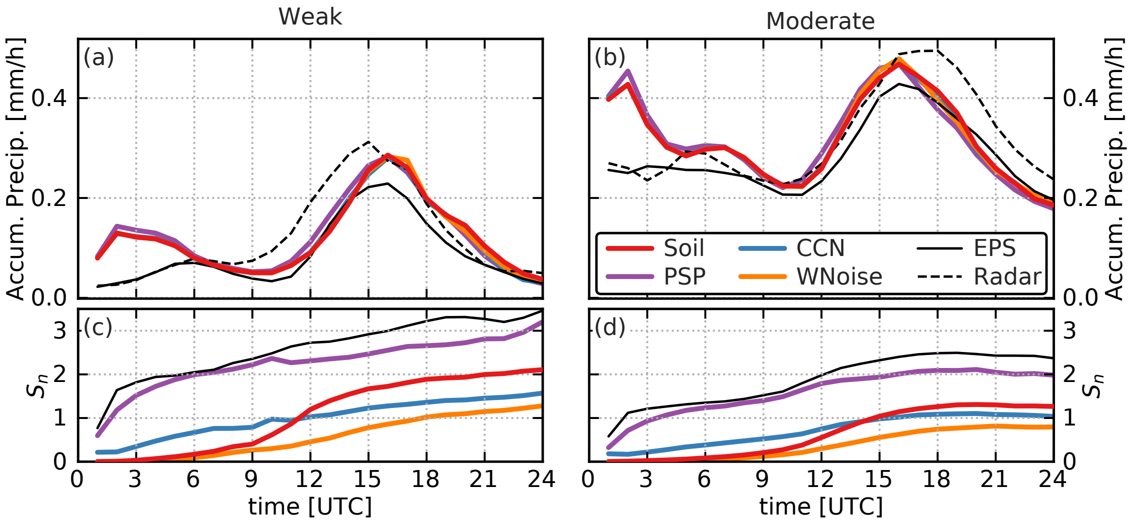

Figure 3.24.: Time series of hourly precipitation (a, c) and normalized precipitation spread $\langle S_n \rangle$ (b, d) averaged over six moderately (a, b) and four weakly (c, d) forced cases evaluated for different COSMO ensembles: prescribed soil moisture heterogeneities (Soil), stochastic boundary layer perturbations (PSP), variations in aerosol concentration (CCN), the operational COSMO-DE-EPS ensemble (EPS) and a reference ensemble perturbed with white noise (WNoise). The daily accumulated radar observations (dashed) separately aggregated over weak (left) and moderate (right) synoptic control provide an informative basis.

operational forecasts paired with higher observed precipitation rates. The use of analysis data to drive our experiments as well as the double-moment microphysics better compares to the observations as the operational forecasts. With a maximum precipitation of about 0.28 mmh^{-1} (0.47 mmh^{-1}) our experiments reach 90 % (95 %) of the radar observations' peak precipitation for weak (moderate) forcing whereas the operational EPS forecast only reach 70 % (85 %). Similar to the peak values, precipitation rates are generally higher for moderate synoptic forcing.

The boxplots in Figure 3.25 visualize the variability in precipitation amount accumulated between 9 and 21 UTC – the period of main convective precipitation – depicting the mean deviation from an unperturbed reference simulation (REF), as well as its median and interquartile range. Values larger (smaller) than one stand for an increase (decrease) in precipitation of the respective perturbed-parameter ensemble compared to REF. The following evaluation will consider the topographical structure of the German domain by dividing it into a relatively flat northern and a mountainous southern subdomain to examine the role of orography paired with different perturbation methods. Note that for both synoptic conditions, comparing all perturbed-parameter experiments with the lower benchmark ensemble (WNoise) reveals both, a broader interquartile range and envelope. The perturbed-parameter ensembles thus produce more variability as compared to white noise perturbations implying a physical cause of the variability.

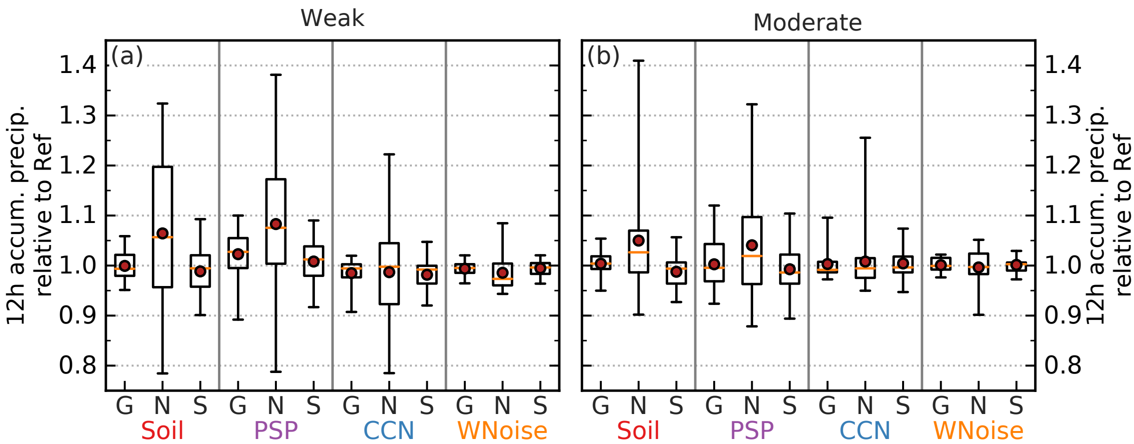

Figure 3.25.: Relative change in precipitation accumulated from 09 UTC to 21 UTC for all Soil, CCN, PSP, and WNoise perturbed-parameter ensembles grouped in weak (a) and moderate (b) forcing. Evaluations are performed for the German (G), as well as the Northern (N) and Southern (S) German subdomains. The upper and lower whiskers show the envelope of all experiments, the boxes the interquartile range (25$^{\text{th}}$ and 75$^{\text{th}}$ percentile) and the orange lines the median. Red circles indicate the mean values.

Among all perturbed-parameter ensembles, CCN shows the smallest variability over all three subdomains. The large spread for weakly forced conditions over northern Germany (Fig. 3.25a) originates from the simulation with maritime aerosols underestimating precipitation on 6 June 2016 and overestimating precipitation on 7 June 2016 over Northern Germany. This misrepresentation broadens the distribution, whereas the mean and median remain close to one. Furthermore, it does not show a strong dependence on the synoptic regime as the distributions are only slightly broader for weak forcing (Fig. 3.25a) as compared to moderate forcing (Fig. 3.25b). Stochastic boundary layer perturbations (PSP) generate the largest variability among all perturbation approaches over the German subdomain. Both the interquartile range and envelope surpass the other ensembles. Additional heterogeneity in the BL shows a larger impact over the fairly flat northern part of Germany as compared to the mountainous south resulting in a broadening of the distribution and a shift of mean and median towards about 10 % (5 %) increase for weak (Fig. 3.25a) (moderate; Fig. 3.25b) forcing. In contrast to that, the mean and median center around one for the southern subdomain. Similar to Figure 3.24, the perturbed initial soil moisture conditions (Soil) reveal the most considerable regime dependence. While the mean and median remains close to one for the German subdomain as the domain-averaged soil moisture remains equal for all simulations, the interquartile range almost doubles for weak as compared to moderate forcing. The entire envelope, however, is similar for both ensembles. Regional differences are, as already seen for the PSP ensemble, large for the Soil ensemble. Over Northern Germany, where terrain variability is limited, soil moisture perturbations generate large variability and produce on average above 5 % more precipitation for both synoptic regimes. Note that the respective median value for moderate synoptic forcing remains close to one, implying that the average increase is due to the skewed distribution illustrated by the envelope. The variability over the southern subdomain is, similar to PSP, comparably small.

While the mean precipitation rates of the sets of experiments only vary within a range of 5 %, ensemble variability varies between different perturbation approaches. In order to assess the local ensemble variability, we calculate the normalized standard deviation

$$S_n(x,y) = \frac{1}{\overline{P(x,y)}}\sqrt{\frac{1}{N-1}\sum_{i=1}^{N}\left(P_i(x,y) - \overline{P(x,y)}\right)^2} \tag{3.3}$$

with N being the number of ensemble members, $P_i(x,y)$ each member's rain rate and $\overline{P(x,y)}$ the ensemble mean precipitation rate (Hohenegger et al., 2006) in Figures 3.24c,d. Generally, the division by $N-1$ rather than N compensates for the fact that the individual members are, on average, closer to their sample mean than to the true population mean (Wilks, 2011). The ensemble spreads of all perturbed-parameter ensembles are well distributed between the two benchmark simulations WNoise and EPS. Since statistical white noise generates the variability in WNoise, being larger as WNoise indicates that the processes leading to ensemble variability are physically based. The CCN ensemble causes steadily increasing variability from the beginning of the simulation but ends having the smallest ensemble spread. Since microphysical processes continuously take place during the formation of clouds and precipitation, CCN perturbation shows constant influence notwithstanding different stages within the cycle of convection. PSP, instead, shows rapid growth in variability at the beginning and reaches about 85 % of the EPS's variability at the time of simulated peak precipitation (about 16 UTC) as the direct perturbation of tendencies in the BL is very effective. Therefore the PSP ensemble outperforms the other perturbed-parameter ensembles. While all ensembles show a fairly steady increase throughout the day, the Soil ensemble reveals an exciting feature. Before sunrise (about 4 UTC), there hardly is an increase in ensemble spread. A period of very gentle increase follows before Figure 3.24c shows a rapid increase in ensemble spread just before the onset of convective precipitation between 9 and 12 UTC (11 and 14 UTC) for weak (moderate; Fig. 3.24d) forcing. Since heterogeneous soil moisture perturbations mainly influence the convection initiation via secondary dynamical effects, like thermally induced circulation cells and boundary layer rolls (see Section 3.2), the most substantial increase in variance is discernible during this period. Therefore it outperforms the CCN ensemble throughout the day and amounts to about 55 % (50 %) of the EPS's spread at 16 UTC for weak (moderate) forcing. With the EPS ensemble employing perturbations all three major sources of uncertainty accounting for initial and boundary condition uncertainty as well as the model error, it outperforms all other experiments.

Comparing the different weather regimes shows a similar stratification of simulations but reveals a regime dependent impact of perturbations. While ensemble spread is generally larger for weak synoptic forcing the differences are not equal for all simulations. Again, soil moisture perturbations show a striking behavior as its spread is about 50 % larger for weak synoptic forcing (Fig. 3.24c) as compared to moderate synoptic forcing (Fig. 3.24d). In contrast to that, the remaining ensembles show a reduction in spread amount to roughly 25 % to 30 %. As already discussed in Section 3.2, soil moisture perturbations are primarily dependent on solar radiation and the background wind, which partly explains the regime dependence.

The effect of the different ensemble sizes was further tested by applying a resampling method with replacement. Drawing 1000 times four individual model runs in each ensemble (Soil, PSP, CCN, WNoise, and EPS) on each day results in 1000 samples per perturbed-parameter ensemble (each consisting of 4 members). The application of this method to compute the domain-averaged precipitation rate and normalized ensemble spread gives qualitatively very similar results with the same order in the importance of the different perturbations (not shown).

In summary, aerosol and stochastic boundary layer perturbations reshuffle the location of precipitation from the model start onwards hence leading to increasing local precipitation variability from the beginning. Soil moisture perturbations, instead, show the largest generation of variability during convection initiation. In general, stochastic boundary layer perturbations are most efficient and produce the largest local variability, almost reaching the upper benchmark (EPS). Moreover, all perturbed-parameter ensembles, in particular, the soil moisture perturbations, show a clear weather regime dependence. While ensemble spread shows differences between the perturbation approaches, domain and ensemble-averaged precipitation amounts are hardly affected by the different perturbations. This hints on the perturbations are mainly redistributing convection within the domain rather than generally modifying the magnitude of convective precipitation. Furthermore, perturbation methods directly acting on the BL and thus causing additional heterogeneity generates a larger variability in 12 hourly accumulated precipitation over the orographically less structured northern part of the German domain.

3.3.3. Spatial precipitation variability

To investigate the relative spatial impact of the different perturbed-parameter ensembles, we will apply the FSS (see Section 2.7) to evaluate the spatial variability of deep convection caused by the perturbations. We produce the binary field using the 95^{th} percentile precipitation as threshold and, unless mentioned differently, allow for a spatial inaccuracy of 11 grid cells (30.8 km). For the calculation of the FSS compare the perturbed-parameter ensembles with REF. While a FSS of one is considered to be a perfect forecast, smaller values stand for increasing spatial variability. The FSS values are averaged over both the ensemble members and all case studies categorized as the same synoptic regime. Since the computation of FSS for the operational EPS relative to REF driven with analysis would result in an unfair comparison, we excluded it from this application.

The ensemble mean FSS (Fig. 3.26) reveals that the stochastic boundary layer perturbations cause variability from the initialization time onwards and exerts the largest influence on convective precipitation among the perturbations. This is similar

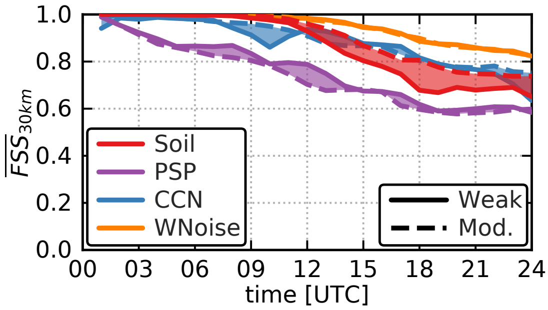

Figure 3.26.: Time series of the ensemble mean Fractions Skill Score (FSS) relative to REF for all perturbed-parameter ensembles for the HIW period. The shaded regions illustrate the differences between the weakly (solid) and moderately (dashed) forced cases. Calculations were performed using the 95$^{\text{th}}$ percentile precipitation as threshold and a spatial scale of 11 grid cells (roughly 30 km).

to the normalized standard deviation (Figs. 3.24b,d). Spatial variability is steadily increasing throughout the simulation time. However, unlike the normalized spread, it does not show any significant dependence on the synoptic forcing as the solid (weak) and dashed (moderate) behave similarly. Spatial variability generated by perturbations of the aerosol concentrations (CCN) is delayed as compared to the ensemble spread but also shows a constant increase after 6 UTC. Similar to the ensemble spread (Fig. 3.24b,d), the Soil ensemble hardly shows any change in variability before 9 UTC but afterward executes a rapid increase prior to the onset of afternoon precipitation.

Similar to the PSP ensemble, CCN shows a small weather regime dependence. In contrast to those, soil moisture perturbations show a pronounced regime dependence. Different initial conditions in soil moisture result in variations in the initiation location of convection being more efficient for weak synoptic forcing where soil-atmosphere interactions are more pronounced. There still is a steeper increase in spatial variability before main afternoon convective precipitation for moderate synoptic forcing whereas it is slightly delayed and less distinct. After 18 UTC (after peak precipitation in Fig. 3.24a,b) FSS values stagnate for both synoptic regimes.

Relaxing the constraint of a fixed spatial scale for the computation of the FSS leads to Figure 3.27 showing the FSS score similarly computed as in Figure 3.26 but for scales ranging from 5.6 km to 84 km. For both synoptic situations, the WNoise ensemble only reveals small FSS values for scales below 30 km (Figs. 3.27d,h). Furthermore, the difference between weak and moderate synoptic forcing (Fig. 3.27l) is close to zero and thus supports WNoise being independent on the synoptic regime across all spatial scales. Perturbed aerosol concentrations (Figs. 3.27c,g) mainly show large FSS for small spatial scales, whereas the decrease towards larger FSS is very smooth, and the increase of spatial scales showing spatial variability is continuously increasing from the initialization onwards. A very efficient perturbation of convective precipitation across all scales is generated by stochastic BL perturbation (Figs. 3.27b,f). Only slightly dependent on the synoptic regime (Figs. 3.27j), the color shading reveals a rapid growth of scales showing spatial variability in PSP.

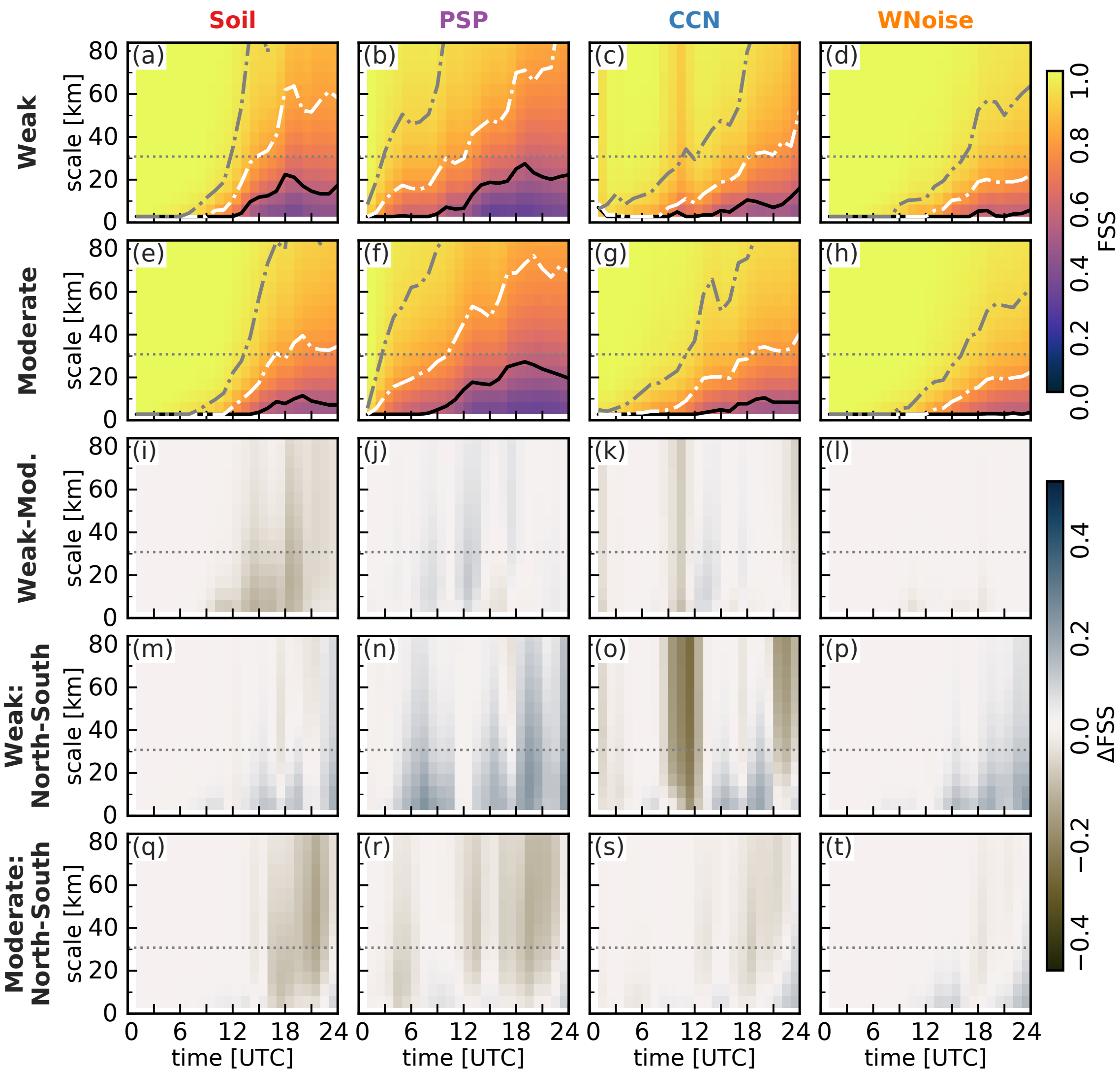

Figure 3.27.: Time series of FSS computed relative to a reference using the 95$^{\text{th}}$ percentile precipitation as threshold for different window sizes ranging from 5.6 km to 84 km (y-axis). The mean ensemble FSS averaged over all weakly (first row, a-d) and moderately (second row, e-h) forced case studies evaluated for the Soil (first column), PSP (second column), CCN (third column) and WNoise (fourth column) ensembles. Colder colors (decreasing values) stand for an increase of spatial variability. Additionally, the useful ($FSSd50$, black, solid line), 75 % ($FSSd75$, white, dash-dotted line) and 90 % ($FSSd90$, gray, dash-dotted line) scales are displayed considering the same precipitation threshold. The third row (i-k) provides the difference of FSS (ΔFSS) between the different forcings. Positive (negative) values (blueish (brownish) colors) describe more variability for moderate (weak) forcing. The lowest two rows (m-t) depict regional differences between northern and southern Germany for weak (m-p) and moderate (q-t). Positive (negative) values (blueish (brownish) colors) describe more variability over the southern (northern) subdomain. The 30.8 km scale applied in Figures 3.26 and 3.28 is marked by the gray dotted line.

Findings described for Soil in Figure 3.26 are transferable to other spatial scales. Following the color gradient for weak synoptic forcing (Fig. 3.27a) reveals a steeper increase of perturbed scales as compared to moderate forcing (Fig. 3.27e). Accordingly, larger scales are perturbed under weak synoptic forcing. Consistently negative values in the difference plot (Fig. 3.27i) support the strong regime dependence with more efficient perturbation for weak synoptic forcing.

Inspection of the low dispersion scales ($FSSd50$) confirms the distinguished regime dependence of the Soil ensemble. The spatial dispersion scales describe the spatial scale at which a particular level of spatial variability (quantified by FSS) is reached (see Section 2.7). While the Soil experiments substantially diverge only until a spatial scale of about 10 km for moderately forced situations, the low dispersion scale is 20 km for weak synoptic forcing (Fig. 3.27a,e). By contrast, this scale is almost insensitive to the synoptic regime for the remaining two perturbed-parameter ensembles amounting to about 30 km (PSP; Fig. 3.27b,f) or 10 km (CCN; Fig. 3.27c,g). The lower benchmark experiment (WNoise), instead, does hardly show growth in the lower dispersion scale. Amending the concept of the low dispersion scale by applying different thresholds provides insight into the growth of particular levels of spatial inaccuracy in scale throughout time. This is based on the assumption that deviations in fractional coverage and displacement in precipitation are necessary to reduce the FSS to a certain value (i.e. approximately 0.75 ($FSSd75$) or approximately 0.90 ($FSSd90$; see Section 2.7). The rate of change in spatial scale at which a specific spatial variability occurs can be tracked throughout time. The 75 %- and 90 %-scale is shown by the white and gray dash-dotted lines in Figures 3.27a-h. Similar to $FSSd50$, $FSSd75$ is almost regime independent for CCN, PSP and WNoise and levels off at about 30 km (CCN), 70 km (PSP) and 20 km (WNoise). Again, Soil shows a pronounced regime dependence whereupon $FSSd75$ is 60 km for weak synoptic situations (Fig. 3.27a) and about 30 km for moderately forced cases (Fig. 3.27e). During the forecast lead time of 24 h, not all experiments reach a stagnation of high dispersion scale ($FSSd90$). While $FSSd90$ keeps growing larger for CCN (reaches up to 150 km), it just decelerates for PSP and reaches almost 200 km. Soil settles at about 150 km (weak; Fig. 3.27a) and approximately 100 km (moderate; Fig. 3.27e), respectively. Note that Figure 3.27 only shows scales up to 84 km.

Differences in the three regarded scales mainly arise from a different growth rate. Thus, small spatial variability values show more rapid growth than higher spatial variability. While CCN and WNoise reveal comparably small growth rates, PSP shows the quickest growth. Interestingly, $FSSd90$ for Soil starts growing at about 09 h and gradually accelerates until it reaches its final scale at about 18 h. Furthermore, its fastest growth rate is comparable to PSP.

The orographic structure of the German domain provides the opportunity to examine the role of orography paired with different perturbation methods. For simplicity, we confine the spatial scale to 30.8 km in Figure 3.28 (cf. Fig. 3.26) and we omit the CCN and WNoise ensembles as Figure 3.26 reveals less pronounced effects on spatial variability. For both subdomains, the PSP ensemble causes spatial

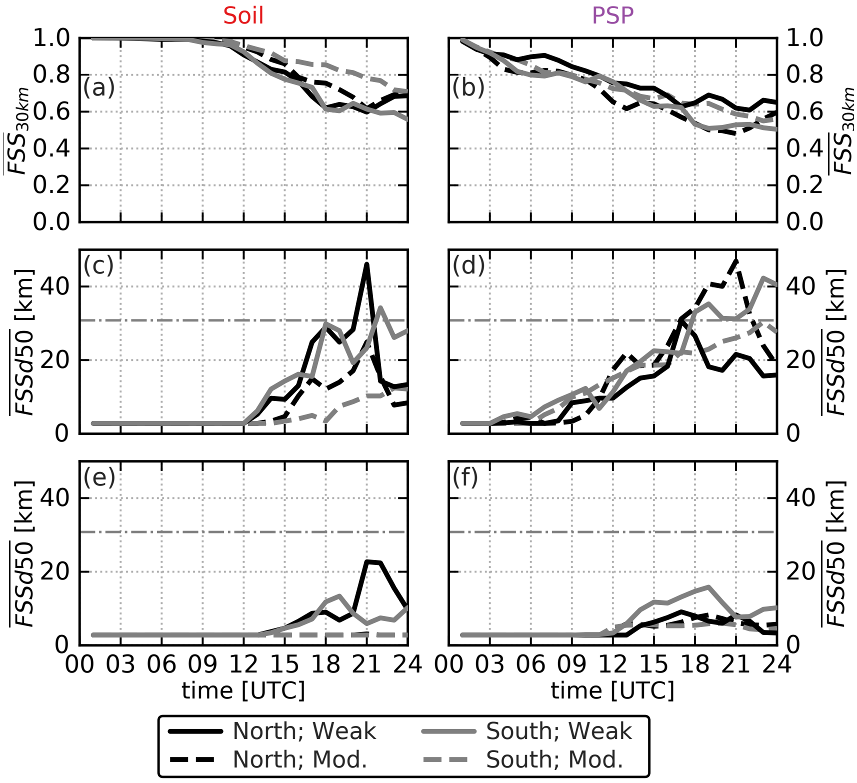

Figure 3.28.: Regional difference of the ensemble averaged FSS for the Soil (a) and PSP (b) ensembles in northern and southern subdomains using the same thresholds as in Figure 3.26. The low dispersion scale ($FSSd50$) using the 95$^{\text{th}}$ percentile precipitation as a threshold is displayed in the second row for the Soil (c) and PSP (d) ensembles in northern and southern subdomains. (e,f) shows the same as (c,d) but applying the 80$^{\text{th}}$ percentile precipitation as a threshold.

variability from the start onwards with a similar descent in FSS hinting on a small regional dependency. Looking at the low dispersion scale ($FSSd50$) in Figure 3.28d confirms the rapid growth in low dispersion scales until about 17 h. Afterwards, however, $FSSd50$ keeps growing over the northern subdomain for moderate forcing while it slightly descents for weak forcing resulting in a maximum difference in low dispersion scales of 20 km. This might imply that grid-scale inhomogeneities in the absence of orography are more efficient for moderate as for weak synoptic forcing. For the southern subdomain, instead, $FSSd50$ grows for both synoptic regime although there is an increased growth discernible for weak synoptic forcing. This hints on the increased influence of orographic triggers during weak forcing conditions.

This characteristic differentiates the Soil ensemble from the other perturbed-parameter ensembles. During weak synoptic forcing, there is a similarly large impact of heterogeneous soil moisture perturbations due to the strong soil-atmosphere interaction over both domains (Fig. 3.28a). This leads to a redistribution of convection and impacts the spatial structure of the precipitation field, resulting in a reduced FSS. The impact is generally smaller during moderate forcing. However, the absence of orographically induced variability over flat terrain leads to a relatively larger impact of soil moisture heterogeneity on spatial precipitation variability over the flat northern subdomain during moderate synoptic control. Another aspect distinguishing Soil from the other two perturbed-parameter ensembles is the broad range of spatial scales $FSSd50$ involves considering the collective impact of orography and synoptic situation (Fig. 3.28c). Before 12 h, $FSSd50$ does not show any change. Regional differences are, on average, very small for weak synoptic conditions showing a scale of about 30 km. Interestingly, spatial variability caused by soil moisture perturbations over the northern subdomain is higher as generated by PSP. This different behavior of Soil and PSP experiments might be caused by the larger spatial correlation of the soil moisture perturbations more efficiently generating small-scale dynamical triggers as opposed to the grid-scale perturbations caused by PSP. Regime dependence, however, shows large regional differences. Similar to the FSS in Figure 3.28a, there is larger regime dependence over the southern subdomain. While differences in $FSSd50$ of about 15 km occur over the North, discrepancies amount up to 30 km over the orographically structured southern subdomain. This again underlines orographic triggers being more important as compared to soil moisture perturbations during moderate synoptic forcing.

Figure 3.27m-t depict regional differences for multiple spatial scales and different synoptic situations. Negative outliers for CCN (weak forcing) are visible throughout all spatial scales in Figure 3.27o. This supports the misrepresentation of individual convective cells over the northern subdomain, as mentioned above. Similar to that, the remaining experiments, especially PSP, show increased spatial variability for the orographically more structured southern part of Germany for weak synoptic forcing. In contrast to that, the sign is reversed for moderate synoptic forcing (Figs. 3.27q-t). While the effect is very small for CCN and WNoise, Soil and PSP show a definite increase in variability across all spatial scales for moderate synoptic forcing. For Soil, the increase in spatial variability during moderate synoptic forcing is mainly constrained to the afternoon and evening hours. As those perturbation methods both act directly on the BL, this again hints on the regime dependent effect of orography, soil and BL perturbations on the initiation of deep convection.

Applying the 95^{th} percentile precipitation as a threshold for the computation of FSS only features the peak values of convective precipitation. Relaxing that threshold to the 80^{th} percentile allows to assess broader-scale features represented in the Soil and PSP ensembles (Fig. 3.28e,f). For the two displayed perturbed-parameter ensembles, the low dispersion scale ($FSSd50$) reveals a smoother increase throughout time as already hypothesized by Dey et al. (2016). Additionally, both ensembles still support the results described above for the more restrictive precipitation threshold in Figures 3.28c,d. The smooth increase leads to a spatial variability is small for the PSP ensemble (Fig. 3.28f). However, the largest spatial variability appears over the orographically structured southern part during weak synoptic control. Despite the weaker constraining precipitation threshold, heterogeneous soil moisture perturbations still cause spatial variability during weak synoptic forcing especially over the northern subdomain (Fig. 3.28e). During moderate synoptic forcing, no increase in

$FSSd50$ is discernible. This again supports that heterogeneous soil moisture perturbations predominantly alter the triggering mechanism locally forced convection during weak synoptic forcing and shows minor effects during moderate synoptic forcing when large-scale triggers are more dominant. Furthermore, the reduced low dispersion scale supports our hypothesis that heterogeneous soil moisture perturbations predominantly affect local triggering mechanisms rather than changing general precipitation.

3.3.4. Discussion and summary

The previous Section 3.2 showed a strong coupling between heterogeneous soil moisture and convective precipitation on daily time scales by evaluating the effect of chessboard patterns on convective initiation. Even though findings are based on real-case scenarios and introduced gradients are shown to relevant dynamical effects, heterogeneous soil moisture initializations are pragmatically chosen to identify dominant processes and heterogeneity length-scales. That way, we learned about dynamical processes strongly influencing convective precipitation on a local scale. A step further towards realistic perturbations is to adopt the spatial scales found in the previous section for spatial filtering using High-, Low- and Band-pass filters. Furthermore, we additionally chose to include perturbation length-scales used in the new, KENDA based ensemble system at DWD (Schraff et al., 2016; Theis et al., 2017). Several studies argued that proper representation of the spatial distribution of initial soil moisture is essential by showing that forecast quality of specific precipitation events suffers from inadequate representation (e.g., Chang and Wetzel, 1990; Trier et al., 2004; Cheng and Cotton, 2004; Koukoula et al., 2019). Therefore, spatial inaccuracy is expected to increase variability in convection hence increasing ensemble spread. Note that we did not alter domain averaged soil moisture as this would lead to a bias in average precipitation. Another open issue is the relevance of soil moisture perturbations, which can be assessed by comparing with other major sources of uncertainty, like CCN and PSP. Important physical mechanisms are linking those specific sources of uncertainty for deep convection. We computed those perturbed-parameter ensembles for ten days of daily occurring high impact weather across Central Europe featuring different synoptic conditions. Furthermore, the operational COSMO-DE-EPS forecasts are available for the sake of comparison.

Dependence on the synoptic regime and temporal evolution of variability

The area- and ensemble mean hourly precipitation rates of the different ensembles closely agree but show differences conditional to the synoptic regime. Differences in average 12-h accumulated precipitation (09-21 UTC) remain below 5 % and are generally smaller for moderate synoptic forcing ($\mathcal{O}(1\,\%)$). This overall robustness of precipitation is in agreement with a study of Seifert et al. (2012) who find aerosol effects on 12-h accumulated area-averaged precipitation below 5 % in a 3-yr climatology of summertime precipitation over Germany as simulated by the COSMO model. Furthermore, previous Sections 3.1 and 3.2 showed small average effects of heterogeneous soil moisture perturbations on mean precipitation as long as domain averaged soil moisture remains unchanged.

Ensemble (S_n) and spatial spread (FSS, $FSSd50$) support the regime dependent influence of perturbations on convective precipitation with larger variability during weak forcing. The operational COSMO-DE-EPS forecasts sampling the main sources of uncertainty present the highest variability. This is in agreement with earlier studies pointing towards the importance of initial and lateral boundary condition uncertainty in convection-permitting EPSs (e.g., Surcel et al., 2017). Physical relevance of the three perturbed-parameter ensembles is implied by outperforming the lower benchmark ensemble (WNoise) initialized with white noise perturbations of the temperature. Both, stochastic boundary layer perturbations and CCN variations induce variability shortly after the beginning of the simulation regardless of the onset of the main convective precipitation around noon. While PSP produces about 85 % of the total EPS ensemble precipitation variability, the CCN ensemble accounts for approximately 40 % during weak forcing. Note that those values are not generally applicable and are restricted to the configurations in this thesis while giving a first estimation of the relative influence of different perturbation methods on the ensemble spread. Those values mainly show that the effect of all perturbed-parameter ensembles is not negligible. Interestingly, heterogeneous soil moisture perturbation shows two characteristics differentiating it from the other perturbed-parameter ensembles. Its ensemble variability shows the largest regime dependence among the ensembles being capable of accounting for about half of the operational EPS variability during the most intense rainfall period in the afternoon. Since heterogeneous soil moisture perturbations mainly influence the convection initiation, the largest increase in variance is discernible at this time (between 09 and 21 UTC). Furthermore, it does not cause major spatial or ensemble variability from the beginning of the simulation. After a period of hardly discernible increase, variability sharply increases in spread prior to the onset of heavy afternoon precipitation. Those results are also supported by the FSS quantifying the spatial variability of the perturbed-parameter ensembles.

Furthermore, evaluation of the temporal change of characteristic dispersion scales ($FSSd50$, $FSSd75$, $FSSd90$) also supports the delayed increase in spatial variability caused by soil moisture perturbations. Irrespective of the dispersion scale, variability starts to increase just before the onset of convective precipitation. The growth-rate of spatial inaccuracy expressed by different spatial deviation scales is generally higher the smaller the respective spatial inaccuracy is. However, the time when the deviation scale starts to grow is hardly changing for the Soil ensemble. In contrast to that, the growth starts significantly earlier, considering smaller spatial inaccuracies for the remaining perturbed-parameter ensembles. This comparison further supports the soil moisture perturbations' unique characteristic to start generating variability just before convection initiation.

Regional differences

Manipulations of the concentration of CCN show a similar impact for both German subdomains. Differences in spatial variability over the Northern part probably stem from misrepresentations of convective precipitation for the simulation with maritime aerosol concentration (i.e. the cleanest conditions of the four options). According to Tao et al. (2012) and references therein, this favors the suppression of warm rain. A more in-depth evaluation of this issue, however, is beyond the scope of this thesis. Interestingly, the regime dependent impact of the remaining two perturbations shows remarkable regional differences. While ensemble variability generally shows larger variation between the members over the northern part, the influence of the perturbations on spatial variability behaves differently for the perturbation methods. Regime differences over the Southern subdomain are comparably small for PSP. Only after 18 UTC, FSS starts to diverge and reveals larger variability for weak synoptic forcing. Over Northern Germany, stochastic BL perturbations generally show a larger impact for moderate synoptic forcing. Following the low spatial dispersion scale ($FSSd50$) reveals large differences of almost 20 km during that period, also implying higher spatial variability moderate synoptic forcing. This hints on the stochastic BL perturbations, on the one hand, amplify with small-scale, orographic effects. On the other hand, they do not efficiently cause variability in the absence of orography. In contrast, Soil perturbations hardly show a regional dependence for weak synoptic forcing neither for a fixed scale (i.e. $\overline{FSS}_{30\,\mathrm{km}}$), nor across different scales ($FSSd50$). Since spatial dispersion scale keeps growing in the afternoon, the Soil ensemble reveals even higher spatial variability over the North as that generated by PSP. During moderate synoptic forcing, instead, there are substantial regional differences for the Soil ensemble. While the low dispersion scale if about 20 km over the North, it remains below 10 km over the South. In other words, soil moisture perturbations hardly show impact over orographically structured terrain during moderate synoptic forcing. Over the Northern part, where orographic triggers are missing, it still produces substantial spatial variability even though synoptic conditions would not favor a strong soil-atmosphere interaction. Henceforth, the small dynamical disturbances produced by different initial soil moisture realizations can – in the absence of orography – still provide important triggering mechanisms for deep convection. Orographic effects in the South suppress the effect of those small-scale disturbances.

Furthermore, comparing values of $FSSd50$ for the Soil ensemble and the bias experiments in Section 3.1 supports our hypothesis after what initial soil moisture bias predominantly amplifies different convective cells rather than causing substantial spatial variability. Values $FSSd50$ for the bias experiment remained below 10 km (Fig. 3.6), low spatial dispersion scale is more than double in case of heterogeneous soil moisture perturbations applies in Soil (Figs. 3.27a-h). Those differences in spatial variability distinguishing homogeneous and heterogeneous soil moisture perturbations emphasizes the fundamental influence of soil moisture gradients exert on convective precipitation.

In summary, this section shows the complex interplay between synoptic conditions comprising thermodynamic stratification and available net radiation modulating the influence of different perturbations on convective precipitation. Soil moisture perturbations can generate variability comparable with stochastic BL perturbations or varied CCN concentrations. Thus, its variability can account for almost half of that produced by the operational COSMO-DE-EPS. We found exciting features of initial soil moisture perturbations discerning them from the other two perturbed-parameter ensembles. Soil perturbations show the most considerable dependence on the synoptic regime and generated the most substantial uncertainty during weak synoptic forcing where soil-atmosphere interactions are most prominent. For those synoptic conditions, the lack of small-scale variability in the lower boundary condition of convective-scale NWP is shown to cause major issues, especially during the initiation phase of convection (e.g., Kühnlein et al., 2014). We hypothesize that perturbations of soil moisture mainly unfold their impact exactly during that phase as heterogeneities mainly influence the convection initiation via secondary dynamical effects, like thermally induced circulation cells and boundary layer rolls. Consequently, spatial and ensemble variability increases just before the onset of afternoon convective precipitation. While the impact of heterogeneous soil moisture perturbations is small over Northern Germany, the southern subdomain shows larger regime dependence. During moderate synoptic forcing, orographic triggers tend to suppress the effect of heterogeneous soil conditions. For weak synoptic control, however, heterogeneities in soil generate substantial variability in convective precipitation.

A limitation of this study might be the differently sized and partly small ensembles. The results appeared robust when testing the effect of different ensemble sizes using a resampling method with replacement. This is supported by Clark et al. (2011) who found statistically indistinguishable results for small ensemble sizes (3-9 members) compared to their full 17-member ensemble investigating precipitation forecast skill in convection-permitting ensembles. We are, therefore, convinced that the differently sized perturbed-parameter ensembles give evidence on the sensitivities of precipitation forecasts to different types of perturbations. Thus, heterogeneous soil moisture perturbations cause valuable variability in regions and during synoptic situations where sufficient small-scale variability in the lower boundary conditions is missing in current NWP models.

4. Conclusion

Deep moist convection is one of the most hazardous small-scale events affecting many socioeconomic sectors (Jahn, 2015) and causing the largest number of insured financial losses (Mills, 2005; Kunz et al., 2009). The potentially dramatic impact on general public arouses great interest in an accurate weather forecast. Even though modern Numerical Weather Prediction benefits from tremendous scientific advances, the quantitative forecast convective precipitation remains a major challenge (Clark et al., 2016). Motivated by the chaotic nature of the atmosphere, Ensemble Prediction Systems predict the probability density function rather than performing a single deterministic forecast. An ensemble generates a set of forecasts and accounts for the three major sources of uncertainty including, initial conditions, lateral boundary conditions, and physical descriptions of the model (e.g., Slingo and Palmer, 2011). The ensemble spread is supposed to adequately represent the forecast uncertainty and should, therefore, give the forecaster guidance about the forecast's accuracy. However, those ensembles are often underdispersive for locally triggered, convective precipitation.

A way to mitigate this underdispersion is to improve the representation of the uncertainty in small-scale processes. Convection is mainly triggered as a reaction of local, small-scale mechanisms. To adequately resolve those mechanisms the grid spacing should be an order of magnitude smaller (i.e. $\mathcal{O}(100\,\mathrm{m})$; Bryan et al. (2003)) than the grid spacing of approximately 2.8 km operationally used in the local area model at DWD. Hence, small-scale Boundary-Layer processes, such as convergence lines, differential or elevated heating, or land surface-atmosphere interactions, are hardly resolved in current weather models. For example, modern convective-scale Ensemble Prediction Systems often attempt to represent initial condition uncertainty by downscaling of coarser-resolution large-scale driving models. However, convective-scale uncertainties are hardly captured by coarse-resolution driving models whereas resolved uncertainties require about 9–12 h to grow downscale and produce small-scale variations (Raynaud and Bouttier, 2016). This time is often too long to fundamentally affect a forecast of locally triggered convective precipitation on a daily timescale.

Improving the uncertainty representation by applying perturbations on convective scales is a promising way to improve ensemble spread of precipitation forecasts. Coupling processes, such as the soil moisture-precipitation coupling (SMP coupling), base on dynamical modifications of the lower troposphere by differential heating. Heterogeneous soil moisture affects precipitation on different spatial and temporal scales. However, sign and magnitude of the SMP coupling on different spatial scales, as well as the collective effect of soil moisture anomalies with different heterogeneity length-scales, are still under debate. Furthermore, existing literature rarely discusses those processes regarding real-case scenarios in operationally used convection-permitting weather models.

SMP coupling, however, has the potential for operational weather forecasting as applying targeted perturbations in initial soil moisture conditions might increase variability in location and intensity of convective precipitation by altering the strength and location of low-level triggering mechanisms. Those small-scale processes are poorly resolved in operationally used convective-scale forecasting models.

In this thesis, particular focus is laid on the influence of soil moisture heterogeneity on convective precipitation by modifications of the lower troposphere's dynamics. We addressed this by a hierarchy of convection-permitting COSMO simulations over the Central European region simulating several real-case scenarios with different synoptic conditions. The first part focuses on the exclusive impact of different artificial initial soil moisture perturbations on the initiation of convection and subsequent precipitation. In this part, we investigate the impact of homogeneous perturbations, as well as its combination with soil moisture heterogeneity at different spatial scales on convective precipitation.

The second part of the thesis concentrates on the relative influence of soil moisture heterogeneity on precipitation in comparison to the influence of two other specific sources of uncertainty in the process of convection initiation and formation of precipitation. The first source of uncertainty comprises the missing spatial variability in the Boundary-Layer (BL). Stochastic perturbations of the BL reintroduce this missing small-scale variability. Those BL perturbations influence the initiation process of convection and hence potentially increases the ensemble spread. Second, Perturbations of the CCN concentration in the atmosphere influence convection in two ways. On the one hand, this generates variability in cloud formation and, on the other hand, influences the surface heat budget by cloud-radiation interactions. Comparing those perturbed-parameter ensembles with a state-of-the-art, operational Ensemble Prediction System is meant to prove the relevance of the perturbations. A more in-depth understanding of the relative impacts of these different perturbation methods in the light of varying synoptic situation is essential for the design of future Ensemble Prediction Systems.

By elaborating on those issues, this thesis provides a first step in transferring findings from highly idealized modeling studies into a real-case application and gives insight into the relative contribution of soil moisture heterogeneity in an operationally used convection-permitting weather model. The following three subsections provide short answers to the research questions posed in the introduction. Furthermore, those subsections also summarize the findings of this thesis according to the research questions. Finally, an outlook and implications for future research will be provided at the end of this chapter.

RQ-1: How does a bias in initial soil moisture conditions affect convective precipitation under different synoptic regimes?

> A bias in initial soil moisture leads to a nonlinear, but positive coupling with convective precipitation on a daily timescale. The influence is larger for weak synoptic forcing. This contributes to the general understanding as it proves the importance of initial soil moisture conditions for the forecast of convective precipitation. The influence, however, is dependent on the synoptic regime.

This question was addressed by simulating several weakly and moderately forced case studies with a homogeneous initial soil moisture bias of $\pm 25\,\%$. The evaluation of 17 real-case scenarios reveals a nonlinear effect on the forecast of convective precipitation within a time horizon of one day. Analyzing domain-averaged evaporation rate, surface heat budget, and precipitation reveals a larger negative effect of a dry soil moisture bias as compared to a positive effect of moist bias. Moisture supply by surface evapotranspiration is nonlinearly increasing with soil moisture. In other words, the magnitude of an increase in evaporation due to a positive soil moisture bias is less than the decrease caused by a negative soil moisture bias. Since this mechanism changes available, atmospheric moisture it thus influences average precipitation. Barthlott and Kalthoff (2011) support the effect of this nonlinear behavior over Central Europe simulating precipitation with gradually increased initial soil moisture from $-50\,\%$ to $50\,\%$ in steps of $5\,\%$ for a single case study. Similar to our study, their study did not show a further increase in precipitation for positive soil moisture biases.

This thesis extends current literature by including several real-case studies differing in their synoptic conditions. The focus on the influence of initial soil moisture perturbations during the different synoptic conditions, on average, revealed a more considerable impact of soil perturbations during weak synoptic forcing. Thus, near-surface variability caused by differential surface heating is more prominent during weak synoptic forcing. In contrast, moderate synoptic forcing is often accompanied by increased cloud coverage, which reduces surface heat fluxes. Furthermore, increased mid-tropospheric background wind increases the importance of atmospheric advection. Those two characteristics of intensified synoptic control reduce the effect of near-surface variability during moderate synoptic forcing.

Combined effects of initial soil perturbations and orographic differences in the German domain reflect the relative importance of the underlying terrain concerning the regime-dependent SMP coupling. Spatial variability over the fairly flat northern subdomain showed less sensitive to the synoptic regime. While spatial variability is more prominent for weak synoptic conditions, the absence of orographic triggers increases the importance of alternative triggering mechanisms, like gradients in surface heating. Because of the greater presence of local triggers over the orographically structured southern subdomain, synoptic sensitivity is more pronounced. While spatial variability is high for weak synoptic forcing, orographic triggers suppress the influence of soil moisture perturbations during moderate synoptic forcing.

RQ-2: What is the combined and regime dependent impact of soil moisture bias and heterogeneity on different spatial scales on the precipitation forecast?

> Despite all atmospheric and orographic complexities involved in the real-case scenarios, we found a locally negative SMP coupling. Interactions between thermally induced circulation cells near soil moisture gradients and the background wind lead to a preferred triggering of convection persistent updraft regions over dry patches which is most prominent for heterogeneity length-scales in the range of 40 km to 80 km. Despite the sharp heterogeneities, domain-averaged precipitation is more dependent on large-scale soil moisture anomalies, which is why precipitation positively correlates with domain-averaged soil moisture.

Introducing additional heterogeneities with well-defined length-scales and sharp gradients allows investigating the collective impact of a uniform bias and heterogeneity in initial soil moisture on convection initiation in real-case scenarios. Chessboard patterns with different patch sizes are superposed with a uniform bias of $\pm 25\,\%$ to create initial conditions with fixed heterogeneity length-scales. Despite the presence of sharp gradients on soil moisture, the domain-averaged effect of bias in soil moisture remains similar to the simple bias experiments from the previous set of experiments. The resulting positive domain-averaged SMP coupling shows that large-scale precipitation is more dependent on large-scale soil moisture perturbations.

In contrast to that, there is a negative local SMP coupling. This means that more precipitation occurs over dry patches. Differential heating over adjacent moist and dry tiles invoke differences in surface temperature and pressure. As a consequence, divergence over moist and convergence over dry patches accompanied with thermally driven circulation cells near the soil moisture gradients evolve. This dynamic mechanism results in higher Liquid Water Path (LWP), an earlier transition from shallow to deep convection and increased precipitation over dry patches. This result is in line with findings from Rieck et al. (2014) evaluating high-resolution simulations in a highly idealized domain.

The background wind strongly modulates circulation cells induced by differential surface heating. Superposition of the background wind with opposing convergent stream of the dry patches close to the adjacent moist patch leads to the intensification of thermally induced circulation cells. As a result, deep convection is preferentially triggered in the vicinity of those persistent updrafts. This mechanism depends on two main factors. First, the intensity of the circulation cells is most prominent for patch sizes between 40 km and 80 km. The predetermination of the region of preferential initiation of convection most efficiently reduces day-to-day variability in accumulated precipitation in this range of heterogeneity length-scales. Second, the intensity of the background wind plays an important role and, by that, the synoptic regime. Synoptic differences manifest, among others, in amplification of the mid-tropospheric background wind and reduced surface heat flux. Therefore, thermodynamic differences in the lower troposphere remain present but are less pronounced for moderate synoptic forcing. The weakened circulation cells show a smaller vertical extent and thus provide less potential for convection triggering. With increasing synoptic forcing atmospheric advection is gaining importance. Thus, the SMP coupling is reduced for moderate synoptic forcing. Lee et al. (2019) recently also found a vanishing effect of thermally induced circulation cells for increasing background wind while examining large-eddy simulations with horizontally homogeneous atmospheric initial conditions.

RQ-3: What is the relative impact of soil moisture, stochastic Boundary-Layer, and aerosol perturbations on convective precipitation considering different synoptic regimes?

> While domain-averaged precipitation hardly changes, the perturbed-parameter ensembles produce a substantial, non-negligible amount of variability. In contrast to PSP and CCN, soil moisture perturbations show the largest dependence on the synoptic regime and generate most variability during the initiation phase of convective precipitation. Thus, soil moisture perturbations show their largest impact during weak synoptic conditions.

After describing relevant mechanisms defining the SMP coupling in real-case scenarios using a state-of-the-art, convection-permitting weather model, question RQ-3 aims at comparing more realistic initial soil moisture perturbations building upon previous experiments with two other specific sources of uncertainty influencing convection triggering and cloud formation. Furthermore, Soil, stochastic BL (PSP) and cloud condensation nuclei (CCN) perturbations are compared with two benchmark simulations including the operational COSMO-DE-EPS (EPS) and an ensemble initialized with white noise perturbations of temperature (WNoise) to assess their relevance.

Thus, the perturbations hardly change general precipitation amounts but still show a dependence on the synoptic regime with slightly increased 12-hourly accumulated precipitation during weak synoptic forcing. Regime-dependence, however, is more prominent in the ensemble (S_n) and spatial (FSS) variability. All perturbed-parameter ensembles show variability larger than the WNoise ensemble supporting that differences in forecasts rely on physical reasons based on the respective parameter. Compared to the operational EPS, all three perturbed-parameter ensembles show a substantial, non-negligible amount of variability.

Two dominant features contrast the soil moisture perturbations from the remaining. First, heterogeneous soil moisture perturbations predominantly affect the initiation process of convection by dynamical modifications of the lower troposphere due to differential heating. Therefore, it shows a steep increase in the ensemble and spatial spread during the initiation phase of convection (i.e. from 09 UTC to 12 UTC for the HIW period). Second, it shows the most pronounced regime dependence with higher variability during weak and smaller variability during moderate synoptic forcing. Those features distinguish soil perturbations from the other perturbation methods applied in this thesis.

Aside from the regime-dependence, the influence of different perturbations also alters with the underlying terrain. Since CCN perturbations mainly affect cloud formation, resulting variability is hardly sensitive to orographic influences. PSP also shows only small regime dependence with slightly higher variability for weak synoptic forcing over the southern subdomain. Over the northern part of Germany, however, differences in the impact dependent on the synoptic regime are larger and show a slightly increased influence during moderate synoptic forcing. While soil heterogeneity generates variability insensitive to the underlying terrain during weakly forcing conditions, regional differences appear during moderate synoptic forcing. In the absence of orographic triggers over the flat, northern subdomain, the influence of soil perturbations is more substantial as compared to the southern part where orographic mechanisms suppress the effect of soil moisture perturbations.

Outlook and implications for future research

The research presented in this thesis highlights some unique characteristics of heterogeneous initial soil moisture perturbations that other considered perturbation methods do not show. Regarding deep convection on a daily timescale, soil moisture perturbations alter the location of convection initiation due to dynamical modifications of the lower troposphere induced by differential surface heating. We hypothesize that this reduces the possible locations where convection initiation can occur. In that respect, accurate representation of soil moisture conditions can act as a source of predictability. This is especially true in the absence of other triggering mechanisms, such as orography, or large-scale lifting, and when the synoptic forcing is weak. Therefore, such perturbations mostly affect situations and regions where local, small-scale variability is shown to be missing in operational, convection-permitting forecasting systems (e.g., Kühnlein et al., 2014). The effect, however, is strongly dependent on the heterogeneity length-scale or the spatial anomalies.

Results in this thesis are achieved exploiting COSMO simulations with a grid spacing of 2.8 km. This resolution permits the representation of convection but is coarse in comparison with the small-scale processes driven by soil moisture-induced differential surface heating. Thus, the results presented in this thesis are potentially dependent on the model resolution. Therefore, simulations are repeated for two case studies with finer model resolution (i.e. 0.5 km) to investigate the sensitivity of the results to the model resolution. The results presented in Appendix A show a slightly faster response of precipitation on initial soil moisture bias across all analyzed spatial scales. Differences in precipitation timing, however, are below an hour. Furthermore, experiments simulating two of the initial chessboard patterns (i.e. 42 km and 56 km patch sizes) hint on a shift of the spatial range of resonant scales towards smaller patch sizes. However, as the high-resolution simulations are computationally very expensive, the results are based on a small number of experiments and case studies, which hampers conclusiveness. Furthermore, results are hard to assign to the resolution as a more sophisticated turbulence scheme was applied in the high-resolution simulations. This means that it is not clear whether differences arise from an improved representation of dynamical processes due to the finer grid spacing, or from the better turbulence scheme. Hints provided by those preliminary results, however, support further investigations.

Another limitation of this thesis is the number of real-case studies, which had to be limited to 17 due to computational constraints. Even though this number and characteristics of real-case studies in this study are, compared to literature, exceptional, more cases, or a longer period including more differently forced precipitation events would be beneficial for firm conclusions. Nonetheless, we believe that the classification by weather situation and the ensuing regime dependent averaging reflects a general atmospheric behavior of SMP coupling during different synoptic control and thus provides a robust basis for future research. Furthermore, the perturbed-parameter ensembles do not adequately sample the probability distribution of atmospheric states and do not represent an ensemble forecast in a statistical sense. However, perturbations applied in this thesis account for uncertainty in processes relevant to the formation of convective precipitation in a physically meaningful way. Therefore, we consider the results gathered in this thesis as encouraging for future research dealing with the different perturbation approaches in conjunction with the principal sources of uncertainty being initial and lateral boundary condition uncertainty, as well as model error as implemented in modern EPS.

In addition to that, this thesis only considers experiments applying the exclusive perturbation of one parameter. Beyond that, it would be beneficial to investigate the combined influence of various perturbation methods as different processes might compensate or enhance each other. Highly idealized LES with horizontally homogeneous initial conditions performed by Jiang and Feingold (2006) emphasize the importance of coupled surface and aerosol-radiative processes. They find the coupling between aerosol-radiative effects and surface heat fluxes to be an important mechanism determining the intensity and duration of deep convection. Grant and van den Heever (2014) simulated tropical convection triggered by sea-breeze circulations with convection-permitting resolution in an idealized setup with horizontally homogeneous atmospheric initial conditions. They report that strong perturbations of CCN or soil moisture individually strongly influence convective precipitation. In the case of collective perturbations, however, nonlinear interactions lead to more affect convective rainfall more effective when relative perturbations are moderate. Those studies demonstrate the importance of collective effects coupling aerosol and soil moisture. Also, note that our choice of perturbed-parameters does not imply their exclusive importance. We picked three major sources of uncertainty concerning deep moist convection, however other parameters are also important and might be considered in future research.

Based on the findings of this thesis, it is likely that systematic initial condition perturbations of the surface state offer the opportunity to increase ensemble spread of prognostic variables, such as temperature, humidity, or precipitation. Potential perturbation parameters, such as surface roughness, leaf area index, or soil moisture, influence the partitioning of surface heat fluxes. Those perturbations evoke modifications of the low-level dynamics based on differential surface heating. Inert processes acting on, for example, soil moisture require solar radiation to unfold their impact on the lower troposphere's dynamic. Thus, those perturbations are expected to show the largest impact during the initiation phase of convection around noon when choosing perturbations with a spatial correlation in the order of a few 10 km. Since those inert physical processes are not likely to be dependent on the model configuration, we expect this to hold for different model settings, as well. Since those processes mainly influence the location of convection, the increased spread in convective precipitation can only be verified using spatial techniques as an unbiased perturbation predominantly reshuffles the location of convection initiation. In contrast to that, the orographic dependency shown in this thesis might, according to Appendix A, be sensitive to the model configuration.

Concerning future applications, Bauer et al. (2015) anticipates beneficial effects of EPSs featuring aerosol and surface uncertainty. This further encourages future investigation of the influence of the soil moisture initial state on the quality of weather forecasting. First studies implementing satellite-based soil moisture measurements in data assimilation found a beneficial impact on near-surface variables (e.g. 2 m temperature) and precipitation over Central United States (Lin et al., 2017) and Eurasia (Draper and Reichle, 2019). This is why the Japanese Meteorological Agency (JMA) operationally assimilates satellite soil moisture observations in their Limited Area Model since January 2017 (Ikuta, 2017). Since we showed in this thesis that the state of the surface is able to affect convection initiation, its accurate representation is a crucial precondition for a precise forecast of convection.

Finally, let us take a look into the future. Since regions of strong coupling between soil moisture and precipitation are most significantly confined to transitional regions between humid and arid climates (e.g., Koster et al., 2004; Taylor et al., 2011), climate change is very likely to alter the susceptibility to soil moisture-precipitation interactions. Exploiting more than 60 years of reanalysis data, Gu et al. (2019) encountered a significant drying trend with the largest gradients over Central Europe, Sahel zone, as well as Northern and Eastern Asia. This trend is expected to continue throughout the present century (Dirmeyer et al., 2012; Gu et al., 2019). Furthermore, Dirmeyer et al. (2012) reports increased the probability of extreme precipitation anomalies in most regions of the globe, which increases the danger of flash-floods and dryness. As many studies, including ours, showed a pronounced positive impact of large-scale soil moisture anomalies on large-scale precipitation, it can be expected that SMP coupling will be increasingly important. Moreover, our study showed a noticeable impact of local soil moisture anomalies on convective precipitation. As preceding precipitation, especially in transitional climate zones, leads to pronounced small-scale soil moisture anomalies, local SMP coupling will gain importance, as well. This shows that in-depth knowledge about mechanisms connecting soil processes with the atmosphere combined with regional effects over Central Europe is of high importance for today's forecast of convective precipitation and prepares for future challenges in a changing climate.

A. Soil moisture-precipitation coupling with finer model resolution

In this thesis, we intentionally use the operational model resolution of 2.8 km for the COSMO simulation to remain as close as possible to arising problems in everyday weather forecasting, and to identify dominant, resolved processes being relevant for the operational service. This resolution permits the representation of convection but is coarse in comparison with the small-scale processes driven by soil moisture induced differential surface heating. Thus, the results presented in this thesis are potentially dependent on the model resolution. Furthermore, by performing several simulations with chessboard-like initial soil moisture conditions with varying patch sizes, we found that soil moisture perturbations with a heterogeneity length-scale between 40 km and 80 km (Section 3.2). Studies investigating the scale-dependent SMP coupling with higher model resolution and horizontally homogeneous atmospheric initial conditions, however, report about smaller resonant scales in the order of a few tens of kilometers. Thus, this indicates that the spatial scales found in this thesis are partly dependent on the comparably coarse model resolution. Therefore, the following chapter repeats some experiments with a finer model resolution to assess the influence of model resolution on the SMP coupling. Section A.1 describes the model configuration for the 500 m COSMO simulations, as well as reasons for necessary adaptations. A wavelet-based method to quantify the influence of soil moisture perturbations on different spatial scales is introduced in Section A.2. The influence of increased model resolution on experiments initialized with a moist and dry soil moisture bias, as well as two different initial chessboard patterns are shown in the results Section A.3 before the chapter closes with a summary (Section A.4). The results presented in this appendix, however, are difficult to interpret as a more sophisticated turbulence scheme was used in addition to the finer model resolution.

A.1. High resolution COSMO simulations

To investigate the influence of model grid spacing on the soil moisture-precipitation interaction, we repeated some simulations on a finer grid of 500 m for a subset of the experiments. Those high-resolution simulations applying a similar model configuration as used in Schneider et al. (2018) were conducted with support from colleagues

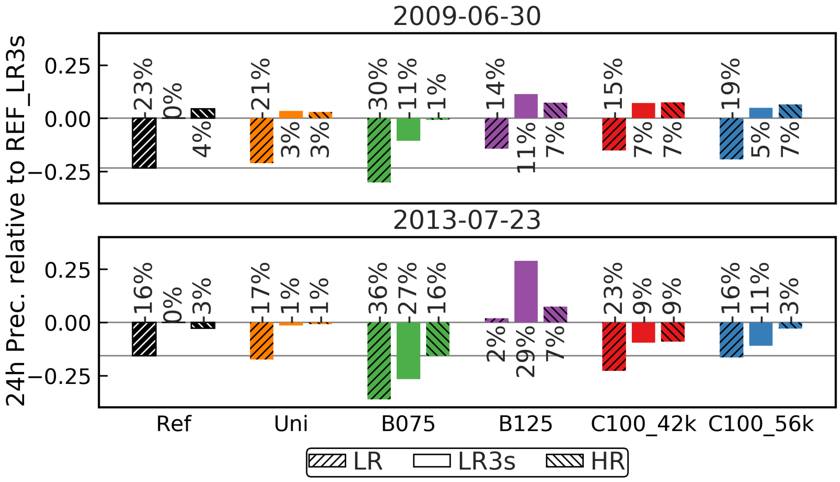

Figure A.1.: Domain accumulated daily precipitation for two different weakly forced case studies illustrating the impact of the model time step. Values are shown for the unperturbed reference simulation, as well as simulations with altered initial soil moisture conditions, such as the uniform control (Uni), two bias simulations with ±25 % initial soil moisture, and 42 km and 56 km chessboard simulations. The leftmost bar indicates simulations with the operationally used 25 s times step, while the central bar indicates the low-resolution simulation with 3 s times step and the rightmost bar shows the high-resolution simulation.

at Karlsruhe Institute of Technology (KIT). To enable a consistent dataset, high-resolution (i.e. 500 m) simulations are configured as similar as possible ro the low-resolution (i.e. 2.8 km) simulations. The high-resolution simulations are initiated at 00 UTC and driven by hourly initial and boundary conditions delivered from the low-resolution simulations (i.e. 2.8 km). The increase in model resolution requires a reduction of the domain to an approximate size of 750 km by 650 km (1510 × 1300 horizontal grid cells) covering the *German subdomain* in Figure 2.1. Furthermore, the number of vertical levels is increased to 80. In contrast to the low-resolution simulations, shallow convection is fully resolved, and turbulence is parameterized using a 3-D closure scheme (Doms et al., 2011). For the reason of numerical stability, the model time step was reduced from 25 s to 3 s. The high sensitivity of the model results on the model time step (Barrett et al., 2019) required the repetition of the respective low-resolution simulations with a reduced model time step, as well. Figure A.1 impressively shows the impact of the model time step in our experiments. While the high-resolution experiments reveal a deviation from the experiments applying the operationally used 25 s model time step of 15 to 25 %, adjusting the internal model time step of the low-resolution simulations to 3 s substantially reduces the deviations. This is an important measure to allow for a comparison of the different model resolutions.

All experiments performed for the resolution comparison are constructed similarly to the corresponding experiments listed in Section 2.3.1. The collection of experiments contains an unperturbed reference simulation (REF), an uniform control simulation (UNI), simulations with an initial soil moisture bias of ±25 % (B075; B125), as well as chess board experiments with tile sizes of 42 km (C100_42k) and 56 km (C100_56k). The nomenclature of the experiments is similar to Table 2.1 but extended by suffix (*_LR / *_HR) differentiating the high- and low-resolution experiments from each other and the simulations conducted using a model time-step of 25 s. Those experiments are performed for two case studies marked with * in Table 2.2 (i.e. 30 June 2009 and 23 July 2013).

A.2. Wavelet based, scale-decomposition validation method

Neighborhood verification methods for precipitation fields, such as the Fractions Skill Score (FSS) presented in Section 2.7, quantify the spatial agreement between a reference and a forecast at a particular spatial scale. This spatial scale resembles a smoothing scale, which means that all smaller scales are also considered. This feature, however, is not optimal when comparing simulations with different spatial resolutions as the number of resolved scales for a particular analyzed scale changes with model resolution. For that purpose, a scale separation method, such as the Intensity-Scale Score (ISS), is advantageous (Casati et al., 2004; Mittermaier, 2006). Similar to the FSS, the first step is to produce a binary field by applying a precipitation threshold. Afterwards, scale decomposition is performed using the 2D Haar wavelet method. The Haar wavelet is a widely used, robust wavelet optimally resembling the step functions of the binary field. The inverse wavelet decomposition is then applied individually to every single wavelet scale to obtain the scale components of the binary field. Precipitation features are thus decomposed in several spatial scales. The skill assessment then considers differences in this reconstructed field between a reference simulation and an experiment. We, however, use this approach to quantify the forecasting bias at different spatial scales. For that purpose, the average of the squared reconstructed binary fields at scale l applying a threshold u are calculated. Those values are then aggregated to a relative energy difference

$$En_{diff} = \frac{En_{u,l}(F) - En_{u,l}(O)}{En_{u,l}(F) + En_{u,l}(O)} \tag{A.1}$$

between a forecast (F, in our case an experiment) and an observation (O, in our case a reference simulation) (Casati, 2010). The resulting value ranges between -1 and 1, whereas negative values describe an underforecasting and positive values mark an overforecasting of precipitation at a particular threshold and scale (Gilleland et al., 2009; Casati, 2010). Please refer to Casati et al. (2004) and Casati (2010) for further details about the method.

A.3. Influence of model resolution on soil moisture atmosphere interaction

We first analyze the spatial distribution of daily accumulated precipitation for the unperturbed reference simulations (REF) to visually assess the spatial agreement of the two model resolutions in Figure A.2. While the general regions with precipitation remain roughly unchanged when increasing model resolution, high-resolution simulations show a broader and smoother distribution of precipitation. This is especially visible on 30 June 2009 over Northern Germany, where more grid points with precipitation are present in the 500-m simulations than in the 2.8-km simulations. This results in an increase in precipitating grid cells by 10 % on 30 June 2009 (5 % on 23 July 2013). The change in domain accumulated daily precipitation, however, is below 5 % for both case studies (Fig. A.1). Removing heterogeneity in relative soil moisture in the Uni simulations even reduces the differences between the experiments and REF_LR. Even though the onset of afternoon precipitation in the HR simulations is slightly earlier (later) on 30 June 2009 (23 July 2013), timing is generally very similar (Fig. A.3). Thus, domain-averaged, the combined impact of model resolution and altered turbulence scheme is small for the reference and control simulations.

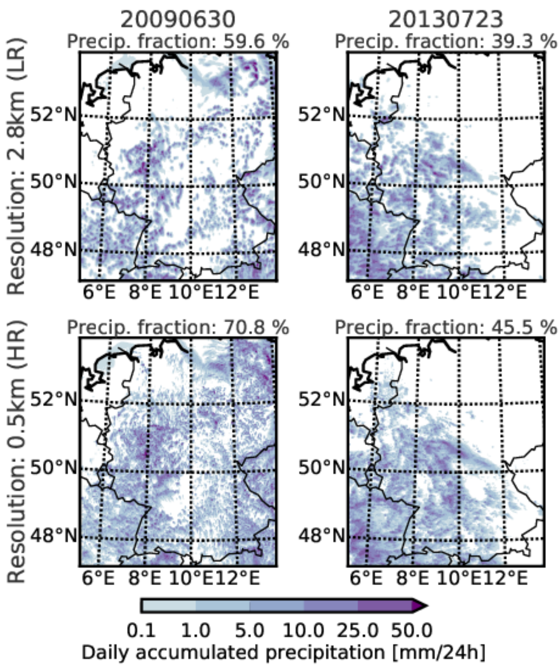

Figure A.2.: Daily accumulated precipitation for the low (upper) and high (lower) resolution unperturbed reference simulations (REF) on 30 June 2009 (left) and 23 July 2013 (right).

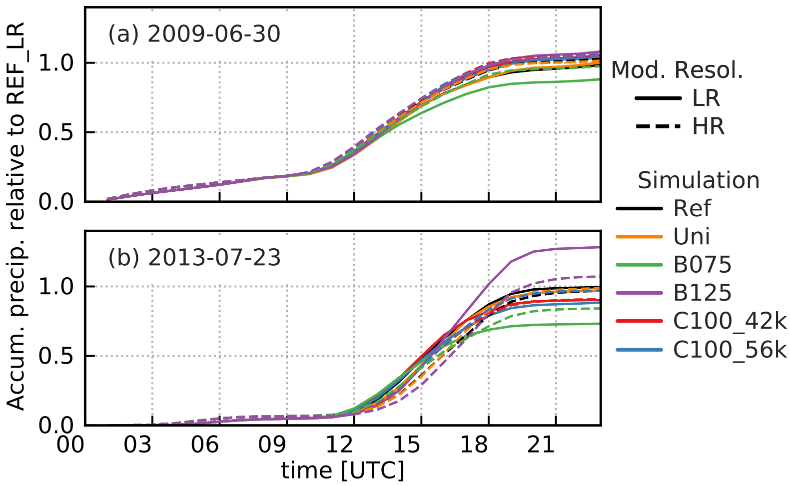

Figure A.3.: Time series of domain averaged, accumulated precipitation for an unperturbed reference simulation (REF), uniform initial soil moisture (Uni), dry and moist initial soil moisture bias, and chessboard experiments with 42 km (C100_42k) and 56 km (C100_56k) patch sizes. Evaluations are shown for low (LH, solid) and high (HR, dashed) model resolution on 30 June 2009 (a) and 23 July 2013 (b).

A.3.1. Bias Experiments (B075, B125)

Considering the bias experiments, differences arise between the model resolutions and the different case studies. In both case studies, the sign of SMP coupling is equal and describes an increase in daily precipitation for moist and a decrease for dry bias experiments. The magnitude, however, is very different in two ways. On the one hand, the impact of initial soil moisture bias is larger for the low-resolution simulations. The general impact, on the other hand, is larger for the 2013 case ($\pm\mathcal{O}30\,\%$) as compared to 30 June 2009 ($\pm\mathcal{O}10\,\%$) (Figs. A.3 and A.3). This difference can be explained by differences in the thermodynamic structure as displayed in Figure A.4 (see also Section 2.8). Since the large low-level humidity index (HI_{low}) on 23 June hints on very dry conditions, precipitation is very sensitive to available soil moisture. Furthermore, large mid-level instability (Convective Triggering Potential (CTP)) favors strong convection. Both these metrics decrease throughout the day, which hints on low-level moistening by convective precipitation. The 2009 case, instead, shows small values of HI_{low} and CTP in comparison to the 2013 case. The fact that both values increase during the day hints on atmospheric instability being too small to efficiently trigger convection considering the prevailing moisture and radiative conditions.

The relative difference in domain-averaged, wavelet-based energy (see Eqn. A.1) relative to the unperturbed reference (REF) is shown in Figure A.5. Negative values qualitatively resemble a negative, while positive values show a positive bias in precipitation for a certain precipitation threshold at the particular scale. The general response of spatial precipitation is most pronounced for the dry bias experiments on 23 July 2013 (Fig. A.5e,g) showing positive precipitation bias throughout all

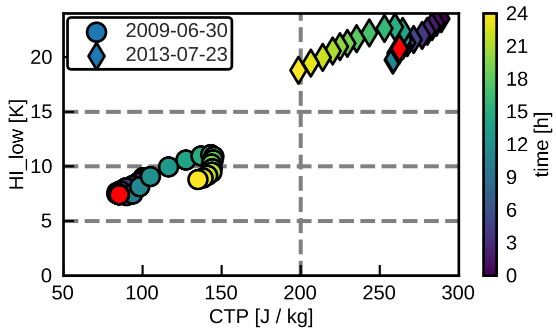

Figure A.4.: Time series (colors) of domain averaged CTP and HI_{low} evaluated for the unperturbed reference simulation (REF) of 30 June 2009 (circles) and 23 July 2013 (diamonds). Early morning conditions are marked in red.

scales during the beginning of afternoon precipitation (i.e. from 9 UTC to 15 UTC) and a negative bias during the evening (i.e. from 15 UTC to 21 UTC) for small precipitation thresholds (i.e. 1.0 mm/h and 4.0 mm/h). While the signs are switched for the moist bias simulations (i.e. positive bias during the early afternoon and negative bias during the evening), the magnitude of the precipitation bias still increases with spatial scale for small precipitation thresholds. Thus, a negative bias in initial soil moisture leads to an earlier increase in precipitation but also an earlier decay in the evening. The opposite is valid for the effect of positively biased in initial soil moisture conditions on hourly precipitation. This temporal dipole structure, however, is, especially for the 2013 case, more pronounced for increased model resolution. Thus increased model resolution, as well as a more accurate description of BL turbulence, leads to a faster response to changes in soil moisture. Differences in domain-accumulated precipitation (Fig. A.1) are unlikely to rely on differences in small precipitation values entirely. Considering higher precipitation thresholds (i.e. 16.0 mm/h, 32.0 mm/h) reveals large discrepancies between the model resolutions. According to that, the response is more prominent for the medium precipitation threshold (16.0 mm/h) for the high-resolution simulations. In contrast, the effect on medium precipitation is more constrained to larger spatial scales, whereas intense precipitation is affected on all spatial scales in the low-resolution simulations. The latter is more dominant for low model resolution and explains the substantial differences in domain-accumulated precipitation. This contrast leads to a reduced impact of initial soil moisture bias with increased model resolution. The same is valid for 30 June 2009 (Fig. A.5a-d) however, the magnitude of the differences is smaller due to reduced interaction between soil and atmosphere as already described using the CTP-HI_{low} framework.

A.3.2. Chessboard Experiments (C100_42k, C100_56k)

The domain-averaged, daily impact of chessboard patterns in initial soil moisture is small in comparison with the influence of initial soil moisture bias. This is in line with findings from Section 3.2 supporting that the domain-averaged precipitation

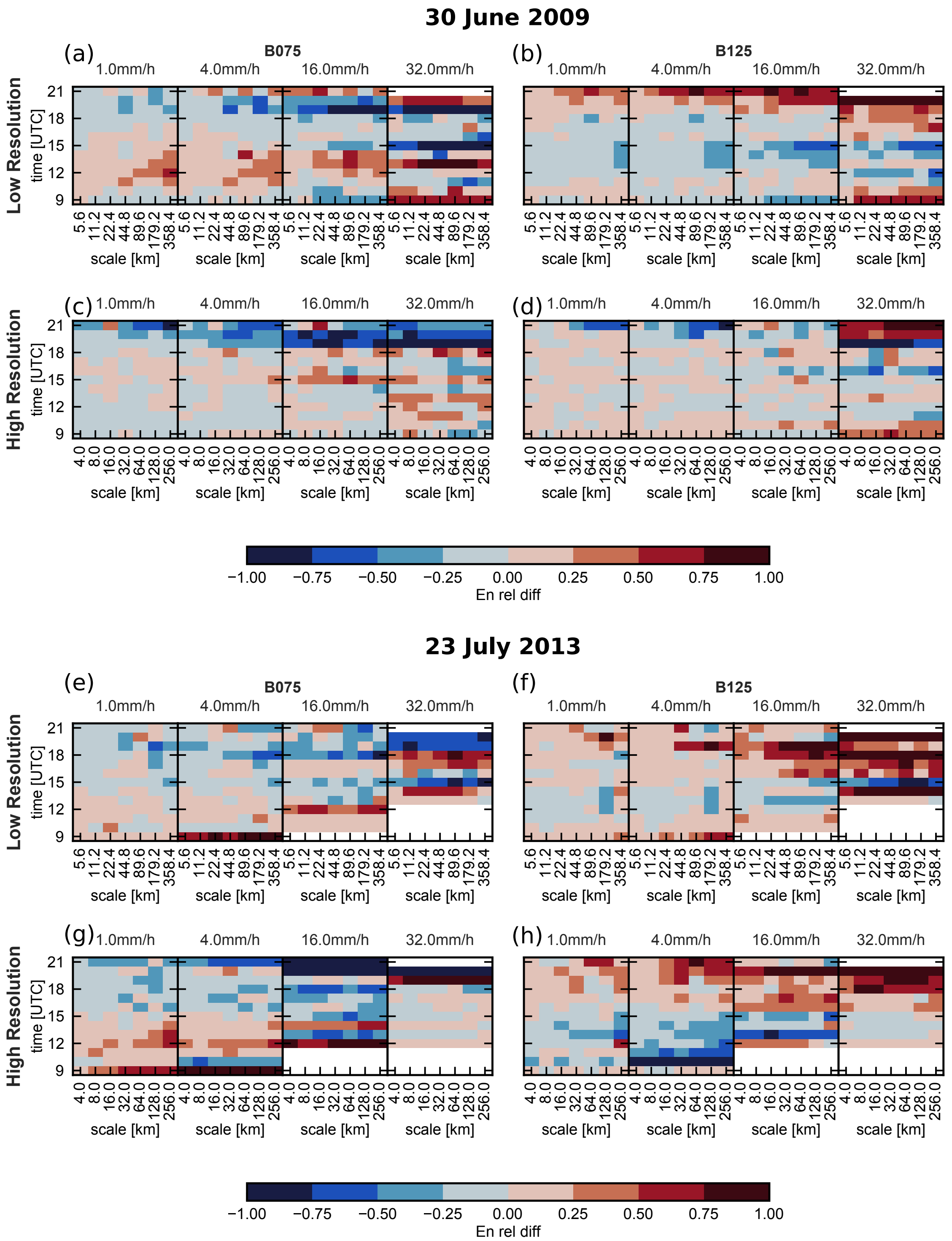

Figure A.5.: Relative difference in domain averaged energy (see Eqn. A.1) between dry (B075, left column) and moist (B125, right column) bias experiment evaluated for different precipitation thresholds (subplots, i.e. 1.0 mm/h, 4.0 mm/h, 16.0 mm/h, 32.0 mm/h) and scales (x-axis) from 9 UTC to 21 UTC (y-axis). Evaluations are performed for the 30 June 2009 (a-d) and 23 July 2013 (e-f). The first row on each day depicts the low-resolution simulations while the high-resolution simulations are in the second row. Negative values qualitatively resemble a negative (blueish), while positive (reddish) values show a positive bias in precipitation compared to the unperturbed reference (REF) for a certain precipitation threshold at the particular scale.

generally remains similar if domain-averaged initial soil moisture remains the same. Differences, however, arise from soil moisture heterogeneity, altering the intensity and location of convective precipitation by thermally induced, secondary circulation cells induced by differential surface heating. In Section 3.2, we elaborated on the hypothesis that this process is most efficient for heterogeneity length-scales ranging from 50 km to 80 km. This scale range, however, might be dependent on the model resolution. To assess the influence of model resolution on this mechanism, we repeated two different chessboard patterns (i.e. C100_42k and C100_56k) with higher model resolution. Note that the chessboard patterns are equally set up, but simulations are realized with the different model resolutions.

Evaluating the relative difference in wavelet-based energy (Fig. A.6) reveals earlier intensification for both patch sizes (reddish colors) in the early afternoon and an underestimation of precipitation in the evening (blueish colors). Differences in precipitation are most prominent for high precipitation thresholds. This means that heterogeneous soil moisture perturbations predominantly perturb the triggering process. Furthermore, single convective cells are intensified but show shorter duration, which is why differences increase in magnitude for higher precipitation thresholds. Apart from higher variability on 23 July 2013 (Figs. A.6 e-h), general differences between the two case studies are small.

In Section 3.2, we found that differential surface heating results in compensating thermally induced circulations near the borders of the patches. To assess the influence of model resolution on these circulation cells we visualized mean vertical cross-sections of S_e, and wind (cf. Fig. 3.12, 3.14 and 3.15 in Section 3.2 for further detail about the averaging method). The mean cross-sections are shown in Figure A.7 are constructed by meridionally averaging the vertical distribution of different quantities and taking the difference between the C100_42k (C100_56k) experiment and the control experiment UNI on 30 June 2009 and 23 July 2013 at 12 UTC in Figures A.7 and A.8. The general structure of the thermally induced circulation cells with subsidence over moist and ascent over dry patches, as well as the gradients in S_e differences, are captured by both model resolutions but are amplified in the high-resolution simulations. The regions of amplified q_c are similar for both resolutions (especially the highest (black) contour). Moisture flux convergence shows a less smooth distribution due to higher model resolution. Especially the 56 km patch on 30 June 2009 (comparing Figs. A.7d,h) shows a very noisy structure of low-level $\overline{MFC}$ for high model resolution caused by many small scale downdrafts over the wet patch.

Additional to the differences in CTP and HI_{low} leading to higher evaporative demand for 23 July 2013, the 2013 case shows higher mid-tropospheric wind speed (see Table 2.2). This leads, relative to the 2009 case in Figure A.7, to a drastically amplified updraft region on the west side of the moist patch on 23 July 2013 (Fig. A.8). The strong wind hampers differences between moist and dry patches in $\overline{MFC}$ for the 56 km patch (Fig. A.8d). While this is not the case for the smaller patch size (Fig. A.8b), differences in S_e almost vanish as S_e deficit from the upwind dry patch is advected over the moist patch (Fig. A.8a). Increasing model resolution

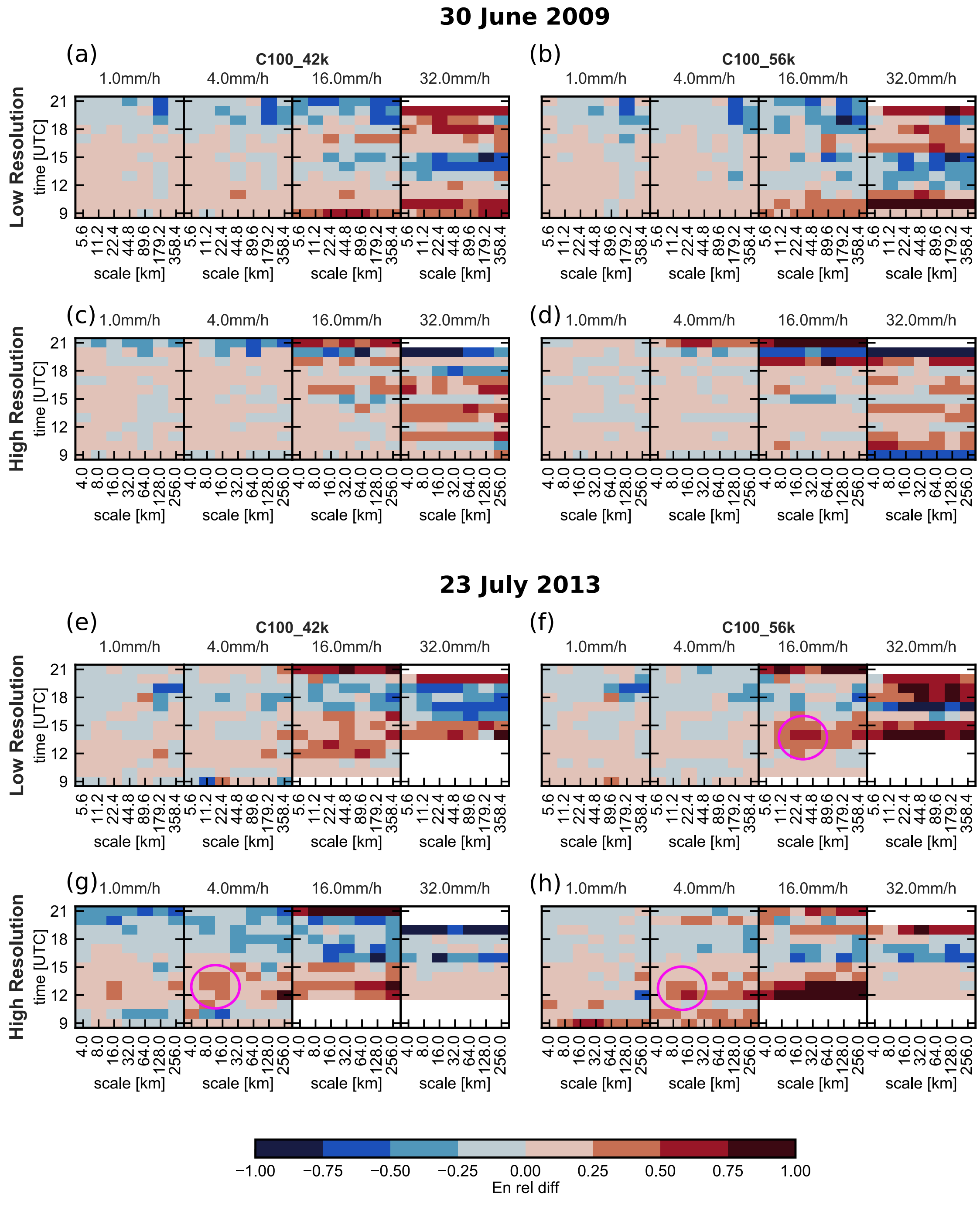

Figure A.6.: Same as Figure A.5, but for C100_042k (left column) and C100_056k (right column) experiments relative to an uniform control simulation (Uni). Purple circles in f,g,h mark interesting regions.

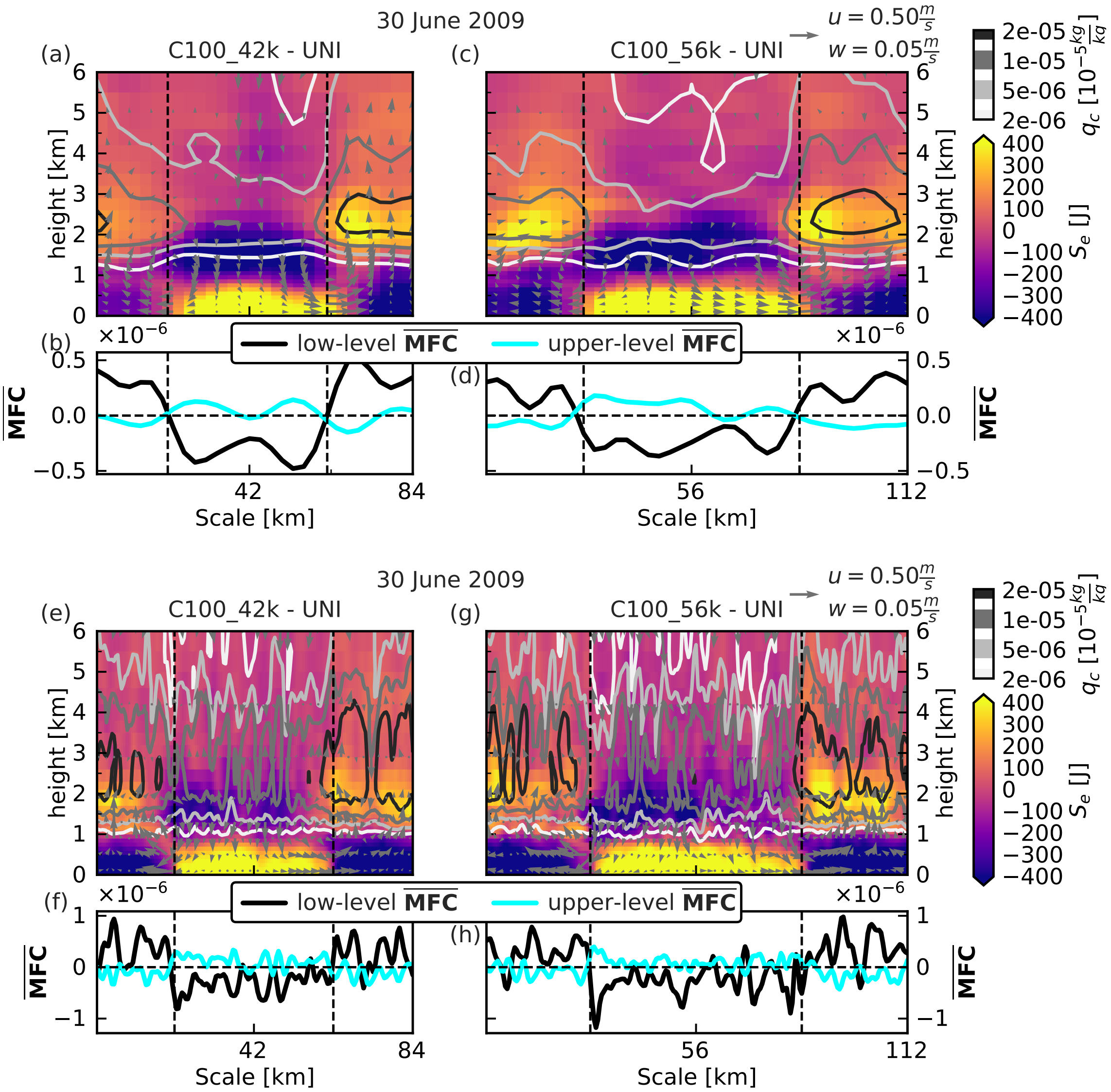

Figure A.7.: Mean meridionally averaged vertical cross-sections with the moist patch in the center and half of the adjacent dry patches (according to the zonally shifted yellow box in Figure 2.2(f)) displaying the difference of Moist Static Energy (S_e) between the control simulation (UNI) and the C100_42k (a,e) and C100_56k (c,g) experiments evaluated on 30 June 2009 at 12 UTC. Yellow colors show an excess and purple colors a deficit in S_e compared to UNI. The arrows show the differences in the u and $10w$ components of the wind. The white dotted line indicates the average BL height. The contour lines indicate specific cloud water content (q_c). Panels (b,f) and (d,h) show vertically averaged difference in Moisture Flux Convergence below 1000 m above ground (low-level $\overline{MFC}$) and between 1000 m and 2000 m (upper-level $\overline{MFC}$). Low-resolution simulations (a-d) are depicted in the upper, whereas high-resolution simulations (e-h) are shown in the lower half of the graphic. The dashed vertical lines in all panels indicate the borders between the patches.

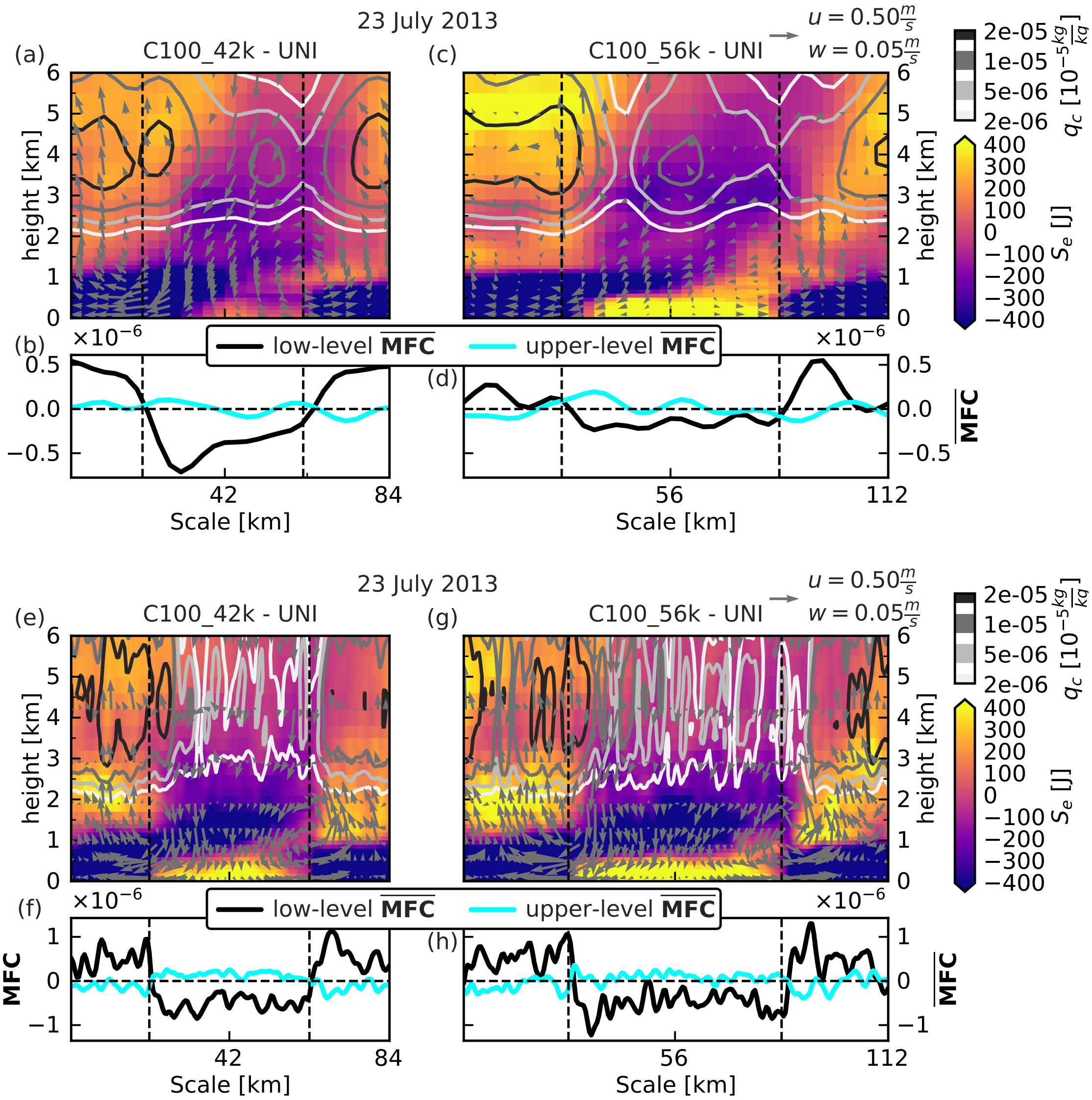

Figure A.8.: Same as Figure A.7 but evaluated for 23 July 2013.

for this case improves the representation of the dipole structure in S_e, especially for the smaller patch size (Fig. A.8e,g). Furthermore, increased wind speeds lead to a strongly amplified updraft on the windward side of the wet patch and a pronounced maximum in specific cloud water content (q_c). For this case, the coarser model resolution and less accurate turbulence scheme are not able to develop those pronounced patterns.

The improved response of the circulation cells to surface heterogeneity is visible in the relative difference of wavelet energy in Figure A.6 e-h. The C100_56k experiment shows a weak local maximum between 12 and 15 UTC for spatial scales ranging from 11.2 km to 44.2 km (i.e. approximately the range of the heterogeneity length scale) as marked by the purple circle in Figure A.6f. The smaller patch size (C100_42; Fig. A.6e), however, does not show such a local maximum but an increase in precipitation throughout all spatial scales during this time. Applying the same metric to the high-resolution again shows the improved representation of precipitation influenced by soil heterogeneity (Figs. A.6g,h). Both patch sizes show pronounced local maxima in precipitation scales ranging from 8.0 km to 16.0 km during the initiation phase (from 12 UTC to 15 UTC; marked by the purple circles).

A.4. Discussion and summary

While, compared to the operational model resolution, increased model resolution in principle produces similar precipitating regions, precipitation is wider distributed (by up to 10 %) and peak precipitation is slightly reduced. This results in a neutral, or a slightly reduced amount of daily, domain-averaged impact of soil moisture perturbations for higher model resolution. Especially the bias simulations show substantial differences in the influence on domain-averaged precipitation. Due to the improved representation of dynamic processes on the lower troposphere with finer grid spacing, the model reacts faster on a soil moisture bias. This leads to a quicker increase (decrease) in precipitation for a dry (moist) bias during the early afternoon but also a much faster decrease (increase) in the evening. Differences in the timing of precipitation, however, is smaller than an hour. The net effect, however, is a slight reduction of the domain-averaged influence of initial soil moisture bias for increased model resolution.

The improved representation of lower tropospheric dynamics and thermodynamics also improves the representation of thermally induced circulation cells, especially for conditions with strong mid-tropospheric background wind. Thus, a more pronounced influence of chessboard-like initial soil moisture conditions is visible. This is especially true for the smaller patch size (i.e. C100_42k). While this hints on a shift of spatial scales optimally determining the initiation of precipitation to the amplified updraft regions near the upwind side of moist patches as found in Section 3.2 towards smaller scales with an increasing model resolution, further experiments with smaller patch sizes are required to further elaborate on this.

Note that it is hard to distinguish to what extent the more sophisticated turbulence scheme used for the high-resolution simulations influences the findings. This means that it is not clear whether differences arise from an improved representation of dynamical processes due to the finer grid spacing, or from the more sophisticated turbulence scheme. Furthermore, the issue concerning the dependence of the results on the model time step makes it hard to refer the findings back to the operational setup.

The results presented in this appendix, however, indicate hints on the important dependence of the SMP coupling on model resolution. Since weather services tend to increase the resolution of their operational models continually, preliminary results presented here encourage further research with an increased number of case studies, as well as experiments with smaller patch sizes. The interpretation of the results would furthermore be facilitated when the same turbulence scheme would be applied to all simulations.

List of Abbreviations

agl	above ground level
BL	Boundary-Layer
$CAPE$	convective available potential energy
CCN	cloud condensation nuclei
CIN	convective inhibition energy
COSMO	Consortium for Small-scale MOdeling
CTP	Convective Triggering Potential
DWD	Deutscher Wetterdienst
ECMWF	European Centre for Medium-Range Weather Forecasts
EPS	Ensemble Prediction System
FSS	Fractions Skill Score
HI_{low}	low-level humidity index
HIW	high impact weather
KENDA	Kilometre-Scale Ensemble Data Assimilation
S_e	Moist Static Energy
SMP coupling	soil moisture-precipitation coupling
LCL	lifting condensation level
LES	large-eddy simulation
LFC	level of free convection
LNB	level of neutral buoyancy
LWP	Liquid Water Path
MFC	Moisture Flux Convergence
MSE	Mean Square Error

NWP	Numerical Weather Prediction
PSP	physically-based stochastic Boundary-Layer perturbations
REF	unperturbed reference simulation
SoE	set of experiment
TERRA-ML	multi-layer soil model
TKE	Turbulent Kinetic Energy
UNI	control simulation with uniform relative soil moisture
UTC	Coordinated Universal Time

List of Figures

List of Tables

Bibliography

Adler, B., N. Kalthoff, and L. Gantner, 2011: Initiation of deep convection caused by land-surface inhomogeneities in West Africa: A modelled case study. *Meteorol. Atmos. Phys.*, **112 (1-2)**, 15–27, doi: 10.1007/s00703-011-0131-2.

Arnault, J., and Coauthors, 2018: Precipitation Sensitivity to the Uncertainty of Terrestrial Water Flow in WRF-Hydro: An Ensemble Analysis for Central Europe. *J. Hydrometeor.*, **19 (6)**, 1007–1025, doi: 10.1175/JHM-D-17-0042.1.

Bachmann, K., C. Keil, and M. Weissmann, 2019: Impact of radar data assimilation and orography on predictability of deep convection. *Q.J.R. Meteorol. Soc.*, **145 (718)**, 117–130, doi: 10.1002/qj.3412.

Baldauf, M., A. Seifert, J. Förstner, D. Majewski, M. Raschendorfer, and T. Reinhardt, 2011: Operational Convective-Scale Numerical Weather Prediction with the COSMO Model: Description and Sensitivities. *Mon. Wea. Rev.*, **139 (12)**, 3887–3905, doi: 10.1175/MWR-D-10-05013.1.

Barrett, A. I., C. Wellmann, A. Seifert, C. Hoose, B. Vogel, and M. Kunz, 2019: One Step at a Time: How Model Time Step Significantly Affects Convection-Permitting Simulations. *J. Adv. Model. Earth Syst.*, **11 (3)**, 641–658, doi: 10.1029/2018MS001418.

Barthlott, C., C. Hauck, G. Schädler, N. Kalthoff, and C. Kottmeier, 2011a: Soil moisture impacts on convective indices and precipitation over complex terrain. *Meteorol. Z.*, **20 (2)**, 185–197, doi: 10.1127/0941-2948/2011/0216.

Barthlott, C., and N. Kalthoff, 2011: A Numerical Sensitivity Study on the Impact of Soil Moisture on Convection-Related Parameters and Convective Precipitation over Complex Terrain. *J. Atmos. Sci.*, **68 (12)**, 2971–2987, doi: 10.1175/JAS-D-11-027.1.

Barthlott, C., and Coauthors, 2011b: Initiation of deep convection at marginal instability in an ensemble of mesoscale models: A case-study from COPS. *Q.J.R. Meteorol. Soc.*, **137 (S1)**, 118–136, doi: 10.1002/qj.707.

Bauer, P., A. Thorpe, and G. Brunet, 2015: The quiet revolution of numerical weather prediction. *Nature*, **525 (7567)**, 47–55, doi: 10.1038/nature14956.

Berner, J., K. R. Fossell, S.-Y. Ha, J. P. Hacker, and C. Snyder, 2015: Increasing the Skill of Probabilistic Forecasts: Understanding Performance Improvements from Model-Error Representations. *Mon. Wea. Rev.*, **143 (4)**, 1295–1320, doi: 10.1175/MWR-D-14-00091.1.

Berner, J., and Coauthors, 2017: Stochastic Parameterization: Toward a New View of Weather and Climate Models. *Bull. Amer. Meteor. Soc.*, **98 (3)**, 565–588, doi: 10.1175/BAMS-D-15-00268.1.

Betts, A. K., and M. A. F. Silva Dias, 2010: Progress in Understanding Land-Surface-Atmosphere Coupling from LBA Research. *J. Adv. Model. Earth Syst.*, **2**, 6, doi: 10.3894/JAMES.2010.2.6.

Bierdel, L., P. Friederichs, and S. Bentzien, 2012: Spatial kinetic energy spectra in the convection-permitting limited-area NWP model COSMO-DE. *Meteorologische Zeitschrift*, 245–258, doi: 10.1127/0941-2948/2012/0319.

Birch, C. E., M. J. Roberts, L. Garcia-Carreras, D. Ackerley, M. J. Reeder, A. P. Lock, and R. Schiemann, 2015: Sea-Breeze Dynamics and Convection Initiation: The Influence of Convective Parameterization in Weather and Climate Model Biases. *J. Climate*, **28 (20)**, 8093–8108, doi: 10.1175/JCLI-D-14-00850.1.

Bouttier, F., L. Raynaud, O. Nuissier, and B. Ménétrier, 2016: Sensitivity of the AROME ensemble to initial and surface perturbations during HyMeX. *Q.J.R. Meteorol. Soc.*, **142**, 390–403, doi: 10.1002/qj.2622.

Bouttier, F., B. Vié, O. Nuissier, and L. Raynaud, 2012: Impact of Stochastic Physics in a Convection-Permitting Ensemble. *Mon. Wea. Rev.*, **140 (11)**, 3706–3721, doi: 10.1175/MWR-D-12-00031.1.

Bright, D. R., and S. L. Mullen, 2002: Short-Range Ensemble Forecasts of Precipitation during the Southwest Monsoon. *Wea. Forecasting*, **17 (5)**, 1080–1100, doi: 10/bb6qh7.

Brune, S., F. Kapp, and P. Friederichs, 2018: A wavelet based analysis of convective organization in ICON large-eddy simulations. *Q.J.R. Meteorol. Soc.*, **144 (717)**, 2812–2829, doi: 10.1002/qj.3409.

Brunsell, N. A., and R. R. Gillies, 2003: Length Scale Analysis of Surface Energy Fluxes Derived from Remote Sensing. *J. Hydrometeor.*, **4 (6)**, 1212–1219, doi: 10.1175/1525-7541(2003)004<1212:LSAOSE>2.0.CO;2.

Bryan, G. H., J. C. Wyngaard, and J. M. Fritsch, 2003: Resolution Requirements for the Simulation of Deep Moist Convection. *Mon. Wea. Rev.*, **131 (10)**, 2394–2416, doi: 10.1175/1520-0493(2003)131<2394:RRFTSO>2.0.CO;2.

Budyko, M. I., 1974: *Climate and life.* No. 18, International geophysics series, Academic Press, New York.

Buizza, R., M. Milleer, and T. N. Palmer, 1999: Stochastic representation of model uncertainties in the ECMWF ensemble prediction system. *Q.J.R. Meteorol. Soc.*, **125 (560)**, 2887–2908, doi: 10/bmtr84.

Buschow, S., J. Pidstrigach, and P. Friederichs, 2019: Assessment of wavelet-based spatial verification by means of a stochastic precipitation model (wv_verif v0.1.0). *Geosci. Model Dev. Discuss.*, 1–26, doi: 10.5194/gmd-2019-90.

Casati, B., 2010: New Developments of the Intensity-Scale Technique within the Spatial Verification Methods Intercomparison Project. *Wea. Forecasting*, **25 (1)**, 113–143, doi: 10.1175/2009WAF2222257.1.

Casati, B., G. Ross, and D. B. Stephenson, 2004: A new intensity-scale approach for the verification of spatial precipitation forecasts. *Met. Apps*, **11 (2)**, 141–154, doi: 10.1017/S1350482704001239.

Chang, J.-T., and P. J. Wetzel, 1990: Effects of Spatial Variations of Soil Moisture and Vegetation on the Evolution of a Prestorm Environment: A Numerical Case Study. *Mon. Wea. Rev.*, **119 (6)**, 1368–1390, doi: 10.1175/1520-0493(1991)119<1368:EOSVOS>2.0.CO;2.

Cheng, W. Y. Y., and W. R. Cotton, 2004: Sensitivity of a Cloud-Resolving Simulation of the Genesis of a Mesoscale Convective System to Horizontal Heterogeneities in Soil Moisture Initialization. *J. Hydrometeor.*, **5 (5)**, 934–958, doi: 10.1175/1525-7541(2004)005<0934:SOACSO>2.0.CO;2.

Cioni, G., and C. Hohenegger, 2017: Effect of soil moisture on diurnal convection and precipitation in Large-Eddy Simulations. *J. Hydrometeor.*, doi: 10.1175/JHM-D-16-0241.1.

Clark, A. J., and Coauthors, 2011: Probabilistic Precipitation Forecast Skill as a Function of Ensemble Size and Spatial Scale in a Convection-Allowing Ensemble. *Mon. Wea. Rev.*, **139 (5)**, 1410–1418, doi: 10.1175/2010MWR3624.1.

Clark, D. B., C. M. Taylor, and A. J. Thorpe, 2004: Feedback between the Land Surface and Rainfall at Convective Length Scales. *J. Hydrometeor.*, **5 (4)**, 625–639, doi: 10.1175/1525-7541(2004)005<0625:FBTLSA>2.0.CO;2.

Clark, P., N. Roberts, H. Lean, S. P. Ballard, and C. Charlton-Perez, 2016: Convection-permitting models: A step-change in rainfall forecasting. *Meteorol. Appl.*, **23 (2)**, 165–181, doi: 10.1002/met.1538.

Craig, G. C., and A. Dörnbrack, 2008: Entrainment in Cumulus Clouds: What Resolution is Cloud-Resolving? *J. Atmos. Sci.*, **65 (12)**, 3978–3988, doi: 10/cpccq6.

Cronin, T. W., K. A. Emanuel, and P. Molnar, 2015: Island precipitation enhancement and the diurnal cycle in radiative-convective equilibrium. *Q.J.R. Meteorol. Soc.*, **141 (689)**, 1017–1034, doi: 10.1002/qj.2443.

Daubechies, I., 1992: *Ten Lectures on Wavelets.* CBMS-NSF Regional Conference Series in Applied Mathematics, Society for Industrial and Applied Mathematics, URL http://epubs.siam.org/doi/book/10.1137/1.9781611970104.

Devara, P. C. S., and M. G. Manoj, 2013: Aerosol–cloud–precipitation interactions: A challenging problem in regional environment and climate research. *Particuology*, **11 (1)**, 25–33, doi: 10.1016/j.partic.2012.07.006.

Dey, S. R. A., G. Leoncini, N. M. Roberts, R. S. Plant, and S. Migliorini, 2014: A Spatial View of Ensemble Spread in Convection Permitting Ensembles. *Mon. Wea. Rev.*, **142 (11)**, 4091–4107, doi: 10.1175/MWR-D-14-00172.1.

Dey, S. R. A., R. S. Plant, N. M. Roberts, and S. Migliorini, 2016: Assessing spatial precipitation uncertainties in a convective-scale ensemble. *Q.J.R. Meteorol. Soc.*, **142 (701)**, 2935–2948, doi: 10.1002/qj.2893.

Dirmeyer, P. A., and Coauthors, 2012: Evidence for Enhanced Land–Atmosphere Feedback in a Warming Climate. *J. Hydrometeor.*, **13 (3)**, 981–995, doi: 10.1175/JHM-D-11-0104.1.

Doms, G., and Coauthors, 2011: A Description of the Nonhydrostatic Regional COSMO Model. *Part II: Physical Parameterization*, URL www.cosmo-model.org/content/model/documentation/core, (accessed 11 Sept 2017).

Done, J. M., G. C. Craig, S. L. Gray, P. A. Clark, and M. E. B. Gray, 2006: Mesoscale simulations of organized convection: Importance of convective equilibrium. *Q.J.R. Meteorol. Soc.*, **132 (616)**, 737–756, doi: 10.1256/qj.04.84.

Draper, C., and R. H. Reichle, 2019: Assimilation of satellite soil moisture for improved atmospheric reanalyses. *Mon. Wea. Rev.*, doi: 10.1175/MWR-D-18-0393.1.

DWD, 2018a: Hoch aufgelöste Niederschlagsanalyse und –vorhersage auf der Basis quantitativer Radar- und Ombrometerdaten für grenzüberschreitende Fluss-Einzugsgebiete von Deutsch land im Echtzeitbetrieb - Beschreibung des Kompositformats Version 2.4.4. URL https://www.dwd.de/DE/leistungen/radolan/radolan_info/radolan_radvor_op_komposit_format_pdf.pdf?__blob=publicationFile&v=6, (accessed 08 Feb 2019).

DWD, 2018b: Radolan Produktübersicht. URL https://www.dwd.de/DE/leistungen/radolan/produktuebersicht/radolan_produktuebersicht_pdf.pdf?__blob=publicationFile&v=6, (accessed 08 Feb 2019).

Ebert, E. E., 2008: Fuzzy verification of high-resolution gridded forecasts: A review and proposed framework. *Meteorol. Appl.*, **15 (1)**, 51–64, doi: 10.1002/met.25.

Eckley, I. A., and G. P. Nason, 2011: LS2W: Implementing the Locally Stationary 2D Wavelet Process Approach in R. *J. Stat. Soft.*, **43 (3)**, doi: 10.18637/jss.v043.i03.

Evensen, G., 1994: Sequential data assimilation with a nonlinear quasi-geostrophic model using Monte Carlo methods to forecast error statistics. *J. Geophys. Res. Oceans*, **99 (C5)**, 10 143–10 162, doi: 10.1029/94JC00572.

Faggian, N., B. Roux, P. Steinle, and B. Ebert, 2015: Fast calculation of the fractions skill score. *Mausam*, **66 (3)**, 457–466.

Fan, J., Y. Wang, D. Rosenfeld, and X. Liu, 2016: Review of Aerosol–Cloud Interactions: Mechanisms, Significance, and Challenges. *J. Atmos. Sci.*, **73 (11)**, 4221–4252, doi: 10.1175/JAS-D-16-0037.1.

Ferguson, C. R., and E. F. Wood, 2011: Observed Land–Atmosphere Coupling from Satellite Remote Sensing and Reanalysis. *J. Hydrometeor.*, **12 (6)**, 1221–1254, doi: 10.1175/2011JHM1380.1.

Findell, K. L., and E. A. B. Eltahir, 2003a: Atmospheric Controls on Soil Moisture–Boundary Layer Interactions. Part I: Framework Development. *J. Hydrometeor.*, **4 (3)**, 552–569, doi: 10.1175/1525-7541(2003)004<0552:ACOSML>2.0.CO;2.

Findell, K. L., and E. A. B. Eltahir, 2003b: Atmospheric Controls on Soil Moisture–Boundary Layer Interactions. Part II: Feedbacks within the Continental United States. *J. Hydrometeor.*, **4 (3)**, 570–583, doi: 10.1175/1525-7541(2003)004<0570:ACOSML>2.0.CO;2.

Ford, T. W., S. M. Quiring, O. W. Frauenfeld, and A. D. Rapp, 2015: Synoptic conditions related to soil moisture-atmosphere interactions and unorganized convection in Oklahoma: Synoptic Patterns Related to Convection. *J. Geophys. Res. Atmos.*, **120 (22)**, 11,519–11,535, doi: 10.1002/2015JD023975.

Ford, T. W., S. M. Quiring, B. Thakur, R. Jogineedi, A. Houston, S. Yuan, A. Kalra, and N. Lock, 2018: Evaluating Soil Moisture–Precipitation Interactions Using Remote Sensing: A Sensitivity Analysis. *J. Hydrometeor.*, **19 (8)**, 1237–1253, doi: 10.1175/JHM-D-17-0243.1.

Frei, T., 2010: Economic and social benefits of meteorology and climatology in Switzerland. *Met. Apps.*, **17 (1)**, 39–44, doi: 10.1002/met.156.

Froidevaux, P., L. Schlemmer, J. Schmidli, W. Langhans, and C. Schär, 2014: Influence of the Background Wind on the Local Soil Moisture–Precipitation Feedback. *J. Atmos. Sci.*, **71 (2)**, 782–799, doi: 10.1175/JAS-D-13-0180.1.

Gallus, W. A., and M. Segal, 2000: Sensitivity of Forecast Rainfall in a Texas Convective System to Soil Moisture and Convective Parameterization. *Wea. Forecasting*, **15 (5)**, 509–525, doi: 10.1175/1520-0434(2000)015<0509:SOFRIA>2.0.CO;2.

Gebhardt, C., S. E. Theis, M. Paulat, and Z. Ben Bouallègue, 2011: Uncertainties in COSMO-DE precipitation forecasts introduced by model perturbations and variation of lateral boundaries. *Atmos. Res.*, **100 (2)**, 168–177, doi: 10.1016/j.atmosres.2010.12.008.

Gilleland, E., D. Ahijevych, B. G. Brown, B. Casati, and E. E. Ebert, 2009: Intercomparison of Spatial Forecast Verification Methods. *Wea. Forecasting*, **24 (5)**, 1416–1430, doi: 10.1175/2009WAF2222269.1.

Grant, L. D., and S. C. van den Heever, 2014: Aerosol-cloud-land surface interactions within tropical sea breeze convection. *J. Geophys. Res. Atmos.*, **119 (13)**, 8340–8361, doi: 10.1002/2014JD021912.

Gu, X., Q. Zhang, J. Li, V. P. Singh, J. Liu, P. Sun, C. He, and J. Wu, 2019: Intensification and Expansion of Soil Moisture Drying in Warm Season Over Eurasia Under Global Warming. *J. Geophys. Res. Atmos.*, **124 (0)**, doi: 10.1029/2018JD029776.

Guillod, B. P., B. Orlowsky, D. G. Miralles, A. J. Teuling, and S. I. Seneviratne, 2015: Reconciling spatial and temporal soil moisture effects on afternoon rainfall. *Nat. Commun.*, **6**, 6443, doi: 10.1038/ncomms7443.

Guillod, B. P., and Coauthors, 2014: Land-surface controls on afternoon precipitation diagnosed from observational data: Uncertainties and confounding factors. *Atmos. Chem. Phys.*, **14 (16)**, 8343–8367, doi: 10.5194/acp-14-8343-2014.

Gunasekera, D., 2010: Use of climate information for socio-economic benefits. *Procedia Environmental Sciences*, **1**, 384–386, doi: 10.1016/j.proenv.2010.09.025.

Guo, Z., P. A. Dirmeyer, T. DelSole, and R. D. Koster, 2012: Rebound in Atmospheric Predictability and the Role of the Land Surface. *J. Climate*, **25 (13)**, 4744–4749, doi: 10.1175/JCLI-D-11-00651.1.

Gustafsson, N., and Coauthors, 2018: Survey of data assimilation methods for convective-scale numerical weather prediction at operational centres. *Q.J.R. Meteorol. Soc.*, **144 (713)**, 1218–1256, doi: 10.1002/qj.3179.

Hally, A., E. Richard, S. Fresnay, and D. Lambert, 2014: Ensemble simulations with perturbed physical parametrizations: Pre-HyMeX case studies. *Q.J.R. Meteorol. Soc.*, **140 (683)**, 1900–1916, doi: 10.1002/qj.2257.

Hauck, C., C. Barthlott, L. Krauss, and N. Kalthoff, 2011: Soil moisture variability and its influence on convective precipitation over complex terrain. *Q.J.R. Meteorol. Soc.*, **137 (S1)**, 42–56, doi: 10.1002/qj.766.

Hillel, D., 1998: *Environmental Soil Physics: Fundamentals, Applications, and Environmental Considerations*. Academic Press, San Diego.

Hohenegger, C., P. Brockhaus, C. S. Bretherton, and C. Schär, 2009: The Soil Moisture–Precipitation Feedback in Simulations with Explicit and Parameterized Convection. *J. Climate*, **22 (19)**, 5003–5020, doi: 10.1175/2009JCLI2604.1.

Hohenegger, C., D. Lüthi, and C. Schär, 2006: Predictability Mysteries in Cloud-Resolving Models. *Mon. Wea. Rev.*, **134 (8)**, 2095–2107, doi: 10.1175/MWR3176.1.

Hohenegger, C., and C. Schär, 2007: Predictability and Error Growth Dynamics in Cloud-Resolving Models. *J. Atmos. Sci.*, **64 (12)**, 4467–4478, doi: 10.1175/2007JAS2143.1.

Hohenegger, C., A. Walser, W. Langhans, and C. Schär, 2008: Cloud-resolving ensemble simulations of the August 2005 Alpine flood. *Q.J.R. Meteorol. Soc.*, **134 (633)**, 889–904, doi: 10.1002/qj.252.

Hoose, C., J. E. Kristjánsson, T. Iversen, A. Kirkevåg, Ø. Seland, and A. Gettelman, 2009: Constraining cloud droplet number concentration in GCMs suppresses the aerosol indirect effect. *Geophys. Res. Lett.*, **36 (12)**, L12 807, doi: 10.1029/2009GL038568.

Hsu, H., M.-H. Lo, B. P. Guillod, D. G. Miralles, and S. Kumar, 2017: Relation between precipitation location and antecedent/subsequent soil moisture spatial patterns. *J. Geophys. Res. Atmos.*, **122 (12)**, 2016JD026 042, doi: 10.1002/2016JD026042.

Igel, A. L., M. R. Igel, and S. C. van den Heever, 2014: Make It a Double? Sobering Results from Simulations Using Single-Moment Microphysics Schemes. *J. Atmos. Sci.*, **72 (2)**, 910–925, doi: 10.1175/JAS-D-14-0107.1.

Ikuta, Y., 2017: Assimilation of Satellite Soil Moisture Contents and Clear-sky Radiance in Operational Local NWP System at JMA. *JpGU-AGU Joint Meeting 2017*, jpGU-AGU Joint Meeting 2017.

Imamovic, A., L. Schlemmer, and C. Schär, 2017: Collective Impacts of Orography and Soil Moisture on the Soil Moisture-Precipitation Feedback. *Geophys. Res. Lett.*, **44 (22)**, 11,682–11,691, doi: 10.1002/2017GL075657.

Jahn, M., 2015: Economics of extreme weather events: Terminology and regional impact models. *Weather and Climate Extremes*, **10**, 29–39, doi: 10.1016/j.wace.2015.08.005.

Jiang, H., and G. Feingold, 2006: Effect of aerosol on warm convective clouds: Aerosol-cloud-surface flux feedbacks in a new coupled large eddy model. *J. Geophys. Res. Atmos.*, **111 (D1)**, doi: 10.1029/2005JD006138.

Johnson, A., and X. Wang, 2016: A Study of Multiscale Initial Condition Perturbation Methods for Convection-Permitting Ensemble Forecasts. *Mon. Wea. Rev.*, **144 (7)**, 2579–2604, doi: 10.1175/MWR-D-16-0056.1.

Kaiser, G., 1994: *A Friendly Guide to Wavelets*. Boston, Massua: Birkhäuser.

Keil, C., and G. C. Craig, 2011: Regime-dependent forecast uncertainty of convective precipitation. *Meteorol. Z.*, **20 (2)**, 145–151, doi: 10.1127/0941-2948/2011/0219.

Keil, C., F. Heinlein, and G. C. Craig, 2014: The convective adjustment time-scale as indicator of predictability of convective precipitation. *Q.J.R. Meteorol. Soc.*, **140 (679)**, 480–490, doi: 10.1002/qj.2143.

Kirshbaum, D. J., B. Adler, N. Kalthoff, C. Barthlott, and S. Serafin, 2018: Moist Orographic Convection: Physical Mechanisms and Links to Surface-Exchange Processes. *Atmosphere*, **9 (3)**, 80, doi: 10.3390/atmos9030080.

Klasa, C., M. Arpagaus, A. Walser, and H. Wernli, 2018: An evaluation of the convection-permitting ensemble COSMO-E for three contrasting precipitation events in Switzerland. *Q.J.R. Meteorol. Soc.*, **144 (712)**, 744–764, doi: 10.1002/qj.3245.

Kober, K., and G. C. Craig, 2016: Physically Based Stochastic Perturbations (PSP) in the Boundary Layer to Represent Uncertainty in Convective Initiation. *J. Atmos. Sci.*, **73 (7)**, 2893–2911, doi: 10.1175/JAS-D-15-0144.1.

Koster, R. D., S. D. Schubert, and M. J. Suarez, 2009: Analyzing the Concurrence of Meteorological Droughts and Warm Periods, with Implications for the Determination of Evaporative Regime. *J. Climate*, **22 (12)**, 3331–3341, doi: 10.1175/2008JCLI2718.1.

Koster, R. D., and Coauthors, 2004: Regions of Strong Coupling Between Soil Moisture and Precipitation. *Science*, **305 (5687)**, 1138–1140, doi: 10.1126/science.1100217.

Kottmeier, C., and Coauthors, 2008: Mechanisms initiating deep convection over complex terrain during COPS. *Meteorol. Z.*, **17 (6)**, 931–948, doi: 10.1127/0941-2948/2008/0348.

Koukoula, M., E. I. Nikolopoulos, J. Kushta, N. S. Bartsotas, G. Kallos, and E. N. Anagnostou, 2019: A Numerical Sensitivity Analysis of Soil Moisture Feedback on Convective Precipitation. *J. Hydrometeor.*, **20 (1)**, 23–44, doi: 10.1175/JHM-D-18-0134.1.

Kühnlein, C., C. Keil, G. C. Craig, and C. Gebhardt, 2014: The impact of downscaled initial condition perturbations on convective-scale ensemble forecasts of precipitation. *Q.J.R. Meteorol. Soc.*, **140 (682)**, 1552–1562, doi: 10.1002/qj.2238.

Kunz, M., J. Sander, and C. Kottmeier, 2009: Recent trends of thunderstorm and hailstorm frequency and their relation to atmospheric characteristics in southwest Germany. *Int. J. Climatol.*, **29 (15)**, 2283–2297, doi: 10.1002/joc.1865.

Lee, J. M., Y. Zhang, and S. A. Klein, 2019: The Effect of Land Surface Heterogeneity and Background Wind on Shallow Cumulus Clouds and the Transition to Deeper Convection. *J. Atmos. Sci.*, **76 (2)**, 401–419, doi: 10.1175/JAS-D-18-0196.1.

Leutbecher, M., and Coauthors, 2017: Stochastic representations of model uncertainties at ECMWF: State of the art and future vision. *Q.J.R. Meteorol. Soc.*, **143 (707)**, 2315–2339, doi: 10/gckb59.

Lin, J. W.-B., and J. D. Neelin, 2003: Toward stochastic deep convective parameterization in general circulation models. *Geophys. Res. Lett.*, **30 (4)**, doi: 10/dzdfrq.

Lin, L.-F., A. M. Ebtehaj, A. N. Flores, S. Bastola, and R. L. Bras, 2017: Combined Assimilation of Satellite Precipitation and Soil Moisture: A Case Study Using TRMM and SMOS Data. *Mon. Wea. Rev.*, **145 (12)**, 4997–5014, doi: 10.1175/MWR-D-17-0125.1.

Lorenz, E. N., 1963: Deterministic Nonperiodic Flow. *J. Atmos. Sci.*, **20 (2)**, 130–141, doi: 10.1175/1520-0469(1963)020<0130:DNF>2.0.CO;2.

Lorenz, E. N., 1982: Atmospheric predictability experiments with a large numerical model. *Tellus*, **34 (6)**, 505–513, doi: 10.3402/tellusa.v34i6.10836.

Mahfouf, J.-F., E. Richard, and P. Mascart, 1987: The Influence of Soil and Vegetation on the Development of Mesoscale Circulations. *J. Climate Appl. Meteor.*, **26 (11)**, 1483–1495, doi: 10.1175/1520-0450(1987)026<1483:TIOSAV>2.0.CO;2.

Markowski, P., and Y. Richardson, 2010: *Mesoscale Meteorology in Midlatitudes*. John Wiley & Sons.

May, R., S. Arms, P. Marsh, E. Bruning, and J. Leeman, 2008: MetPy: A Python Package for Meteorological Data. Boulder, Colorado, URL https://github.com/Unidata/MetPy, UCAR/NCAR - Unidata, doi: 10.5065/D6WW7G29.

Mellor, G. L., and T. Yamada, 1982: Development of a turbulence closure model for geophysical fluid problems. *Rev. Geophys.*, **20 (4)**, 851–875, doi: 10.1029/RG020i004p00851.

Mills, E., 2005: Insurance in a Climate of Change. *Science*, **309 (5737)**, 1040–1044, doi: 10.1126/science.1112121.

Mittermaier, M., and N. Roberts, 2010: Intercomparison of Spatial Forecast Verification Methods: Identifying Skillful Spatial Scales Using the Fractions Skill Score. *Wea. Forecasting*, **25 (1)**, 343–354, doi: 10.1175/2009WAF2222260.1.

Mittermaier, M., N. Roberts, and S. A. Thompson, 2013: A long-term assessment of precipitation forecast skill using the Fractions Skill Score. *Met. Apps*, **20 (2)**, 176–186, doi: 10.1002/met.296.

Mittermaier, M. P., 2006: Using an intensity-scale technique to assess the added benefit of high-resolution model precipitation forecasts. *Atmospheric Science Letters*, **7 (2)**, 36–42, doi: 10.1002/asl.127.

Molini, L., A. Parodi, N. Rebora, and G. C. Craig, 2011: Classifying severe rainfall events over Italy by hydrometeorological and dynamical criteria. *Quarterly Journal of the Royal Meteorological Society*, **137 (654)**, 148–154, doi: 10.1002/qj.741.

Moon, H., B. P. Guillod, L. Gudmundsson, and S. I. Seneviratne, 2019: Soil Moisture Effects on Afternoon Precipitation Occurrence in Current Climate Models. *Geophys. Res. Lett.*, **46 (3)**, 1861–1869, doi: 10.1029/2018GL080879.

Pal, J. S., and E. A. B. Eltahir, 2001: Pathways Relating Soil Moisture Conditions to Future Summer Rainfall within a Model of the Land–Atmosphere System. *J. Climate*, **14 (6)**, 1227–1242, doi: 10.1175/1520-0442(2001)014<1227:PRSMCT>2.0.CO;2.

Peralta, C., Z. B. Bouallègue, S. E. Theis, C. Gebhardt, and M. Buchhold, 2012: Accounting for initial condition uncertainties in COSMO-DE-EPS. *Journal of Geophysical Research: Atmospheres*, **117 (D7)**, doi: 10.1029/2011JD016581.

Pielke, R. A., 2001: Influence of the spatial distribution of vegetation and soils on the prediction of cumulus Convective rainfall. *Rev. Geophys.*, **39 (2)**, 151–177, doi: 10.1029/1999RG000072.

Piper, D., M. Kunz, F. Ehmele, S. Mohr, B. Mühr, A. Kron, and J. Daniell, 2016: Exceptional sequence of severe thunderstorms and related flash floods in May and June 2016 in Germany – Part 1: Meteorological background. *Nat. Hazards Earth Syst. Sci.*, **16 (12)**, 2835–2850, doi: 10.5194/nhess-16-2835-2016.

Rasp, S., T. Selz, and G. C. Craig, 2018: Variability and Clustering of Midlatitude Summertime Convection: Testing the Craig and Cohen Theory in a Convection-Permitting Ensemble with Stochastic Boundary Layer Perturbations. *J. Atmos. Sci.*, **75 (2)**, 691–706, doi: 10.1175/JAS-D-17-0258.1.

Raynaud, L., and F. Bouttier, 2016: Comparison of initial perturbation methods for ensemble prediction at convective scale. *Q.J.R. Meteorol. Soc.*, **142 (695)**, 854–866, doi: 10.1002/qj.2686.

Rieck, M., C. Hohenegger, and C. C. van Heerwaarden, 2014: The Influence of Land Surface Heterogeneities on Cloud Size Development. *Mon. Wea. Rev.*, **142 (10)**, 3830–3846, doi: 10.1175/MWR-D-13-00354.1.

Ritter, B., and J.-F. Geleyn, 1992: A Comprehensive Radiation Scheme for Numerical Weather Prediction Models with Potential Applications in Climate Simulations. *Mon. Wea. Rev.*, **120 (2)**, 303–325, doi: 10.1175/1520-0493(1992)120<0303:ACRSFN>2.0.CO;2.

Roberts, N. M., and H. W. Lean, 2008: Scale-Selective Verification of Rainfall Accumulations from High-Resolution Forecasts of Convective Events. *Mon. Wea. Rev.*, **136 (1)**, 78–97, doi: 10.1175/2007MWR2123.1.

Robinson, F. J., S. C. Sherwood, and Y. Li, 2008: Resonant Response of Deep Convection to Surface Hot Spots. *J. Atmos. Sci.*, **65 (1)**, 276–286, doi: 10.1175/2007JAS2398.1.

Rochetin, N., F. Couvreux, and F. Guichard, 2016: Morphology of breeze circulations induced by surface flux heterogeneities and their impact on convection initiation. *Q.J.R. Meteorol. Soc.*, n/a–n/a, doi: 10.1002/qj.2935.

Romine, G. S., C. S. Schwartz, J. Berner, K. R. Fossell, C. Snyder, J. L. Anderson, and M. L. Weisman, 2014: Representing Forecast Error in a Convection-Permitting Ensemble System. *Mon. Wea. Rev.*, **142 (12)**, 4519–4541, doi: 10.1175/MWR-D-14-00100.1.

Roundy, J. K., C. R. Ferguson, and E. F. Wood, 2012: Temporal Variability of Land–Atmosphere Coupling and Its Implications for Drought over the Southeast United States. *J. Hydrometeor.*, **14 (2)**, 622–635, doi: 10.1175/JHM-D-12-090.1.

Santanello, J. A., P. Lawston, S. Kumar, and E. Dennis, 2019: Understanding the Impacts of Soil Moisture Initial Conditions on NWP in the Context of Land–Atmosphere Coupling. *J. Hydrometeor.*, **20 (5)**, 793–819, doi: 10.1175/JHM-D-18-0186.1.

Schär, C., D. Lüthi, U. Beyerle, and E. Heise, 1999: The Soil–Precipitation Feedback: A Process Study with a Regional Climate Model. *J. Climate*, **12 (3)**, 722–741, doi: 10.1175/1520-0442(1999)012<0722:TSPFAP>2.0.CO;2.

Schättler, U., and U. Blahak, 2017: Part V: Preprocessing: Initial and Boundary Data for the COSMO-Model. *A Description of the Nonhydrostatic Regional COSMO Model*, URL www.cosmo-model.org/content/model/documentation/core, (accessed 11 Sept 2017).

Scheck, L., P. Frèrebeau, R. Buras-Schnell, and B. Mayer, 2016: A fast radiative transfer method for the simulation of visible satellite imagery. *Journal of Quantitative Spectroscopy and Radiative Transfer*, **175**, 54–67, doi: 10.1016/j.jqsrt.2016.02.008.

Schlemmer, L., C. Hohenegger, J. Schmidli, and C. Schär, 2012: Diurnal equilibrium convection and land surface–atmosphere interactions in an idealized cloud-resolving model. *Q.J.R. Meteorol. Soc.*, **138 (667)**, 1526–1539, doi: 10.1002/qj.1892.

Schneider, L., C. Barthlott, A. I. Barrett, and C. Hoose, 2018: The precipitation response to variable terrain forcing over low mountain ranges in different weather regimes. *Q.J.R. Meteorol. Soc.*, **144 (713)**, 970–989, doi: 10.1002/qj.3250.

Schraff, C., H. Reich, A. Rhodin, A. Schomburg, K. Stephan, A. Periáñez, and R. Potthast, 2016: Kilometre-scale ensemble data assimilation for the COSMO model (KENDA). *Q.J.R. Meteorol. Soc.*, **142 (696)**, 1453–1472, doi: 10.1002/qj.2748.

Segal, M., and R. W. Arritt, 1992: Nonclassical Mesoscale Circulations Caused by Surface Sensible Heat-Flux Gradients. *Bull. Amer. Meteor. Soc.*, **73 (10)**, 1593–1604, doi: 10.1175/1520-0477(1992)073<1593:NMCCBS>2.0.CO;2.

Segal, Y., and A. Khain, 2006: Dependence of droplet concentration on aerosol conditions in different cloud types: Application to droplet concentration parameterization of aerosol conditions. *J. Geophys. Res. Atmos.*, **111 (D15)**, D15 204, doi: 10.1029/2005JD006561.

Seifert, A., and K. D. Beheng, 2006: A two-moment cloud microphysics parameterization for mixed-phase clouds. Part 1: Model description. *Meteorol. Atmos. Phys.*, **92 (1-2)**, 45–66, doi: 10.1007/s00703-005-0112-4.

Seifert, A., C. Köhler, and K. D. Beheng, 2012: Aerosol-cloud-precipitation effects over Germany as simulated by a convective-scale numerical weather prediction model. *Atmos. Chem. Phys.*, **12 (2)**, 709–725, doi: https://doi.org/10.5194/acp-12-709-2012.

Selz, T., and G. C. Craig, 2015: Upscale Error Growth in a High-Resolution Simulation of a Summertime Weather Event over Europe. *Mon. Wea. Rev.*, **143 (3)**, 813–827, doi: 10.1175/MWR-D-14-00140.1.

Seneviratne, S. I., T. Corti, E. L. Davin, M. Hirschi, E. B. Jaeger, I. Lehner, B. Orlowsky, and A. J. Teuling, 2010: Investigating soil moisture–climate interactions in a changing climate: A review. *Earth-Science Reviews*, **99 (3)**, 125–161, doi: 10.1016/j.earscirev.2010.02.004.

Sharif, I., and S. Khare, 2014: Comparative Analysis of Haar and Daubechies Wavelet for Hyper Spectral Image Classification. *Int. Arch. Photogramm. Remote Sens. Spatial Inf. Sci.*, **XL-8**, 937–941, doi: 10.5194/isprsarchives-XL-8-937-2014.

Skok, G., and N. Roberts, 2016: Analysis of Fractions Skill Score properties for random precipitation fields and ECMWF forecasts. *Q.J.R. Meteorol. Soc.*, **142 (700)**, 2599–2610, doi: 10.1002/qj.2849.

Slingo, J., and T. Palmer, 2011: Uncertainty in weather and climate prediction. *Philosophical Transactions of the Royal Society A: Mathematical, Physical and Engineering Sciences*, **369 (1956)**, 4751–4767, doi: 10.1098/rsta.2011.0161.

Stensrud, D. J., J.-W. Bao, and T. T. Warner, 2000: Using Initial Condition and Model Physics Perturbations in Short-Range Ensemble Simulations of Mesoscale Convective Systems. *Mon. Wea. Rev.*, **128 (7)**, 2077–2107, doi: 10.1175/1520-0493(2000)128<2077:UICAMP>2.0.CO;2.

Surcel, M., I. Zawadzki, M. K. Yau, M. Xue, and F. Kong, 2017: More on the Scale Dependence of the Predictability of Precipitation Patterns: Extension to the 2009–13 CAPS Spring Experiment Ensemble Forecasts. *Mon. Wea. Rev.*, **145 (9)**, 3625–3646, doi: 10.1175/MWR-D-16-0362.1.

Tao, W.-K., J.-P. Chen, Z. Li, C. Wang, and C. Zhang, 2012: Impact of aerosols on convective clouds and precipitation. *Rev. Geophys.*, **50 (2)**, doi: 10.1029/2011RG000369.

Taylor, C. M., 2015: Detecting soil moisture impacts on convective initiation in Europe. *Geophys. Res. Lett.*, **42 (11)**, 2015GL064 030, doi: 10.1002/2015GL064030.

Taylor, C. M., C. E. Birch, D. J. Parker, N. Dixon, F. Guichard, G. Nikulin, and G. M. S. Lister, 2013: Modeling soil moisture-precipitation feedback in the Sahel: Importance of spatial scale versus convective parameterization. *Geophys. Res. Lett.*, **40 (23)**, 2013GL058 511, doi: 10.1002/2013GL058511.

Taylor, C. M., R. A. M. de Jeu, F. Guichard, P. P. Harris, and W. A. Dorigo, 2012: Afternoon rain more likely over drier soils. *Nature*, **489 (7416)**, 423–426, doi: 10.1038/nature11377.

Taylor, C. M., and R. J. Ellis, 2006: Satellite detection of soil moisture impacts on convection at the mesoscale. *Geophys. Res. Lett.*, **33 (3)**, L03 404, doi: 10.1029/2005GL025252.

Taylor, C. M., A. Gounou, F. Guichard, P. P. Harris, R. J. Ellis, F. Couvreux, and M. De Kauwe, 2011: Frequency of Sahelian storm initiation enhanced over mesoscale soil-moisture patterns. *Nat. Geosci.*, **4 (7)**, 430–433, doi: 10.1038/ngeo1173.

Taylor, C. M., C. Prigent, and S. J. Dadson, 2018: Mesoscale rainfall patterns observed around wetlands in sub-Saharan Africa. *Q.J.R. Meteorol. Soc.*, **144 (716)**, 2118–2132, doi: 10/gfktr9.

Theis, S., C. Gebhardt, and Z. B. Bouallegue, 2015: Beschreibung des COSMO-DE-EPS und seiner Ausgabe in die Datenbanken des DWD (Version 2.0). Tech. rep., 76 pp. URL https://www.dwd.de/SharedDocs/downloads/DE/modelldokumentationen/nwv/cosmo_de_eps/cosmo_de_eps_dbbeschr_20150922.html?nn=16102.

Theis, S., C. Gebhardt, and Z. B. Bouallegue, 2017: Beschreibung des COSMO-DE-EPS und seiner Ausgabe in die Datenbanken des DWD (Version 3.0). Tech. rep., 81 pp. URL https://www.dwd.de/SharedDocs/downloads/DE/modelldokumentationen/nwv/cosmo_de_eps/cosmo_de_eps_dbbeschr_20170321.html?nn=16102.

Tiedtke, M., 1989: A Comprehensive Mass Flux Scheme for Cumulus Parameterization in Large-Scale Models. *Mon. Wea. Rev.*, **117 (8)**, 1779–1800, doi: 10.1175/1520-0493(1989)117<1779:ACMFSF>2.0.CO;2.

Trier, S. B., F. Chen, and K. W. Manning, 2004: A Study of Convection Initiation in a Mesoscale Model Using High-Resolution Land Surface Initial Conditions. *Mon. Wea. Rev.*, **132 (12)**, 2954–2976, doi: 10.1175/MWR2839.1.

Trier, S. B., F. Chen, K. W. Manning, M. A. LeMone, and C. A. Davis, 2008: Sensitivity of the PBL and Precipitation in 12-Day Simulations of Warm-Season Convection Using Different Land Surface Models and Soil Wetness Conditions. *Mon. Wea. Rev.*, **136 (7)**, 2321–2343, doi: 10.1175/2007MWR2289.1.

Van Weverberg, K., N. P. M. van Lipzig, L. Delobbe, and D. Lauwaet, 2010: Sensitivity of quantitative precipitation forecast to soil moisture initialization and microphysics parametrization. *Q.J.R. Meteorol. Soc.*, **136 (649)**, 978–996, doi: 10.1002/qj.611.

Vié, B., O. Nuissier, and V. Ducrocq, 2011: Cloud-Resolving Ensemble Simulations of Mediterranean Heavy Precipitating Events: Uncertainty on Initial Conditions and Lateral Boundary Conditions. *Mon. Wea. Rev.*, **139 (2)**, 403–423, doi: 10.1175/2010MWR3487.1.

Wallace, J., and P. Hobbs, 2006: *Atmospheric Science*. 2nd ed., Elsevier Academic Press, Amsterdam.

Weckwerth, T. M., and D. B. Parsons, 2006: A Review of Convection Initiation and Motivation for IHOP_2002. *Mon. Wea. Rev.*, **134 (1)**, 5–22, doi: 10.1175/MWR3067.1.

Welty, J., and X. Zeng, 2018: Does Soil Moisture Affect Warm Season Precipitation Over the Southern Great Plains? *Geophys. Res. Lett.*, **45 (15)**, 7866–7873, doi: 10.1029/2018GL078598.

Wilks, D. S., 2011: *Statistical Methods in the Atmospheric Sciences*. 3rd ed., Elsevier Academic Press, Amsterdam, URL http://www.myilibrary.com?id=310129, oCLC: 733937718.

Yang, K., C. Wang, and H. Bao, 2016: Contribution of soil moisture variability to summer precipitation in the Northern Hemisphere: SOIL MOISTURE AND SUMMER PRECIPITATION. *J. Geophys. Res. Atmos.*, **121 (20)**, 12,108–12,124, doi: 10.1002/2016JD025644.

Yano, J.-I., and Coauthors, 2018: Scientific Challenges of Convective-Scale Numerical Weather Prediction. *Bull. Amer. Meteor. Soc.*, **99 (4)**, 699–710, doi: 10.1175/BAMS-D-17-0125.1.

Yoden, S., 2007: Atmospheric Predictability. *J. Meteor. Soc. Japan*, **85B**, 77–102, doi: 10.2151/jmsj.85B.77.

Zeng, Y., T. Janjić, A. de Lozar, U. Blahak, H. Reich, C. Keil, and A. Seifert, 2018: Representation of Model Error in Convective-Scale Data Assimilation: Additive Noise, Relaxation Methods, and Combinations. *J. Adv. Model. Earth Syst.*, **10 (11)**, 2889–2911, doi: 10.1029/2018MS001375.

Zhang, F., Y. Q. Sun, L. Magnusson, R. Buizza, S.-J. Lin, J.-H. Chen, and K. Emanuel, 2019: What Is the Predictability Limit of Midlatitude Weather? *J. Atmos. Sci.*, **76 (4)**, 1077–1091, doi: 10.1175/JAS-D-18-0269.1.

Zhang, X., 2019: Multiscale Characteristics of Different-Source Perturbations and Their Interactions for Convection-Permitting Ensemble Forecasting during SCMREX. *Mon. Wea. Rev.*, **147 (1)**, 291–310, doi: 10.1175/MWR-D-18-0218.1.

Zhang, Y., S. A. Klein, J. Fan, A. S. Chandra, P. Kollias, S. Xie, and S. Tang, 2017: Large-Eddy Simulation of Shallow Cumulus over Land: A Composite Case Based on ARM Long-Term Observations at Its Southern Great Plains Site. *J. Atmos. Sci.*, **74 (10)**, 3229–3251, doi: 10.1175/JAS-D-16-0317.1.

Acknowledgements

Most of all, I want to thank my supervisors George Craig and Christian Keil for giving helpful advice in all aspects of this project. Christian, George, With the precious time you invested in me, you gave me scientific and personal guidance through this very exciting period of my life. Furthermore, I want to thank Bernhard Mayer for co-examining this thesis.

I am thankful that I was a part of the awesome and inspiring Waves to Weather community. The community enabled me to make great experiences at many meetings, conferences, and ECS activities, and, especially, at the NAWDEX research campaign in Iceland. Special thanks to my B3 colleagues Linda Schneider and Christian Barthlott from Karlsruhe for the pleasant and excellent collaboration.

I am honored by Christoph Schär, Linda Schlemmer, and Adel Imamovic for the invitation to the ETH in Zürich. Thanks to all of you!

Special thanks to Robert Redl, you always took time for my computer problems. I am sure that the institute would just crash entirely without you. Besides that, the morning coffee was always a great start in the day.
Thank you, Leonhard Scheck, for always having an open ear and excellent solution for my scientific questions and for helping me with your great MFASIS operator. Furthermore, you provided an island for cheap jokes and strange Bavarian accents.

Special thanks to the best office mates. We had plenty of fun with joyful, but sometimes crazy, weird, or pointless discussions and occasionally an excellent espresso. The office atmosphere was a perfect mixture of fun and professionalism. Our decoration is fantastic, is it? Thank you, Yvonne Ruckstuhl, for uncountable things. You patiently corrected my English and made me learn about many aspects of life and science by nicely asking numerous questions. I am grateful to Federico Grazzini for sharing your great scientific and personal experience. Your great passion for meteorology, climatology, and mountains was always very inspiring for me! Philip Rupp, thank you for installing living plants in the office. Let me know if you ever print one of your plots on a shirt. Thanks, Stephan Rasp, for regularly showing me how efficient and at the same time joyful work can be.

I wish to thank Kevin Bachmann for all the more and less scientific, but always very fruitful and joyful discussions in uncountable coffee-breaks throughout the last years. I am more than happy that we met again as friends and colleagues here in Munich to share this exciting time.

I met so many great colleagues, mentioned in here or not, making time in Munich great and make everyday's way to work easy. Matthias Schindler, Mirjam Hirt, Tobias Selz, Tobias Necker, Philipp Gregor, Joel Arnault, Audine Laurian, Andrea Schäfer, you made every day special!

Thank you Mathias Rotach for continuously mentoring and pushing me during my Master studies. You finally encouraged me to apply for Doctoral studies.

To my friends and family, you helped me with great support during this time. The awesome Burschen at home, the wonderful Kapritzen from Innsbruck, my great friends in the Vorstandschaft, Damenmannschaft, and Herrenmannschaft from the sports club, you all participated in this academic adventure by continuously supporting me.

I feel sincere gratitude towards my family and to my amazing partner Melly. You definitely had to bear most of my bad mood if something does not work as it was supposed to. Thanks for always supporting me and giving me a warm home. Melly, I'm looking forward to many adventures with you and Dumbo. Thank you, Michael, for still being with me even if you can't be here anymore.

Thank you all und liabe Grüaßlen!